AGH University of Science and Technology
in Cracow

Faculty of Physics and Applied Computer Science

Jarosław Łukasik

Measurement of the proton diffractive structure function in deep inelastic e^+p scattering with the ZEUS detector at HERA

PhD Thesis

Supervisor: Dr hab. M. Przybycień

November 2007

To my parents

Abstract

A detailed analysis of the diffractive process $\gamma^* p \to Xp$ in deep inelastic e^+p scattering is presented. The data taken with the ZEUS detector were extracted with the requirement of a large rapidity gap (LRG) between hadronic final state X and the outgoing proton. The measurement was done for photon virtualities $2 < Q^2 < 305\,\mathrm{GeV}^2$, masses of the hadronic final state $2 < M_X < 25\,\mathrm{GeV}$ and the $\gamma^* p$ centre of mass energies $40 < W < 240\,\mathrm{GeV}$. Events were selected with $0.0002 < x_{\mathrm{IP}} < 0.02$, where x_{IP} indicates fractional momentum loss of the scattered proton. The data support a factorisable x_{IP} dependence, which can be described by the exchange of an effective Pomeron trajectory with intercept $\alpha_{\mathrm{IP}}(0) = 1.118 \pm 0.007(\mathrm{exp.})^{+0.019}_{-0.010}(\mathrm{model})$. The x_{IP} and β dependences of the reduced diffractive cross section $\sigma_r^{D(3)}$ are discussed. The ratio of the $\sigma_r^{D(3)}$ obtained from the analysis of events with a measured leading proton (LPS) and from LRG analysis is presented. The Q^2 dependence of the $\alpha_{\mathrm{IP}}(0)$ was also measured.

Contents

1 Introduction **1**

2 Theoretical background **4**
2.1 Deep Inelastic *ep* Scattering . . . 4
2.1.1 Kinematics in DIS . . . 4
2.1.2 Cross sections and structure functions . . . 6
2.1.3 Quark parton model . . . 8
2.1.4 Quantum Chromodynamics . . . 9
2.1.5 Evolution equations . . . 11
2.2 Diffraction . . . 13
2.2.1 Properties of diffractive processes . . . 14
2.2.2 Regge formalism . . . 16
2.2.3 Diffractive photoproduction . . . 22
2.2.4 Diffraction in DIS . . . 23
2.2.5 Diffractive Parton Distribution Functions . . . 26
2.2.6 Models of diffraction in DIS . . . 26

3 The experimental setup **30**
3.1 The HERA accelerator . . . 30
3.2 The ZEUS detector . . . 32
3.2.1 The Central Tracking Detector . . . 36
3.2.2 The Uranium Calorimeter . . . 37
3.2.3 The Forward Plug Calorimeter . . . 39
3.2.4 The luminosity measurement . . . 40
3.2.5 The trigger and data acquisition system . . . 42

4 Event simulation **44**
4.1 Diffractive events simulation—SATRAP MC . . . 45
4.2 Inclusive DIS events simulation—DJANGOH MC . . . 45
4.3 Photoproduction events simulation—PYTHIA MC . . . 46
4.4 Simulation of the detector and offline reconstruction . . . 47

4.5 Monte Carlo event samples . . . 47

5 Event reconstruction **50**
5.1 Vertex reconstruction . . . 50
5.2 Reconstruction of scattered electron . . . 51
5.3 Hadronic system reconstruction . . . 54
5.3.1 Clustering of calorimeter cells and tracks matching . . . 55
5.3.2 Hadronic final state variables . . . 59
5.4 Reconstruction of the kinematic variables . . . 59
5.4.1 The electron method . . . 63
5.4.2 The Jacquet-Blondel method . . . 63
5.4.3 The double angle method . . . 64
5.4.4 Weighted reconstruction method . . . 64
5.5 Comparison of data with MC simulation . . . 65

6 Event selection and background estimation **73**
6.1 Methods of the diffractive contribution selection . . . 73
6.1.1 Use of the Leading Proton Spectrometer . . . 73
6.1.2 Selection of events with a large rapidity gap . . . 74
6.1.3 The M_X method . . . 75
6.2 Trigger selection . . . 77
6.3 Offline selection cuts . . . 79
6.3.1 DIS selection cuts . . . 79
6.3.2 RCAL electron position cuts . . . 80
6.3.3 Kinematic phase space cuts . . . 81
6.3.4 Diffractive events selection . . . 82
6.4 Background discussion . . . 82

7 Results **87**
7.1 Kinematic range and binning . . . 87
7.2 Acceptance corrections . . . 88
7.3 Systematic uncertainties . . . 89
7.4 Diffractive reduced cross section $x_{\mathrm{IP}}\sigma_r^{D(3)}$ . . . 92
7.5 Pomeron trajectory . . . 93

8 Conclusions **102**

A Tables of the reduced diffractive cross section **103**

Acknowledgements **117**

List of Figures

2.1 Schematic diagram of deep inelastic lepton-proton scattering. 5
2.2 The structure function F_2 as a function of Q^2 for different values of x. The results from ZEUS, H1, and fixed-target experiments are shown. 10
2.3 Schematic diagram of scaling violation. 11
2.4 Elementary vertices in QCD and associated splitting functions. 12
2.5 Range of validity for various evolution equations. 12
2.6 The notation for a ladder diagram with emission of n gluons. 13
2.7 (a) Elastic hadron-hadron scattering, (b) Single dissociation, (c) Double dissociation. 14
2.8 The differential pp elastic scattering cross section $d\sigma/dt$ for different values of the centre of mass energy squared s. 15
2.9 The differential cross section for the inelastic diffractive process $pp \to Xp$ as a function of scaled diffractive mass M_X^2/s. 17
2.10 Spin J versus mass squared for different mesons. 18
2.11 The total cross sections for hadronic, γp, and $\gamma\gamma$ scattering as a function of $\sqrt{s}$. 19
2.12 Regge diagrams for the total, elastic, and single diffractive hadron-hadron scatterings. 21
2.13 Diagrams illustrating the classification of diffractive processes in γp scattering. 23
2.14 Event topologies and particle flow diagrams for non-diffractive deep inelastic scattering event and for diffractive DIS event. 24
2.15 Diagram of a diffractive DIS event where the virtual photon dissociates. . . 25

3.1 The HERA accelerator complex and four experiments: ZEUS , H1, HERMES, and HERA-B. 31
3.2 The integrated luminosity delivered by HERA and collected by the ZEUS detector during the 1993-2000 running periods. 32
3.3 The longitudinal cut of the ZEUS detector. 34
3.4 The cross section of the ZEUS detector. 35
3.5 Layout of the CTD octant. 36

3.6 A schematic picture of the FCAL module. 38
3.7 The view of the CAL geometry. 39
3.8 Front view of the FPC. 40
3.9 The LUMI system—location of the LUMI-e and LUMI-γ components. . . . 41
3.10 Diagram of the ZEUS three level trigger and data acquisition system. . . . 43

4.1 Schematic diagram of an inclusive DIS Monte Carlo generator. 45
4.2 Feynman diagrams of the Born level and the LO QED corrections to NC DIS scattering implemented in HERACLES. 46
4.3 Data flow diagram for the real data and Monte Carlo simulation chain in the ZEUS experiment. 48

5.1 The distribution of the z component of the vertex after the diffractive selection for data and MC. 51
5.2 The distributions of the x (left) and y (right) components of the scattered positron after the diffractive selection for data and MC. 53
5.3 The distributions of the scattered electron energy and polar angle after the diffractive selection for data and MC. 53
5.4 The principle of combining neighbouring calorimeter cells into cell islands. 56
5.5 Combining EMC and HAC cell islands into cone islands. 57
5.6 The four-momentum of the hadronic final state system: distributions of the energy, p_x, p_y and p_z after the diffractive selection for data and MC. . . 60
5.7 The reconstructed mass of the diffractive system after the diffractive selection for data and MC. 61
5.8 Relative difference between the generated and measured diffractive masses. 61
5.9 Isolines of the constant energy and polar angle drawn for the scattered electron and current jet in the (Q^2, W) plane. 62
5.10 Relative difference between the generated and measured values of Q^2 for the electron, double angle, and weighted reconstruction methods as a function of generated and reconstructed Q^2 values. 66
5.11 Relative difference between the generated and measured values of W for electron, double angle, and weighted reconstruction methods as a function of generated and reconstructed W values. 67
5.12 Relative difference between the generated and measured values of Q^2 and W for weighted reconstruction method. 68
5.13 Relative difference between the generated and measured values of x_{IP} and β. 68
5.14 Relative differences between the generated and measured value of Q^2, W, M_X, x_{IP}, and β as a function of generated value of respective variable. . . . 69
5.15 Relative differences between the generated and measured value of Q^2, W, M_X, x_{IP}, and β as a function of reconstructed value of respective variable. 70

5.16 Distributions of the reconstructed Q^2 shown as a $\log Q^2$, W, x_{IP} shown as a $\log x_{\mathrm{IP}}$, and β after the diffractive selection for data and MC. 71
5.17 Distributions of the reconstructed $E-p_z$, η_{max}, and γ_h after the diffractive selection for data and MC. 72

6.1 The x_L spectrum measured by LPS. 74
6.2 Event display diagram for the diffractive DIS event with a maximum rapidity of $\eta_{max} = 0.6$. 75
6.3 Distribution of the η_{max} for the DIS data made for $134 < W < 164\,\mathrm{GeV}$ and $20 < Q^2 < 40\,\mathrm{GeV}^2$. 76
6.4 The distribution of $\ln M_X^2$ in several Q^2 and W bins. 76
6.5 Distributions of $\ln M_X^2$ at the detector level for different (W, Q^2) bins. . . . 78
6.6 The ratio of the number of the non-diffractive events predicted by Djangoh to the number of data events after the final event selection in low Q^2 bins. 83
6.7 The ratio of the number of the non-diffractive events predicted by Djangoh to the number of data events after the final event selection in medium Q^2 bins. 84
6.8 The ratio of the number of the non-diffractive events predicted by Djangoh to the number of data events after the final event selection in high Q^2 bins. 85

7.1 Acceptance corrections and purity values obtained with Satrap MC in bins of (M_X, Q^2) as a function of x_{IP} in low Q^2 bins. 89
7.2 Acceptance corrections and purity values obtained with Satrap MC in bins of (M_X, Q^2) as a function of x_{IP} in medium Q^2 bins. 90
7.3 Acceptance corrections and purity values obtained with Satrap MC in bins of (M_X, Q^2) as a function of x_{IP} in high Q^2 bins. 91
7.4 The reduced diffractive cross section multiplied by x_{IP}, $x_{\mathrm{IP}}\sigma_r^{D(3)}$, as a function of x_{IP} in different β and Q^2 regions shown in low Q^2 bins. 94
7.5 The reduced diffractive cross section multiplied by x_{IP}, $x_{\mathrm{IP}}\sigma_r^{D(3)}$, as a function of x_{IP} in different β and Q^2 regions shown in medium Q^2 bins. 95
7.6 The reduced diffractive cross section multiplied by x_{IP}, $x_{\mathrm{IP}}\sigma_r^{D(3)}$, as a function of x_{IP} in different β and Q^2 regions shown in high Q^2 bins. 96
7.7 The reduced diffractive cross section multiplied by x_{IP}, $x_{\mathrm{IP}}\sigma_r^{D(3)}$, as a function of Q^2 for different β and x_{IP} regions. 97
7.8 The ratio of the reduced diffractive cross sections $\sigma_r^{D(3)}$ obtained with the LPS and the LRG methods as a function of x_{IP} for different values of β and Q^2. 98
7.9 The Pomeron intercept $\alpha_{\mathrm{IP}}(0)$ as a function of Q^2. 101

List of Tables

3.1 HERA design parameters and performance during 1999-2000 running period. 33
3.2 Angular acceptance and longitudinal depth of the CAL modules. 38

4.1 Summary of the Monte Carlo event samples used in the analysis. 49

5.1 Calorimeter calibration correction factors. 55

A.1 The reduced diffractive cross section multiplied by x_{IP}, $x_{\mathrm{IP}}\sigma_r^{D(3)}$, as a function of x_{IP} for different values of M_X, for $Q^2 = 2.5\,\mathrm{GeV}^2$. 103
A.2 The reduced diffractive cross section multiplied by x_{IP}, $x_{\mathrm{IP}}\sigma_r^{D(3)}$, as a function of x_{IP} for different values of M_X, for $Q^2 = 3.5\,\mathrm{GeV}^2$ and $4.5\,\mathrm{GeV}^2$. . . 104
A.3 The reduced diffractive cross section multiplied by x_{IP}, $x_{\mathrm{IP}}\sigma_r^{D(3)}$, as a function of x_{IP} for different values of M_X, for $Q^2 = 5.5\,\mathrm{GeV}^2$ and $6.5\,\mathrm{GeV}^2$. . . 105
A.4 The reduced diffractive cross section multiplied by x_{IP}, $x_{\mathrm{IP}}\sigma_r^{D(3)}$, as a function of x_{IP} for different values of M_X, for $Q^2 = 8.5\,\mathrm{GeV}^2$ and $12\,\mathrm{GeV}^2$. . . . 106
A.5 The reduced diffractive cross section multiplied by x_{IP}, $x_{\mathrm{IP}}\sigma_r^{D(3)}$, as a function of x_{IP} for different values of M_X, for $Q^2 = 16\,\mathrm{GeV}^2$ and $22\,\mathrm{GeV}^2$. . . . 107
A.6 The reduced diffractive cross section multiplied by x_{IP}, $x_{\mathrm{IP}}\sigma_r^{D(3)}$, as a function of x_{IP} for different values of M_X, for $Q^2 = 30\,\mathrm{GeV}^2$ and $40\,\mathrm{GeV}^2$. . . . 108
A.7 The reduced diffractive cross section multiplied by x_{IP}, $x_{\mathrm{IP}}\sigma_r^{D(3)}$, as a function of x_{IP} for different values of M_X, for $Q^2 = 50\,\mathrm{GeV}^2$, $65\,\mathrm{GeV}^2$, and $85\,\mathrm{GeV}^2$. 109
A.8 The reduced diffractive cross section multiplied by x_{IP}, $x_{\mathrm{IP}}\sigma_r^{D(3)}$, as a function of x_{IP} for different values of M_X, for $Q^2 = 110\,\mathrm{GeV}^2$, $140\,\mathrm{GeV}^2$, $185\,\mathrm{GeV}^2$, and $255\,\mathrm{GeV}^2$. 110
A.9 The reduced diffractive cross section multiplied by x_{IP}, $x_{\mathrm{IP}}\sigma_r^{D(3)}$, as a function of Q^2 for different values of β, for $x_{\mathrm{IP}} = 0.00028$, 0.00054, and 0.001. . 111
A.10 The reduced diffractive cross section multiplied by x_{IP}, $x_{\mathrm{IP}}\sigma_r^{D(3)}$, as a function of Q^2 for different values of β, for $x_{\mathrm{IP}} = 0.002$. 112
A.11 The reduced diffractive cross section multiplied by x_{IP}, $x_{\mathrm{IP}}\sigma_r^{D(3)}$, as a function of Q^2 for different values of β, for $x_{\mathrm{IP}} = 0.0038$. 113

A.12 The reduced diffractive cross section multiplied by x_{IP}, $x_{\mathrm{IP}}\sigma_r^{D(3)}$, as a function of Q^2 for different values of β, for $x_{\mathrm{IP}} = 0.0073$. 114
A.13 The reduced diffractive cross section multiplied by x_{IP}, $x_{\mathrm{IP}}\sigma_r^{D(3)}$, as a function of Q^2 for different values of β, for $x_{\mathrm{IP}} = 0.0073$ (cont.), and 0.014. . . 115
A.14 The reduced diffractive cross section multiplied by x_{IP}, $x_{\mathrm{IP}}\sigma_r^{D(3)}$, as a function of Q^2 for different values of β, for $x_{\mathrm{IP}} = 0.014$ (cont.). 116

Chapter 1

Introduction

Quantum Chromodynamics (QCD) is a theory of strong interactions, an important part of the Standard Model of particle physics. It is a quantum field theory describing the interactions of the particles carrying colour charge, that are quarks and gluons found in hadrons. Developed in the 1970's QCD was frequently confirmed in many experimental tests. In very high-energy reactions, when short distances are accessible, the interaction between quarks and gluons becomes arbitrarily weak which is known as *asymptotic freedom*. For the discovery of this property D. J. Gross, H. D. Politzer, and F. Wilczek were awarded the Nobel Prize in Physics in 2004. Asymptotic freedom was proven rigorously what permits the predictions for the properties of strong interactions using the perturbative techniques familiar from QED. Another aspect of QCD, the so-called *colour confinement*, states that the force between colour charged particles does not diminish as they are separated. The quarks are confined with other quarks to form hadrons that are colourless. Although it has never been proven mathematically, confinement is believed to be true because it explains failures of free quark searches.

In this non-perturbative regime some global aspects of the soft hadron-hadron interactions are successfully described by Regge phenomenology [1]. In this approach the interaction is viewed in terms of the exchange of the *Regge trajectories* which are formed by the states in the angular momentum-t plane[1]—so-called *Regge poles*. In most cases Regge trajectories include states corresponding to known particles. The only exception is the Regge trajectory with the quantum numbers of the vacuum, called Pomeron (IP) trajectory [2] which is widely believed to be required to describe the diffractive scattering.

In-depth studies of the diffraction were performed for hadron-hadron interactions. Good example is the elastic diffractive scattering of two hadrons in which no quantum numbers are exchanged. The inelastic diffractive reaction, where one or both colliding hadrons are excited into a higher mass states with the same internal quantum numbers as the initial particles, is also possible. They are called the single and double diffraction

[1] t is the square of the momentum transfer between the interacting particles.

(or dissociation) respectively. Term *diffraction* was borrowed from optics. Its justification is that the diffractive hadronic processes have features similar to the ones characteristic of deflection of a beam of light by an obstacle which dimensions are comparable to the wavelength. Diffractive hadronic processes characterise a pronounced forward peak in the t-differential cross section which is exponentially suppressed. Moreover, the series of diffractive maxima and minima, noticeable at larger $|t|$ values, make the analogy even more spectacular.

First experimental confirmation of partonic structure of the Pomeron was provided with high transverse momentum jets which were observed in high mass system in diffractive $p\bar{p}$ scattering [3]. The Pomeron structure could be also probed by means of a virtual photon in deep inelastic electron-proton scattering (DIS). This opportunity was realized in 1992 when the electron-proton collider HERA was put into operation. Virtual photons have the advantage over a hadron beam in studying the Pomeron because in deep inelastic ep scattering a wide range of the interaction scale can be easily accessed.

The QCD picture of the Pomeron points to its non-universal nature. Among many concepts of a Pomeron in QCD framework the most straightforward one can be realized as the exchange of two gluons with no net colour transfer. For ep DIS, in the proton rest frame, the virtual photon emitted from the incoming electron may fluctuate into a quark-antiquark ($q\bar{q}$) pair or into a quark-antiquark-gluon ($q\bar{q}g$) state with the same quantum numbers. Then the $q\bar{q}$ or $q\bar{q}g$ state interacts with the proton via two gluons exchange and can be observed in two or three jet events respectively [4]. Since in DIS the partonic fluctuations of the virtual photon can lead to configurations of different sizes, the transition from the soft, non-perturbative Pomeron, to the perturbative one can be studied. Thus better understanding of the Pomeron and the region of interplay between non-perturbative and perturbative QCD can be reached.

The experimental signature of a Pomeron exchange is a large rapidity gap in the hadronic final state between the virtual photon and the proton fragmentation system. In other words this is a large angular region where no outgoing particles are detected. Due to a colour singlet exchange hadron radiation between the photon dissociated system and the remnant of the proton is strongly suppressed. In the dominant mechanism of DIS the colour transfer between the struck quark and the proton remnant fills the rapidity interval between them with hadrons. Significant number of large rapidity gap events in DIS ($\sim 10\%$) observed by the ZEUS [5] and H1 [6] collaborations opened a new domain of studies on diffraction and made the deep inelastic electron-proton scattering one of the best method for testing QCD models.

There are two major difficulties that can make studying diffractive scattering at HERA problematic. The first one is related to the selection of the diffractive contribution and is caused by troublesome issue to distinguish the particles produced in virtual photon dissociation from all the final state particles. The detectors installed at HERA cover mainly the photon fragmentation region whereas most of the proton fragmentation region stays beyond their reach. The second difficulty arises because not all the events which

have topological properties of diffractive scattering are due to Pomeron exchange.

This thesis presents details of the measurement of the reduced diffractive cross section in deep inelastic neutral current ep scattering. The title diffractive structure function $F_2^{D(3)}$ is equal to the reduced diffractive cross section up to corrections due to the longitudinal structure function. The large rapidity gap method has been used to extract the diffractive contribution $\gamma^* p \to Xp$. The analysis was performed on the data collected with the ZEUS detector at HERA ep accelerator in the years 1999 and 2000 when HERA collided positrons of 27.6 GeV with protons of 920 GeV. The corresponding integrated luminosity is $62.07\,\mathrm{pb}^{-1}$ which is almost 24 times higher compared to the previous inclusive measurement of diffractive DIS with large rapidity gap method made by the ZEUS collaboration [7].

The thesis is divided into 8 Chapters:

- Chapter 2 introduces the theory of deep inelastic ep scattering and the diffraction. Several theoretical models of the diffractive DIS are reviewed there.
- Chapter 3 describes briefly the HERA collider and the ZEUS detector. Components of the ZEUS detector that were essential for this analysis were considered in details.
- Chapter 4 is devoted to Monte Carlo event simulation. Several MC programs used in the analysis are described there.
- Details of event reconstruction and methods of the kinematic variables reconstruction together with the comparison of data with MC simulation are presented in Chapter 5.
- Chapter 6 deals with the event selection and problem of background processes.
- The results of the analysis are presented in Chapter 7.
- The conclusions are included in Chapter 8.

Chapter 2

Theoretical background

2.1 Deep Inelastic ep Scattering

Deep inelastic scattering (DIS) is the process in which constituents of the proton (e.g. the quarks) are probed by means of lepton-proton scattering. The interaction is *inelastic* when a quark is knocked out of the proton and the proton is broken up. It is called *deep* when the proton is probed with a gauge boson having small wavelength that it can resolve small distance scales. The interaction can be described by the exchange of photons or Z^0s, which are electrically neutral, or by the exchange of charged bosons $W^{\pm}$. These different processes are called neutral current (NC) and charged current (CC) deep inelastic scattering respectively. The studies presented in this thesis focus on the diffractive neutral current e^+p DIS events.[1]

2.1.1 Kinematics in DIS

A diagram of the neutral current deep inelastic ep scattering is shown in Fig. 2.1:

$$e(k) + p(P) \to e(k') + X(P'). \tag{2.1}$$

The incident electron with four-momentum k is scattered on the proton carrying four-momentum P. Virtual photon with four-momentum q is exchanged in the interaction. Because of the lepton number conservation, the scattered electron has to be present in the final state (having four-momentum k'). In addition, hadronic system X coming from the proton fragmentation appears. Its four-momentum is denoted by P'.

Kinematics of deep inelastic electron-proton scattering can be described by the follow-

[1] To make things simpler the incoming and scattered lepton will be referred to as electron (e), unless stated otherwise.

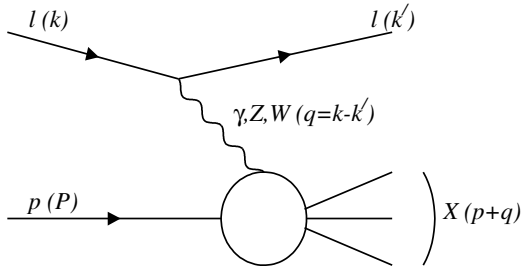

Figure 2.1: *Schematic diagram of deep inelastic lepton-proton scattering.*

ing variables:[2]

$$s = (k+P)^2 \simeq 4E_eE_p, \tag{2.2}$$

$$Q^2 \equiv -q^2 = -(k-k')^2, \tag{2.3}$$

$$x = \frac{Q^2}{2P\cdot q}, \tag{2.4}$$

$$y = \frac{q\cdot P}{k\cdot P}, \tag{2.5}$$

$$W^2 = (q+P)^2 = m_p^2 + \frac{Q^2}{x}(1-x), \tag{2.6}$$

$$\nu = \frac{q\cdot P}{m_p}. \tag{2.7}$$

The variable s is the centre-of-mass energy squared in the electron-proton system. The E_e and E_p are electron and proton beam energies respectively. Virtuality of the exchanged photon, Q^2, determines the hardness of the interaction which directly limits its resolving power. Resolution, Δb, of the proton structure probing by the virtual photons can be estimated by:

$$\Delta b \propto \frac{\hbar c}{\sqrt{Q^2}} = \frac{0.197}{\sqrt{Q^2}}\,\text{GeVfm}. \tag{2.8}$$

In the parton model the Bjorken variable x is interpreted as the fraction of the proton momentum carried by the quark struck by the virtual photon. In the proton rest frame ν is the energy transfered from the electron to the proton whereas parameter y is the fractional energy transfer which sets the inelasticity of the interaction. W^2 is the centre-of-mass energy squared of the virtual photon-proton system.

[2]Natural units, which correspond to the relation $\hbar = c = 1$ between the reduced Planck constant $\hbar$ and the speed of light in a vacuum c, will be used throughout this thesis.

The two kinematic regions can be singled out in the *ep* interactions:

- the deep inelastic scattering (DIS) regime which is defined by the following conditions:
$$Q^2 \gg m_p^2, \quad W^2 > m_p^2$$
,
- the photoproduction regime in which the exchanged photon is real or quasi-real (small values of Q^2). For this type of events, the electron may be represented like a source of real photons.

2.1.2 Cross sections and structure functions

Considering the elastic electron-proton scattering the expression for the cross section, known as the Rosenbluth formula [8], is:

$$\frac{d\sigma}{d\Omega} = \frac{\alpha^2\cos^2\frac{\theta}{2}}{4E\sin^4\frac{\theta}{2}}\frac{E'}{E}\left(\frac{G_E^2+\tau G_M^2}{1+\tau} + 2\tau G_M^2\tan\frac{\theta}{2}\right), \tag{2.9}$$

where $\tau = \frac{-q^2}{4m_p^2}$. The proton electric and magnetic form factors, G_E and G_M, can be related via Fourier transforms to the proton charge and magnetic moment distributions. If the proton were a point-like, structureless particle, these form factors would be $G_E(q^2) = G_M(q^2) = const$.

Unlike elastic scattering, where the process can be described by one parameter only (angle or Q^2), in the inelastic case two independent variables have to be used. Often chosen are the Q^2 and ν, and then the inelastic cross section can be written as [9]:

$$\frac{d^2\sigma}{dE'd\Omega} = \frac{4\alpha^2E'^2}{Q^4}\left\{W_2(\nu,Q^2)\cos^2\frac{\theta}{2} + 2W_1(\nu,Q^2)\sin^2\frac{\theta}{2}\right\}, \tag{2.10}$$

where, instead of the two form factors G_E and G_M (functions of the single variable Q^2) encountered previously, we have the inelastic form factors W_1 and W_2, that, *a priori*, are functions of both Q^2 and ν.

Observing that the structure functions $W_{1,2}$ may be expressed in terms of the absorption cross sections σ_T and σ_L for transversely and longitudinally polarised photons [10], one can rewrite the *ep* scattering cross section as:

$$\frac{d^2\sigma_{ep}(y,Q^2)}{dydQ^2} = \frac{\alpha}{y\pi Q^2}\left[\left(1-y+\frac{y^2}{2}-\frac{(1-y)Q^2_{min}}{Q^2}\right)\sigma_T(y,Q^2) + (1-y)\sigma_L(y,Q^2)\right], \tag{2.11}$$

where Q^2_{min} is the minimum kinematically allowed Q^2 value, i.e. $Q^2_{min} = m_e^2 y^2/(1-y) \approx 10^{-9}\,\mathrm{GeV}^2$. The term with Q^2_{min} can be therefore neglected and one gets:

$$\frac{d^2\sigma_{ep}}{dQ^2 dy} = \Gamma\sigma_T(1+\epsilon R), \tag{2.12}$$

where

$$\begin{aligned} \Gamma &= \frac{\alpha(1+(1-y^2))}{2\pi Q^2 y}, \\ \epsilon &= \frac{2(1-y)}{1+(1-y)^2}, \\ R &= \frac{\sigma_L}{\sigma_T}. \end{aligned} \tag{2.13}$$

The ep cross section decreases rapidly with increasing Q^2 and therefore reaches maximum for Q^2 close to zero. If one requires the structure functions $W_{1,2}$ to have a regular evolution as Q^2 approaches zero, then

$$\sigma_T \to \sigma^{tot}_{\gamma p} \qquad \text{and} \qquad \sigma_L \propto Q^2,$$

where $\sigma^{tot}_{\gamma p}$ is the total γp cross section for real photons. In this limit the cross section for longitudinally polarised photons can be neglected and one gets the so-called Weizsäcker-Williams approximation which factorizes the ep cross section in terms of the probability of photon emission from the electron and of the total γp cross section.

W_1 and W_2 are commonly presented in terms of the dimensionless structure functions F_1 and F_2:

$$\begin{aligned} F_1(\nu, Q^2) &= m_p W_1(\nu.Q^2), \\ F_2(\nu, Q^2) &= \nu W_2(\nu, Q^2), \end{aligned} \tag{2.14}$$

through which the inelastic ep cross section from Equation (2.10) becomes:

$$\frac{d^2\sigma_{ep}}{dxdQ^2} = \frac{4\pi\alpha^2}{xQ^4}\left[\left(1-y-\frac{m_p^2 xy}{s-m_p^2}\right)F_2(x,Q^2) + xy^2 F_1(x,Q^2)\right] \tag{2.15}$$

or

$$\frac{d^2\sigma_{ep}}{dxdQ^2} = \frac{4\pi\alpha^2}{xQ^4}\frac{F_2(x,Q^2)}{x}\left[1-y-\frac{m_p^2x^2y^2}{Q^2}+\frac{y^2}{2}\frac{1+4m_p^2x^2/Q^2}{1+R(x,Q^2)}\right]. \tag{2.16}$$

It is worth to note that two variables are enough to describe the whole process and all the information on the interaction is provided by the structure functions F_1 and F_2.

The first measurements in DIS, performed at SLAC [11] and at DESY [12], shown that, differently from the elastic case, the inelastic form factors are to a first approximation

independent of Q^2 and that they are functions of the variable x only. This feature, predicted by Bjorken [13], is called *scale invariance*.

We expect that a function of two variables becomes function of their ratio when they both go to infinity not only on mathematical basis, but on physical grounds as well, if the target is made of elementary subconstituents. Scale invariance was and still is the best experimental evidence that an elementary probe sees the proton (like any other hadron) as made of spin-$\frac{1}{2}$ free point-like constituents which were named partons by Feynman. In a very similar way 60 years earlier the $\sin^{-4}(\theta/2)$ behaviour in scattering experiments with α particles suggested to Rutherford and his collaborators the presence of charged point-like nuclei inside the target atom.

Just as Rutherford was only able to say that atomic nucleus has to be smaller than $\sim 10^{-13}\,\mathrm{m}$ (it took some time before it has proved that the atomic nucleus is smaller than $\sim 10^{-15}\,\mathrm{m}$), similarly nowadays we only know that partons (like leptons) are elementary particles down to $\sim 10^{-18}\,\mathrm{m}$. The answer for the question whether partons (and leptons) will keep appearing point-like at much smaller distances (i.e. much higher energy of the probe) or they will, once more, reveal to be made of even smaller components remains a mystery.

2.1.3 Quark parton model

According to Feynman's parton model [14] the proton is composed of free point-like objects called *partons*. In the infinite momentum frame, where the interactions between partons and their transverse momenta can be neglected, the proton may be depicted as a beam of partons, each having a momentum xm_p, where x is the Bjorken scaling variable. The inelastic lepton-proton scattering is interpreted in this model as elastic lepton-parton interaction.

According to the above assumptions the total ep cross section may be expressed as the incoherent sum of elastic electron-parton scattering cross sections:

$$\frac{d^2\sigma}{dxdQ^2} = \sum_i e_i^2 f_i(x)\left(\frac{d\sigma}{dQ^2}\right)_i, \tag{2.17}$$

where e_i is the electric charge of the parton i, $f_i(x)$ is the parton momentum distribution function, that is the probability of finding a parton i with momentum fraction between x and $x+dx$, and $(d\sigma/dQ^2)_i$ represents the cross section for elastic scattering on a single parton i. The parton momentum distribution has to satisfy the following condition:

$$\sum_i \int dx\, x f_i(x) = 1. \tag{2.18}$$

Since the structure function F_2 can be expressed in terms of the functions f_i:

$$F_2(x) = x\sum_i e_i^2 f_i(x), \tag{2.19}$$

one derives the so-called Callan-Gross relation [15] which is a direct consequence of the spin-$\frac{1}{2}$ partons:

$$F_2(x) = 2xF_1(x). \tag{2.20}$$

The main success of the parton model, that is explaining observed scaling phenomenon, together with confirmation of Callan-Gross relation in measurements at SLAC, led to the identification of the partons with the spin-$\frac{1}{2}$ *quarks*, introduced independently by Gell-Mann [16] and Zweig [17] in hadron spectroscopy.

2.1.4 Quantum Chromodynamics

At the beginning of 70's it turned out that naive parton model could not handle some facts.

- More accurate experiments demonstrated that scale invariance holds for approximately $x \approx 0.15$ and that significant variations of the structure function F_2 with Q^2 are observed at higher and lower values of x (see Fig. 2.2).
- If the proton consisted only of charged quarks, their momenta would be expected to add up to the proton momentum, $\sum_i \int_0^1 dx\, x f_i(x) = 1$. However experimentally a value of ~ 0.5 was found [18] which means that only half of the proton momentum is carried by charged quarks and the rest part has to be contained in neutral partons. Direct evidence for the existence of these partons, called *gluons*, was provided in 1979 at DESY via the observation of three-jet events in e^+e^- annihilation [19].
- Moreover, the fact that quarks are confined in hadrons implies the presence of strong binding between them which cannot be understood within the quantum electromagnetic theory (QED).

The explanation of above problems was brought by Quantum Chromodynamics (QCD), a field theory developed in the 1970's to describe the strong interactions. In QCD quarks are not free but interact through the exchange of spin-$\frac{1}{2}$ gauge bosons (gluons). Gluons carry colour charge and therefore couple to each other which is the main difference comparing to QED. In QCD the colour coupling constant α_S decreases at short distances, contrary to QED where the effective charge coupling increases at very small distances. The scale dependence of the strong coupling constant in leading order perturbation theory is given by: [10]

$$\alpha_S(Q^2) = \frac{12\pi}{(33 - 2n_f)\ln(Q^2/\Lambda^2)}, \tag{2.21}$$

where n_f is the number of quark flavours. The QCD scale parameter Λ determines the energy scale at which α_S becomes so large that perturbation theory breaks down. It was measured to be within the range of 100–300 MeV. At large energy scale the strong coupling constant decreases logarithmically. This behaviour is known as *asymptotic freedom*.

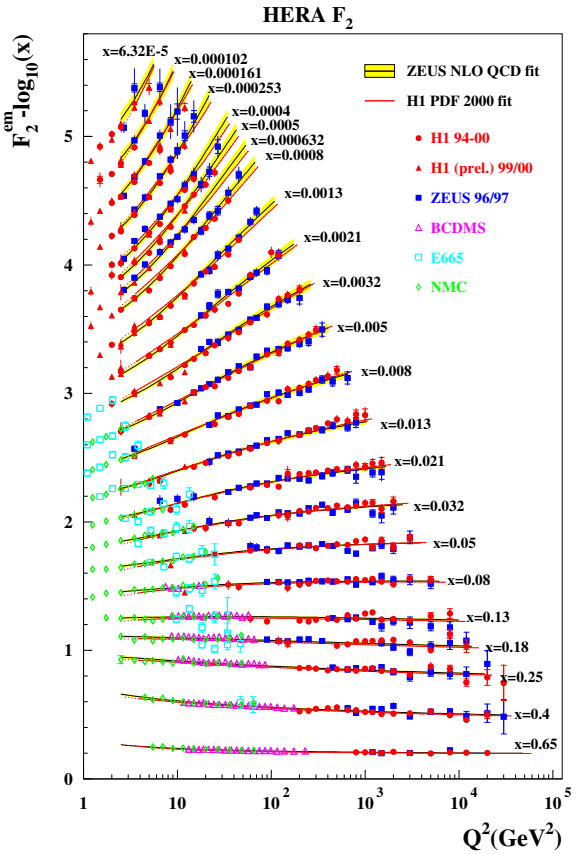

Figure 2.2: *The structure function F_2 as a function of Q^2 for different values of x. The results from ZEUS, H1, and fixed-target experiments are shown.*

According to the QCD way of expression of the deep inelastic scattering, the naive QPM needs to be improved due to the coupling of quarks to gluons. Quarks may radiate gluons which in turn may split into quark-antiquark pairs. In this case the number of partons increases and at the same time the average momentum per parton decreases. With increasing Q^2 more and more of these fluctuations can be resolved (see Fig. 2.3).

At low values of Q^2 only the valence quarks with relatively large x values, assumed by

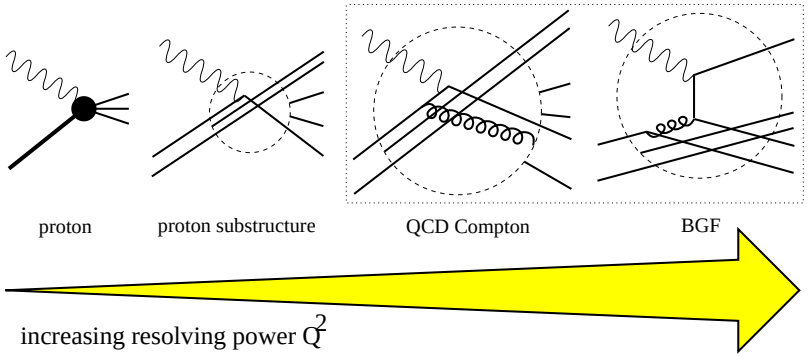

Figure 2.3: *Schematic diagram of scaling violation.*

naive QPM, dominate. In high Q^2 region gluons radiation leads to an increase of the number of quarks with small fraction x of the proton momentum and accordingly to a depletion of the high x region. In fact, at low x a rapid increase of F_2 with increasing Q^2 was observed [20] while at large x values F_2 decreases (see Fig. 2.2). The logarithmic Q^2 dependence of F_2 for fixed x is known as *scaling violations*.

Another consequence of gluon radiations is that quarks can have a transverse momentum and can couple to longitudinally polarised photons leading to the longitudinal structure function

$$F_L = F_2 - 2xF_1. \tag{2.22}$$

Thus the Callan-Gross relation is no longer satisfied exactly.

2.1.5 Evolution equations

There are four elementary vertices foreseen by QCD (see Fig. 2.4), each of them is associated with a *splitting function* which gives the probability $P_{ij}(\frac{x}{y})$ for a quark or gluon with momentum fraction x to have been originated from a parent parton with momentum fraction y. Using the splitting functions and having the parton densities $q_i(x, Q^2)$ for quarks of flavour i and $g(x, Q^2)$ for gluons given at $Q^2 = Q_0^2$, the Q^2 evolution of the parton densities (or equivalently of the structure functions) may be expressed as a differential equation in the variables x and Q^2, providing $\alpha_S(Q^2) \ll 1$ which makes perturbative calculus applicable.

Since the *evolution equations* were developed under certain approximations, they comply with different regions of x–Q^2 space (see Fig. 2.5). The DIS region, where increasing Q^2

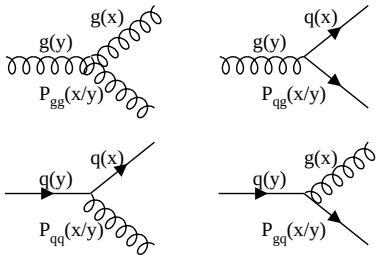

Figure 2.4: *Elementary vertices in QCD and associated splitting functions.*

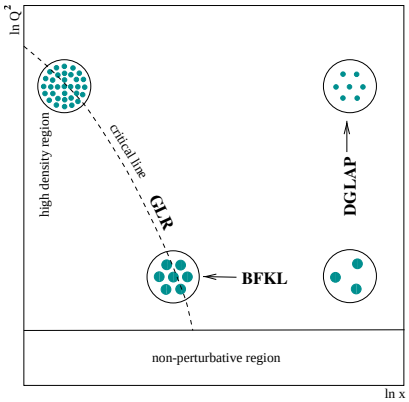

Figure 2.5: *Range of validity for various evolution equations.*

makes smaller and smaller spatial distances accessible, is well described in pQCD by the DGLAP[3] evolution equations [21, 22]. For smaller values of x and Q^2, the evolution is dominated by the gluon cascade. The BFKL[4] evolution equations [23] predict a strong increase of the gluon densities which is somehow balanced by means of recombination processes between partons. When entering the region named *transition region* pQCD is still valid, but the evolution equation must be modified by introduction of a non-linear term first proposed by Gribov, Levin, and Ryskin with the so-called GLR equations [24].

[3] Dokshitzer, Gribov, Lipatov, Altarelli, Parisi
[4] Balitzki, Fadin, Kuraev, Lipatov

Using them it is possible to calculate the *critical line* which demarcate the transition and the non-perturbative regions. At small enough x values the increase of the gluon component becomes so large that the unitarity constraint of the parton model is violated. Introduction of the non-perturbative corrections is required. However, pQCD cannot make any predictions in this region. There is a hypothesis that since at low x the gluon density is high, the gluons start to overlap in the proton and to recombine via the QCD process $gg \to g$. These *saturation effects* diminish the rise of F_2 for decreasing x.

The concept of parton evolution can be generalised by inclusion of the higher order corrections involving more than one quark-gluon vertex. It can be shown [21] that the amplitude for the inelastic process can be obtained from the sum of so-called *ladder diagrams* of consecutive gluon emissions (see Fig. 2.6). The quark which absorbs the photon

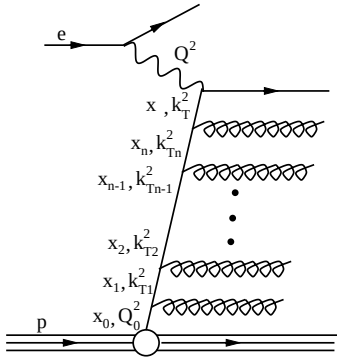

Figure 2.6: *The notation for a ladder diagram with emission of n gluons.*

evolves from the incoming proton via gluon emission losing in that way its longitudinal momentum. The longitudinal momentum fractions x_i with respect to the proton energy are decreasingly ordered, i.e. $x_0 > x_1 > \ldots > x_n > x$, while the transverse momenta of the emitted gluons increase: $Q_0^2 \ll k_{T1}^2 \ll k_{T2}^2 \ll \ldots \ll k_{Tn}^2 \ll Q^2$.

2.2 Diffraction

Term *diffraction* is derived from optics where it describes the phenomenon of deflection of a beam of light by an obstacle which dimensions are comparable to the wavelength. In the high energy physics it was firstly used to describe the elastic hadron-hadron scattering of the type $a + b \to a + b$. Later it was extended to processes where one or both colliding hadrons are transformed into multi-particle final states without exchange of quantum

numbers (except for angular momentum). These processes are: single dissociation: $a+b \to X + b$ and double dissociation $a + b \to X + Y$—see Fig. 2.7.

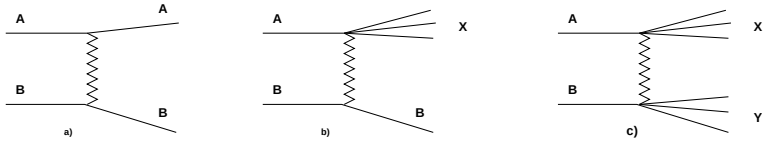

Figure 2.7: *(a) Elastic hadron-hadron scattering, (b) Single dissociation, (c) Double dissociation.*

If the colliding particle is described by a superposition of different wave components which scatter elastically on the target, the outgoing beam will contain a new superposition of the scattered wave amplitudes which in general corresponds to new physical states. In analogy with the optics the shadow which emerges when scattering a projectile on an extended target can be interpreted as the diffraction.

2.2.1 Properties of diffractive processes

Let us consider the process $a + b \to X + Y$ which can be described by two independent Mandelstam variables:

$$\begin{aligned} s &= (p_a + p_b)^2 = 4(p^2 + m^2), \\ t &= -2p^2(1 - \cos\theta), \end{aligned} \tag{2.23}$$

where p is the four-momentum in the centre of mass system, θ is the scattering angle and it is assumed that particles a and b have identical masses m.

Diffractive process characterises a pronounced *forward peak* in the elastic t-differential cross section which is exponentially suppressed. The small t region is parametrised according to:

$$\begin{aligned} \frac{d\sigma}{dt} &= \left(\frac{d\sigma}{dt}\right)_{t=0} \cdot e^{bt} \\ &\simeq \left(\frac{d\sigma}{dt}\right)_{t=0} \cdot \left(1 - b(p\theta)^2\right), \end{aligned} \tag{2.24}$$

where b is the slope of the forward peak. This relation is reminiscent of the intensity of the scattered light from a circular aperture which for small θ scattering angles is given by:

$$I = I_0 \left(1 - \frac{R^2}{4}(k\theta)^2\right), \tag{2.25}$$

where k is the photon wave number, R is the radius of the aperture, and $kR \simeq \sin\theta/\theta$. Comparing of equations (2.24) and (2.25) gives the relation between the slope b and the interaction radius R:

$$b = \frac{R^2}{4}. \tag{2.26}$$

When we look at the plot of the differential pp cross section (Fig. 2.8) the analogy to the optical case becomes even more explicit. Apart from the main peak the minimum and

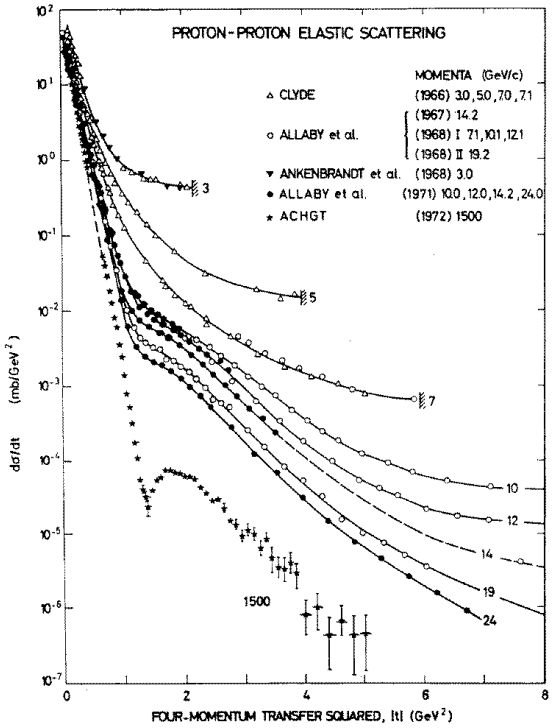

Figure 2.8: *The differential pp elastic scattering cross section $d\sigma/dt$ for different values of the centre of mass energy squared s [25].*

the secondary maximum is present in the $t > 1\,\mathrm{GeV}^2$ region. It can be observed that the

slope b increases slowly with energy s. This effect is known as *shrinkage* of the forward diffractive peak.

In the general case of the diffractive reaction $a + b \to X + Y$ no quantum numbers are exchanged in the t-channel. For partonic processes it means that no colour charge is exchanged and consistently—there is no colour field operating between products X and Y. In general these two final state systems are well separated in the phase space. This is obvious especially for elastic or single dissociation events where at least one of the incident particles experience a very small loss of its initial energy in the collision. Therefore the diffractive events are characterised by a large rapidity gap (LRG) between the quasi-elastically scattered particle and the rest of the final state. The rapidity for particle of energy E and longitudinal momentum p_L is defined by:

$$\mathcal{Y} = \frac{1}{2}\ln\frac{E + p_L}{E - p_L}, \tag{2.27}$$

which for particles with small masses is very good approximated by the pseudorapidity variable:

$$\eta = -\ln\left(\tan\frac{\theta}{2}\right), \tag{2.28}$$

where θ is the polar angle measured with respect to the direction of the incident particles.

Additional feature of the diffractive processes, foreseen by theoretical considerations, is theirs mass dependence. It was measured that for the diffractive single dissociation events $a + b \to X + b$ small masses M_X are preferred. Above the resonance region the differential cross section integrated over t falls with M_X (see Fig. 2.9):

$$\frac{d\sigma^{ab\to Xb}}{dM_X^2} \propto \frac{1}{M_X^n}, \tag{2.29}$$

with $n \approx 2$. This is a confirmation of the coherence preservation between the incoming and outgoing waves. The coherence criterion can be formulated as follows:

$$\frac{M_X^2}{s} \lesssim \frac{1}{2m_a R}, \tag{2.30}$$

where R is the longitudinal reaction radius in the rest frame of the target b.

2.2.2 Regge formalism

The soft hadron-hadron interactions are well described by Regge phenomenology [26] which is based on the formalism of the analytical continuation of the scattering amplitude into the complex values of the angular momentum. It successfully describes the energy dependence of the total hadron-hadron cross section and certain properties of elastic and diffractive scattering. The review of Regge theory can be found in [1].

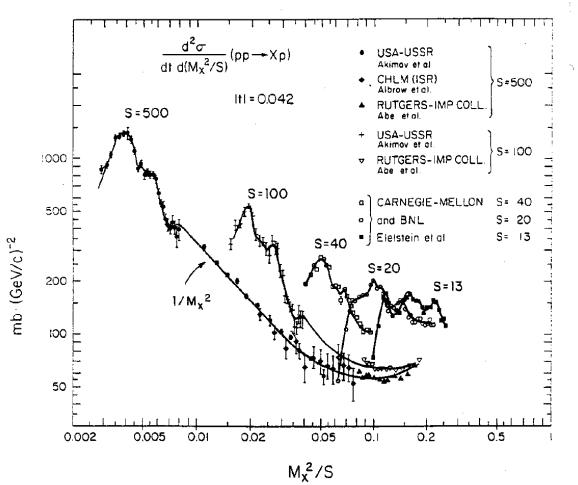

Figure 2.9: *The differential cross section for the inelastic diffractive process $pp \to Xp$ as a function of scaled diffractive mass M_X^2/s.*

In the Regge phenomenology it is assumed that collective states called *Regge poles* are exchanged in hadron-hadron interaction. A Regge pole is equivalent to a superposition of many particles with the same quantum numbers, but different spins. All exchanged particles form linear trajectories in the J–m^2 plane where J is the spin and m is the mass of the particle. The Chew-Frautschi plot [27] shows few exemplary Regge trajectories (see Fig. 2.10). The continuation of a trajectory to negative values of m^2 leads to a parametrisation in terms of the square of the four momentum transfer t:

$$\alpha(t) = \alpha_0 + \alpha' t, \tag{2.31}$$

where α_0 is the intercept and α' is the slope of the trajectory. The lightest particle on a trajectory gives the name to the trajectory itself. For most of the trajectories the slope is close to $1\,\mathrm{GeV}^{-2}$. The intercept of Regge trajectories for known particles is within the range 0–0.5, for example: $\alpha_\pi \approx 0$, $\alpha_\rho \approx 0.5$.

In the high energy limit, $s \to \infty$, and at fixed t the scattering amplitude for each Regge pole can be written as

$$A(s,t) \overset{s\to\infty}{\longrightarrow} \beta(t) \left(\frac{s}{s_0}\right)^{\alpha(t)}, \tag{2.32}$$

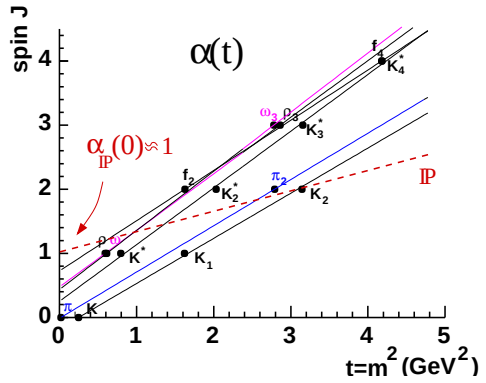

Figure 2.10: *Spin J versus mass squared for different mesons. Straight lines are the result of the linear fit and correspond to Regge trajectories.*

where $s_0 \simeq 1\,\mathrm{GeV}^2$ is the hadronic mass scale. Then the cross section of the elastic scattering process $ab \to ab$ is expressed as:

$$\frac{d\sigma}{dt} \propto \frac{1}{s^2}|A(s,t)|^2 \propto F(\beta(t)) \left(\frac{s}{s_0}\right)^{2\alpha(t)-2}, \tag{2.33}$$

where the $\alpha(t)$ in this case is the leading trajectory exchanged in elastic scattering that is the trajectory with the largest real part which contribution to the exponent of s is therefore dominant. The s-dependence of the slope b comes from the comparison to (2.24):

$$b = b_0 + 2\alpha' \ln\left(\frac{s}{s_0}\right). \tag{2.34}$$

The width of the forward peak $\Delta|t| = (b_0 + 2\alpha' \ln(s/s_0))^{-1}$ decreases as the energy increases—the shrinkage of the diffractive peak is thus explained.

Using the optical theorem, which relates the total cross section to the elastic scattering amplitude, the energy dependence of the total hadron-hadron scattering cross section is given by

$$\sigma_{tot} \sim \frac{1}{s}\mathrm{Im}[A(s,t=0)] \propto \left(\frac{s}{s_0}\right)^{\alpha_0 - 1}. \tag{2.35}$$

The total cross sections for pp, $p\bar{p}$, γp, and $\gamma\gamma$ scattering are plotted as a function of $\sqrt{s}$ in Fig. 2.11. At high energies a similar energy dependence for these processes can be seen which also applies to other hadron-hadron scattering reactions. The fall-off at low energies

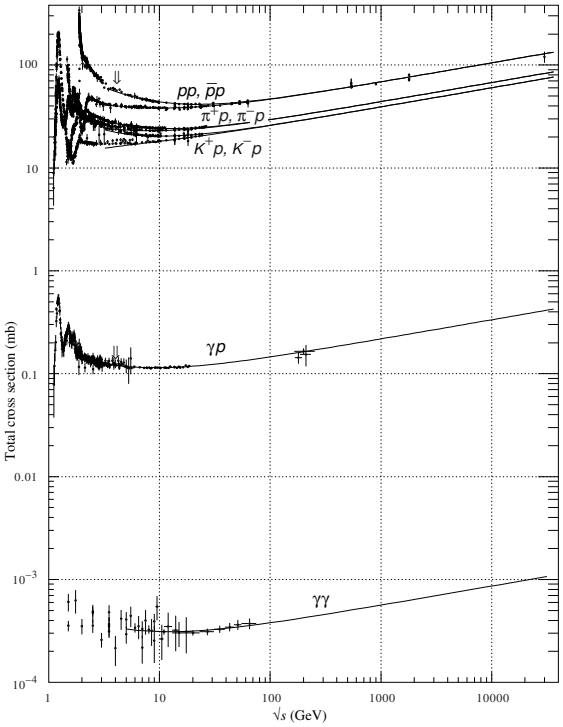

Figure 2.11: *The total cross sections for hadronic, γp, and $\gamma\gamma$ scattering as a function of $\sqrt{s}$ [28].*

in Fig. 2.11 can be explained by the exchange of Regge trajectories corresponding to known particles. The slowly increasing cross section at high energies requires a Regge trajectory with $\alpha_0 \gtrsim 1$, while all known trajectories interpolating existing particles or resonances have an intercept $\alpha_0 \lesssim 0.5$. In order to describe the data in the Regge framework one has to postulate the existence of a new trajectory. After I. Ya. Pomeranchuk the so-called *Pomeron* (IP) *trajectory* was introduced [2, 27] with $\alpha \approx 1$ (see Fig. 2.10). The Pomeron has the quantum numbers of vacuum and is generally regarded as the mediator in diffractive scattering.

The total hadron-hadron scattering cross section is successfully described by the sum

of the Reggeon and a Pomeron contributions. Donnachie and Landshoff [29] fitted all available hadronic data to the parametrisation of the form

$$\sigma_{tot} = As^{\alpha_{\mathrm{IR}}-1} + Bs^{\alpha_{\mathrm{IP}}-1}. \tag{2.36}$$

The parameters A and B depend on the particular process whereas α_{IR} and α_{IP} were fitted globally. The first term in Equation (2.36) corresponds to the Reggeon exchange responsible for the decrease of the cross section at low energies while the second one represents the Pomeron contribution which dominates at high energies. The results of the fits are: $\alpha_{\mathrm{IR}} \approx 0.55$, $\alpha_{\mathrm{IP}} \approx 1.08$. The following parametrisation of the Pomeron trajectory was obtained:

$$\alpha(t) = 1.08 + 0.25t. \tag{2.37}$$

This Pomeron trajectory which describes the weak dependence of the total cross section is known as a *soft Pomeron*.

The total, elastic, and single diffractive cross sections are expressed in terms of Regge trajectories $\alpha_i(t)$ and their couplings to hadrons $\beta(t)$ called *residue functions*. In the Regge limit, defined as $t \ll M_X^2 \ll s$, the following formulae for the cross sections in the hadron-hadron interactions hold:

$$\sigma_{tot}^{ab} = \sum_k \beta_{ak}(0)\beta_{bk}(0)s^{\alpha_k(0)-1}, \tag{2.38}$$

$$\frac{d\sigma_{el}^{ab}}{dt} = \sum_k \frac{\beta_{ak}^2(t)\beta_{bk}^2(t)}{16\pi} s^{2(\alpha_k(t)-1)}, \tag{2.39}$$

$$\frac{d^2\sigma_{diff}^{ab}}{dtdM_X^2} = \sum_{k,l} \frac{\beta_{ak}^2(t)\beta_{bl}(0)g_{kkl}(t)}{16\pi} \frac{1}{M_X^2} \left(\frac{s}{M_X^2}\right)^{2(\alpha_k(t)-1)} \left(M_X^2\right)^{\alpha_l(0)-1}, \tag{2.40}$$

where the sum runs over all contributing Regge trajectories. Equation (2.40) is based on Mueller's generalisation of the optical theorem [30] which relates the total cross section of two body scattering with the imaginary part of the forward elastic amplitude ($ab \to ab$) to the three body scattering. The term g_{kkl} is called the triple-Regge coupling. Calculations of above cross sections are illustrated in Fig. 2.12.

It can be assumed that at high energy only Pomeron exchange contributes. We can take its trajectory as

$$\alpha_{\mathrm{IP}}(t) = 1 + \epsilon + \alpha'_{\mathrm{IP}}t. \tag{2.41}$$

Since the t distribution in elastic scattering case can be approximated by the exponential function:

$$\beta_{a\mathrm{IP}}(t) = \beta_{a\mathrm{IP}}(0) \cdot e^{b_a t}, \tag{2.42}$$

where b_a is an effective slope of the elastic form factor of particle a and is related to the average radius squared of the density distribution, we can rewrite the cross section (2.40)

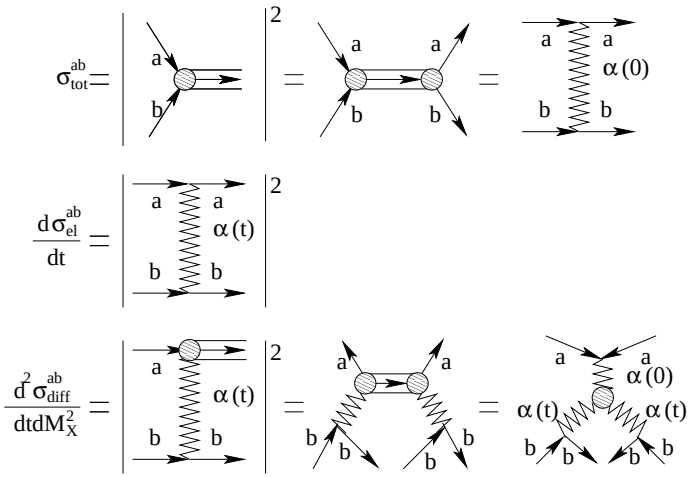

Figure 2.12: *Regge diagrams for the total, elastic, and single diffractive hadron-hadron scatterings.*

in following way:

$$\frac{d^2\sigma^{ab}_{diff}}{dtdM_X^2} = \frac{\beta^2_{a\mathrm{IP}}(0)\beta_{b\mathrm{IP}}(0)g_{\mathrm{IPIPIP}}(t)}{16\pi}\frac{1}{M_X^2}\left(\frac{s}{M_X^2}\right)^{2\epsilon}\left(M_X^2\right)^{\epsilon}e^{b_{sd}t}, \tag{2.43}$$

where

$$b_{sd} = 2b_a + 2\alpha'_{\mathrm{IP}}\ln\frac{s}{M_X^2}. \tag{2.44}$$

Now, if we take $\epsilon = 0$, all properties of the diffractive processes, i.e. no energy dependence of the cross section, $1/M_X^2$ dependence on the dissociated mass, and an exponential slope in the t distribution which shrinks with s, will be reproduced by the Equation (2.43).

The triple Regge formula has the factorisation property which allow the diffractive differential cross section to be separated into two terms,

$$\frac{d^2\sigma^{ab}_{diff}}{dtdM_X^2} = f_{\mathrm{IP}/a}(x_{\mathrm{IP}},t)\cdot\sigma_{b\mathrm{IP}}(M_X^2), \tag{2.45}$$

where $x_{\mathrm{IP}} = M_X^2/s$. The first term is called the Pomeron flux while the second one can be considered as the total cross section for bIP interactions. This decomposition is arbitrary

as far as constant factors are concerned, as the IP is not a real particle. The Pomeron flux factor is usually defined as

$$f_{\mathrm{IP}/a}(x_{\mathrm{IP}},t) = \frac{N}{16\pi}\beta^2_{a\mathrm{IP}}(t)x_{\mathrm{IP}}^{1-2\alpha_{\mathrm{IP}}(t)}, \tag{2.46}$$

with $N = 1$ [31] or $N = 2/\pi$ [32].

2.2.3 Diffractive photoproduction

The first γp experiments from 1960's [33] shown considerable similarities to the hadron-hadron interactions notably in the s dependence of the total cross section (see Fig. 2.11). The possible explanation provided by the Vector Dominance Model (VDM) [34] is based on the assumption of hadronic structure of the photon. According to that the photon is considered as a superposition of a bare photon $|\gamma_b\rangle$ and hadronic state $|h\rangle$:

$$|\gamma\rangle = \sqrt{Z_3}|\gamma_b\rangle + \sqrt{\alpha}|h\rangle, \tag{2.47}$$

where α is the fine structure constant and Z_3 is the proper normalisation constant. The hadronic component $|h\rangle$ dominates due to large hadron-hadron cross section. Conservation laws require that the hadronic state has the same quantum numbers as the photon. In the VDM it is assumed that to the state $|h\rangle$ contribute three lightest vector mesons ρ^0, ω, ϕ and that the bare photon $|\gamma_b\rangle$ does not contribute to the γ-hadron interaction. Later, in Generalised Vector Dominance Model (GVDM) [35], more constituents to the hadronic component were introduced.

The photoproduction of vector mesons can be explained within the VDM in the following way. The uncertainty principle enables fluctuations of the photon into a $q\bar{q}$ state with the same quantum numbers which makes the vector meson. The lifetime of this fluctuation is

$$t_f \approx \frac{2E_\gamma}{Q^2 + M_V^2}, \tag{2.48}$$

where E_γ is the photon energy in the proton rest frame and M_V is the mass of the vector meson V. The Vp interaction time is approximately given by $t_i = 2R_p$ where R_p is the radius of the proton. Now, for $t_f \gg t_i$ the γp scattering can be regarded as a fluctuation of the photon into a vector meson V which then interacts with the proton. In other words, the photon interacts as if it was a hadron.

By analogy to hadron-hadron case the γp diffractive scattering can be classified into four processes, depending on the final states (see Fig. 2.13). The photon can fluctuate into a vector meson with the quantum numbers of the photon, where the proton either stays intact (*elastic vector meson production*) or dissociates into a system Y (*proton dissociative vector meson production*). The photon can also dissociate into a high-mass system X. In this case the proton can either stay intact or dissociate into a Y system.

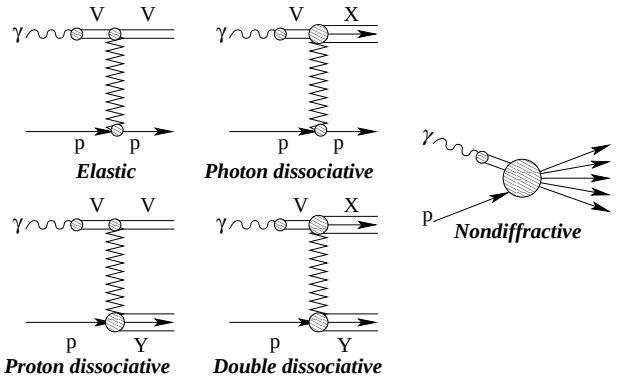

Figure 2.13: *Diagrams illustrating the classification of diffractive processes in γp scattering. For comparison a diagram for a non-diffractive process is also shown.*

2.2.4 Diffraction in DIS

Regge theory gives a unified description of the pre-HERA diffractive data and HERA photoproduction data within a non-perturbative, phenomenological approach. Both cases go under the name of soft diffraction dominated by peripheral long-range processes with small transverse momenta. Factorisation treats the Pomeron as a quasi-hadron and suggests the possibility of its partonic structure. Regge formalism, however, provides no insight into the microscopic structure of the Pomeron and the nature of its interactions. In order to study the partonic structure of the Pomeron a hard scattering with short-range interactions is needed. By hard scattering we mean that there is at least one large scale in the problem which enables the application of perturbative QCD.

For diffractive deep inelastic scattering the hard scale is provided by the photon virtuality Q^2. The final state of a standard DIS event consists of the scattered electron, the current jet, originating from the parton struck by the virtual photon, and of the proton debris. The gap in rapidity between the struck parton and the proton remnant is exponentially suppressed due to parton radiation in the resulting QCD colour field (see Fig. 2.14a).

However, soon after the HERA experiments started, a different type of hadronic final state was observed. In these events only the scattered electron and particles in the direction of the struck parton were detected. The rest of the hadronic activity was thought to escape through the beam pipe in the outgoing proton direction. The events shown a gap in the longitudinal phase space between the two groups of the low mass hadronic systems (see Fig. 2.14b). This signature was attributed to a diffractive exchange between

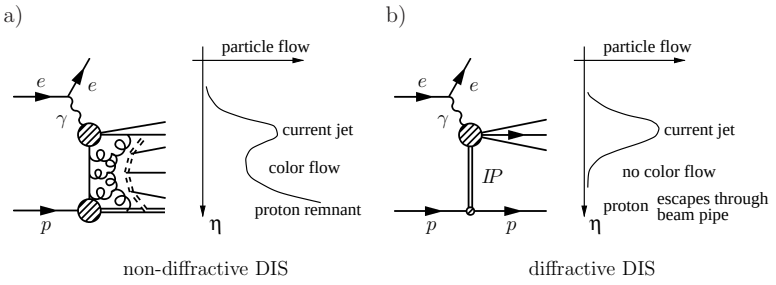

Figure 2.14: *Event topologies and particle flow diagrams for non-diffractive deep inelastic scattering event (a) and for diffractive DIS event (b).*

the photon and the proton. Due to a colour singlet exchange parton radiation between the current jet and the proton remnant is strongly suppressed. The appearance of events with large rapidity gap in NC DIS was reported by ZEUS [5] and H1 [6] experiments. It was a surprise that as much as 10% of such events was observed, even at high Q^2. Deep inelastic scattering where the Q^2 and the γp centre of mass energy W can be varied over a wide range in a well defined manner in a single experiment provides an ideal testing ground for QCD models of diffractive scattering.

Except the usual DIS variables the diffractive DIS process $e(k) + p(P) \rightarrow e'(k') + p'(P') + X$ (see Fig. 2.15) is described by the additional ones. X is the hadronic system, which results from virtual photon dissociation. If the proton dissociates into higher mass state it will be denoted by N. The four momentum transfer squared at the proton vertex is defined as:

$$t = (P - P')^2, \tag{2.49}$$

where P and P' are the four-momenta of incoming and outgoing proton respectively. The mass M_X of the hadronic system X is the second independent variable. Alternatively, the x_{IP} and β variables could be used:

$$x_{\mathrm{IP}} = \frac{(P - P') \cdot q}{p \cdot q} \approx \frac{M_X^2 + Q^2}{W^2 + Q^2}, \tag{2.50}$$

$$\beta = \frac{Q^2}{2(P - P') \cdot q} = \frac{x}{x_{\mathrm{IP}}} \approx \frac{Q^2}{M_X^2 + Q^2}, \tag{2.51}$$

where the approximations hold for small values of t. In a model with Pomeron exchange in the t channel x_{IP} is the fraction of the proton momentum carried by the Pomeron while β corresponds to the momentum fraction of the struck quark within the Pomeron.

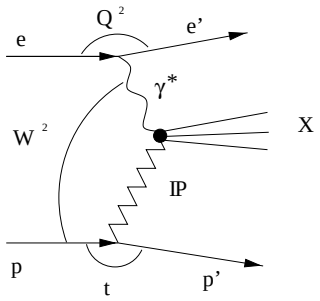

Figure 2.15: *Diagram of a diffractive DIS event where the virtual photon dissociates.*

The diffractive cross section can be expressed by the diffractive four-fold structure function which is defined by analogy to inclusive structure function of the proton (2.16):

$$\frac{d^4\sigma_{ep}^{diff}}{dQ^2 d\beta dx_{\mathrm{IP}} dt} = \frac{2\pi\alpha^2}{\beta Q^4}\left(1+(1-y)^2\right) F_2^{D(4)}(Q^2,\beta;x_{\mathrm{IP}},t), \tag{2.52}$$

or similarly:

$$\frac{d^4\sigma_{ep}^{diff}}{dQ^2 dx dx_{\mathrm{IP}} dt} = \frac{2\pi\alpha^2}{xQ^4}\left(1+(1-y)^2\right) F_2^{D(4)}(Q^2,x;x_{\mathrm{IP}},t), \tag{2.53}$$

where α is the electromagnetic coupling constant. Note that in (2.52) and (2.53) the contributions of the longitudinal structure function and the effects of the Z^0 exchange were neglected.

It is also worthwhile to introduce the three-fold structure function $F_2^{D(3)}$ where an integrations over t of the previous equations were performed:

$$\frac{d^3\sigma_{ep}^{diff}}{dQ^2 d\beta dx_{\mathrm{IP}}} = \frac{2\pi\alpha^2}{\beta Q^4}\left(1+(1-y)^2\right) F_2^{D(3)}(Q^2,\beta;x_{\mathrm{IP}}). \tag{2.54}$$

In Pomeron type models it is expected that the diffractive structure function factorizes into two parts:

$$F_2^{D(4)}(Q^2,x;x_{\mathrm{IP}},t) = f_{\mathrm{IP}/p}(x_{\mathrm{IP}},t)\cdot F_2^{\mathrm{IP}}(\beta,Q^2), \tag{2.55}$$

where $f_{\mathrm{IP}/p}(x_{\mathrm{IP}},t)$ is the flux of the Pomerons emitted from the proton and $F_2^{\mathrm{IP}}(\beta,Q^2)$ is the Pomeron structure function describing the γIP vertex. In Regge models the Pomeron flux is expected to be:

$$f_{\mathrm{IP}/p}(x_{\mathrm{IP}},t) \approx f(t)\cdot(1/x_{\mathrm{IP}})^{2\alpha_{\mathrm{IP}}(t)-1}. \tag{2.56}$$

In the Ingelman and Schlein model [31] the Pomeron consists of partons like a standard hadron. Here the virtual photon probes its structure. In analogy to the proton structure function, the Pomeron structure function $F_2^{\mathrm{IP}}(\beta,Q^2)$ can then be interpreted as the probability to find a parton inside the Pomeron which carries a momentum fraction β of the Pomeron.

2.2.5 Diffractive Parton Distribution Functions

In the leading $\log(Q^2)$ approximation the cross section for the diffractive process $\gamma^* p \to p'X$ can be written as a convolution of the universal partonic cross section $\hat{\sigma}^{\gamma^* i}$ with the diffractive parton distribution f_i^D (diffractive PDF) representing the probability to find in a proton a parton of type i under the condition that the proton undergoes a diffractive scattering:

$$\frac{d^2\sigma(x,Q^2,x_{\mathrm{IP}},t)^{\gamma^* p\to p'X}}{dx_{\mathrm{IP}}dt} = \sum_i \int_x^{x_{\mathrm{IP}}} d\xi \hat{\sigma}^{\gamma^* i}(x,Q^2,\xi) f_i^D(\xi,Q^2,x_{\mathrm{IP}},t), \tag{2.57}$$

where the integration variable ξ is the momentum fraction of the struck parton in the proton. The hard scattering factorisation formula for diffractive DIS holds for large enough Q^2 and fixed x, x_{IP}, and t. This *ansatz* was first introduced in [36] and applied to hard diffraction in [37]. The proof for (2.57) for inclusive diffractive lepton-hadron scattering was given in [38] in the framework of a scalar model and in [39] for full QCD. The diffractive PDFs are not known from first principles, though they should evolve with DGLAP [21, 22] evolution equations. They present a necessary input for any calculations of the cross sections for inclusive diffractive processes at the LHC[5]—an important background to exclusive diffractive reactions (see e.g. [40, 41]).

2.2.6 Models of diffraction in DIS

Aligned jet model

The presence of diffraction in DIS was first predicted by Bjorken and Kogut [42] based on the Aligned Jet Model (AJM). The virtual-photon proton interaction is considered in the proton rest frame. In this frame the photon fluctuates into a $q\bar{q}$ state which undergoes hadronic interactions with the proton as in the Vector Dominance Model. However, if all configurations of the hadronic fluctuation were contribute to the total $\gamma^* p$ cross section $\sigma_{\gamma^* p}^{tot}$ in a universal manner, $\sigma_{\gamma^* p}$ would be Q^2 independent leading to scaling violation of the structure function $F_2 \propto Q^2\sigma_{\gamma^* p}$. Bjorken suggested to overcome the scaling violation by requiring that only $q\bar{q}$ configurations where the p_t of the $q(\bar{q})$ relative

[5]Large Hadron Collider—a particle accelerator and collider located at CERN (currently under construction).

to the photon axis is small (aligned jet configurations) contribute to the $\gamma^* p$ cross section. The low-p_t configurations correspond to extended, hadron like objects which give also rise to a substantial diffractive cross section.

A simple explanation of the above suppression [43–45] can be found in QCD models. The effective colour charge of a $q\bar{q}$ pair is small due to screening of one parton by the other. This phenomenon is known as *colour transparency*.

QCD inspired models

Since the first observation of diffractive events in DIS at HERA many attempts have been made to develop QCD based models of diffraction. The most popular approaches are roughly described below.

Regge factorisation and QCD: This class of models follows the idea of Ingelman and Schlein [31] who proposed to investigate the partonic structure of the Pomeron through the $p\bar{p} \to X\bar{p}$ reaction. The basic idea is that the Pomeron consists of partons which can be probed in hard scattering processes and whose densities have to be determined directly from the data. With the assumption that the process can be decomposed into the emission of a Pomeron by the proton and its subsequent hard interaction with the antiproton, the cross section can be calculated with QCD techniques.

The diffractive structure function $F_2^{D(4)}$ can be factorized as:

$$F_2^{D(4)}(\beta, Q^2, x_{\mathrm{IP}}, t) = f^{\mathrm{IP}}(x_{\mathrm{IP}}, t) F_2^{\mathrm{IP}}(\beta, Q^2), \tag{2.58}$$

where $f^{\mathrm{IP}}(x_{\mathrm{IP}}, t)$ is the Pomeron flux which depends only on x_{IP} and t, and F_2^{IP} is the Pomeron structure function:

$$F_2^{\mathrm{IP}}(\beta, Q^2) = \sum_i e_i^2 \left[\beta q_i(\beta) + \beta \bar{q}_i(\beta)\right]. \tag{2.59}$$

The variable β represents, in complete analogy with x for the proton, the parton momentum fraction probed in the IP by the virtual photon and $q_i(\bar{q}_i)$ are the parton densities for the quarks (antiquarks) of flavour i. If one considers the Pomeron to be composed exclusively of gluons these densities originate from the splitting $g \to q\bar{q}$. According to Regge phenomenology the Pomeron flux has the form:

$$f^{\mathrm{IP}}(x_{\mathrm{IP}}, t) \propto x_{\mathrm{IP}}^{1-2\alpha_{\mathrm{IP}}(t)} B_{\mathrm{IP}}^2(t), \tag{2.60}$$

where $B_{\mathrm{IP}}(t)$ is the Pomeron coupling to the proton [46]. On the other hand the Pomeron structure function does not depend on x_{IP}. The x_{IP}-dependence of the diffractive structure function is fully described by (2.60) and turns out to be

$$F_2^{D(4)} \propto \left(\frac{1}{x_{\mathrm{IP}}}\right)^{2\alpha_{\mathrm{IP}}(t)-1}. \tag{2.61}$$

Perturbative QCD and colour dipole interactions: The simplest realization of the Pomeron in QCD is a colour singlet two gluon state [47]. In perturbative QCD approaches [48–50] the photon, seen in the proton rest frame, fluctuates into different hadronic states, the leading contributions being a $q\bar{q}$ pair and $q\bar{q}g$ system. Thus the wave function of the photon can be expressed as:

$$|\gamma\rangle = |\gamma\rangle_{bare} + |q\bar{q}\rangle + |q\bar{q}g\rangle + \ldots. \tag{2.62}$$

The interaction with the proton is calculated as a t-channel exchange of a colour singlet two gluon state. The models differ in the treatment of QCD corrections and in the choice of the gluon density in the proton.

In the colour dipole approach the $q\bar{q}$ fluctuation of the photon interacts with the proton as a colour dipole—first advocated by Nikolaev et al. [51]. In [43] this concept was extended to more complicated hadronic states. The calculation is performed in a kinematic regime where perturbative QCD is applicable and then extrapolated into the soft region.

Saturation model: The saturation model developed by Golec-Biernat and Wüsthoff [52] is related to the colour dipole models. It considers saturation effects occurring when the photon wavelength $1/Q$ reaches the size of the proton at small Q^2. A second kind of saturation appears in the low x region where the parton density is very high and recombination effects limit a further growth of the density. A simple *ansatz* for the dipole-proton cross section $\hat{\sigma}$ is made:

$$\hat{\sigma} = \sigma_0 \left[1 - \exp\left(\frac{-r^2}{4R_0^2(x)}\right)\right], \tag{2.63}$$

where r denotes the transverse $q\bar{q}$ separation, R_0 is a x-dependent saturation scale $R_p^2(x) = (x/x_0)^\lambda$ in GeV^{-2}, and σ_0, x_0 and λ are free parameters. The inclusive $\gamma^* p$ cross section for transversely (T) and longitudinally (L) polarised photons is given by:

$$\sigma_{T,L}(x, Q^2) = \int d^2r \int_0^1 dz \left|\Psi_{T,L}(z, r)\right|^2 \hat{\sigma}\left(x, r^2\right), \tag{2.64}$$

where z is the longitudinal momentum fraction of the photon carried by the quark and $\Psi_{T,L}$ is the photon wave function. Then the cross section for diffractive DIS can be written as

$$\frac{\sigma_{T,L}^D}{dt}(t=0) = \frac{1}{16\pi} \int d^2r \int_0^1 dz \left|\Psi_{T,L}(z, r)\right|^2 \left|\hat{\sigma}\left(x, r^2\right)\right|^2. \tag{2.65}$$

After determining the free parameters σ_0, x_0, and λ from fits to total $\gamma^* p$ cross sections the diffractive cross section can be predicted. The model is found to reproduce the measured diffractive cross section surprisingly well [44].

Soft colour interactions and semi classical approach: Motivated by the observation of a close similarity between the x and Q^2 dependence of the diffractive and the inclusive DIS cross section at small x the model of soft colour interactions (SCI) [53] assumes that the same hard partonic processes underlie both cross sections. In the proton rest frame the photon fluctuates into a $q\bar{q}$-state which interacts with the proton. After this hard interaction the $q\bar{q}$ pair propagates through the colour field of the proton. Through the exchange of soft gluons, which do not affect the kinematics of the process, the colour of the $q\bar{q}$ pair changes randomly. The probability that the $q\bar{q}$ pair, which is originally produced in a colour octet state, evolves into a colour singlet state is 1/9 given by the statistical weight factor accounting for all possible colour states. In the case that a colour singlet state is created, there is no colour flow between the $q\bar{q}$ pair and the proton remnant. The colour singlet state fragments independently of the proton remnant yielding a gap in rapidity which is a characteristic feature of diffractive events. The SCI model predicts that the ratio of the diffractive and the non-diffractive DIS cross section is $\sim 1/9$ independent of Q^2 and W which is in agreement with experiment.

The semi classical approach [45] is based on the SCI model. The interaction of the $q\bar{q}$-state with the colour field of the proton is treated in the eikonal approximation. Also higher Fock states in the photon wave function, such as $q\bar{q}g$ states, are included in the calculations.

Chapter 3

The experimental setup

3.1 The HERA accelerator

The *Hadron Elektron Ring Anlage* (HERA) circular collider is unique in the world due to type of the beams that it collides: lepton (electrons or positrons) and protons. It is located at *Deutsches Elektronen Synchrotron* laboratory (DESY) in Hamburg, Germany. Its construction started in 1984, it was commissioned in 1991, and data taking began in June 1992.

Two separate rings for electrons and protons are situated in the 6.3 km long tunnel, 10–25 m underground. The proton ring uses superconducting magnets operating at ≈ 4 K to produce the strong magnetic field (4.68 T) necessary to bend the high energy proton beam. Less energetic lepton beam is led by means of conventional magnets.

The layout of the HERA accelerator complex with four experiments is shown in Fig. 3.1. The beams are brought to collision at zero crossing angle in two experimental halls, housing H1 and ZEUS general purpose detectors. Two fixed-target experiments, HERA-B and HERMES, make use of the proton and electron beams respectively. HERA-B was designed to study $\mathcal{CP}$-violation in the $B^0\overline{B^0}$-system. The B-mesons are produced by the interaction of protons from the beam halo with a fixed tungsten wire target. The HERMES experiment studies the spin structure of the nucleon using the scattering of longitudinally polarised electrons or positrons on a jet of polarised gas targets such as hydrogen, deuterium or ^{3}He.

The production of a proton beam starts from ionising hydrogen, thus creating H^- ions which are accelerated to a 50 MeV in a linear accelerator LINAC. While passing through a thin golden foil the ions are stripped off electrons and then the proton beam is injected to the proton synchrotron DESY III. After acceleration to 7.5 GeV, the protons are transferred to the PETRA storage ring where they are further accelerated to 40 GeV. Finally, they are injected to HERA and reach their target energy.

Electrons are obtained from a hot filament whereas positrons are produced by a pair

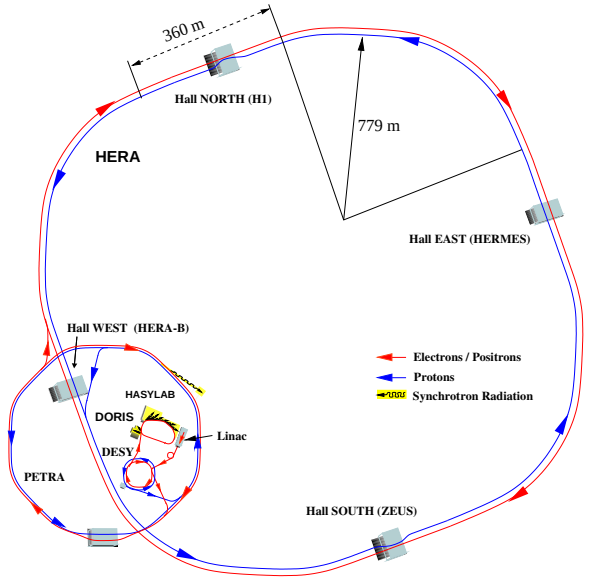

Figure 3.1: *The HERA accelerator complex and four experiments: ZEUS (South hall), H1 (North hall), HERMES (East hall), and HERA-B (West hall).*

production from bremsstrahlung photons coming from an electron beam. After collection, the electron or positron beam is accelerated by the two linear accelerators LINAC I and II to energy of 450 MeV and injected to the DESY II storage ring. Then, beam is accelerated to 7.5 GeV, transferred to PETRA II, and accelerated to 12 GeV. After injection to HERA lepton beam achieves final energy.

HERA can be filled with up to 210 electron and proton bunches with 96 ns spacing. In practice not all bunches are filled—non colliding (unpaired) bunches allow to estimate beam related background and empty bunches can be used to measure cosmic ray background rates.

From mid 1994 to 1997 HERA accelerated positrons instead of electrons due to lifetime problems. It switched to electrons for the period of 1998-99, then in mid 1999 back to positrons. In 1998 HERA increased also the proton beam energy from the design value of 820 GeV to 920 GeV. The integrated luminosities for these three data taking periods are shown in Fig. 3.2. The design parameters of HERA accelerator are summarised in Table 3.1.

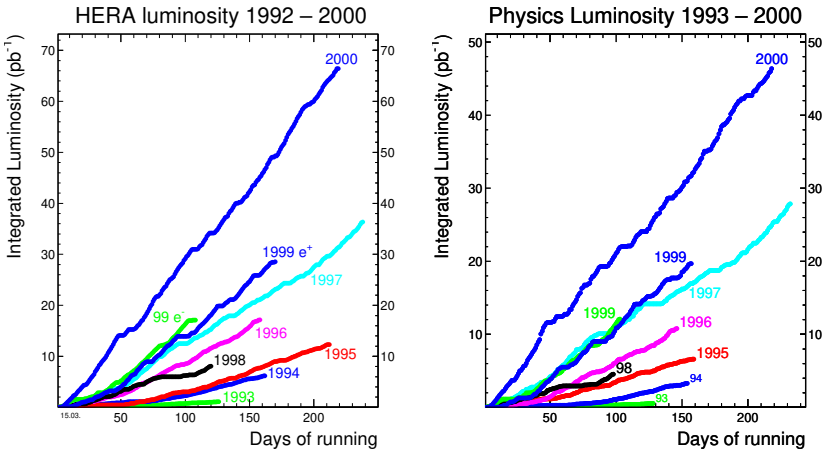

Figure 3.2: *The integrated luminosity delivered by HERA (left) and collected by the ZEUS detector (right) during the 1993-2000 running periods.*

3.2 The ZEUS detector

ZEUS is a multi-purpose magnetic detector designed to study properties of electron-proton interactions at HERA. It provides a nearly full calorimetric coverage of the interaction region (solid angle coverage $> 99.6\%$). Structure of the detector reflects the asymmetry of the ep final-state resulting from the difference of the beam energies. The ZEUS coordinate system is defined as a right-handed orthogonal system with the origin at the nominal interaction point, the z-axis pointing the proton beam direction (defining the forward direction), the x-axis pointing towards the centre of the HERA ring and y-axis taken upwards in the vertical direction. The polar angle θ is measured with respect to the forward direction and the azimuthal angle ϕ with respect to the x-axis.

An outline of the major detector components is given below followed by a more detailed description of the components important for this analysis. Broad and complete description of the ZEUS detector can be found in [54]. Figures 3.3 and 3.4 show the longitudinal and transverse layouts of the detector.

The tracking system is situated in the centre of the ZEUS detector. A large wire chamber, the Central Tracking Detector (CTD), is surrounded by a superconducting

Table 3.1: *HERA design parameters and performance during 1999-2000 running period.*

HERA parameters	Design values		1999-2000 values	
	$e^{\pm}$	p	$e^{\pm}$	p
Circumference (m)	6336			
Time between bunch crossing (ns)	96			
Injection energy (GeV)	14	40	12	40
Maximum current (mA)	58	160	37	99
Energy (GeV)	30	820	27.5	920
Centre of mass energy (GeV)	314		318	
Horizontal beam size (mm)	0.301	0.276	0.200	0.200
Vertical beam size (mm)	0.067	0.087	0.054	0.054
Longitudinal beam size (mm)	8	110	8	170
Max. specific luminosity ($\mathrm{cm^{-2}\,s^{-1}\,mA^{-2}}$)	$3.6 \cdot 10^{29}$		$9.9 \cdot 10^{29}$	
Max. instantaneous luminosity ($\mathrm{cm^{-2}\,s^{-1}}$)	$1.5 \cdot 10^{31}$		$2.0 \cdot 10^{31}$	
Integrated luminosity per year ($\mathrm{pb^{-1}}$)	35		83/3	

solenoid providing an axial magnetic field of 1.43 T. Forward and Rear Tracking chambers (FDET and RDET) provide additional tracking information outside the central region.

The tracking system is surrounded by the high resolution Uranium Calorimeter (CAL). The CAL is divided into three sections: the FCAL in the forward direction, the RCAL in the rear direction, and the BCAL, a barrel section surrounding the central region. In front of the FCAL and RCAL, and more recently of the BCAL, the layer of scintillator tiles (the Presampler) improves the accuracy of energy measurement by correcting for energy losses due to showers in the inactive material in front of the calorimeter. The Small Rear Tracking Device (SRTD) is situated behind the RDET and covers the face of the RCAL to a radius of $\sim 34\,\mathrm{cm}$ around the centre of the beam-pipe hole. It improves the detection of positrons at small angles. At a longitudinal depth of 3 radiation lengths in the RCAL and FCAL, the Hadron Electron Separator (HES) consisting of $3 \times 3\,\mathrm{cm}^2$ silicon diodes is installed for the discrimination between electromagnetic and hadronic showers originating from low energetic particles ($< 5\,\mathrm{GeV}$). In the beam hole of the RCAL there is the Beam Pipe Calorimeter (BPC) which extends the acceptance for positrons scattered at small angles. The Forward Plug Calorimeter (FPC) reduces the beam hole in the FCAL from $20 \times 20\,\mathrm{cm}^2$ to a radius of about 2.5 cm and extends the acceptance of the calorimeter by one unit of pseudorapidity.

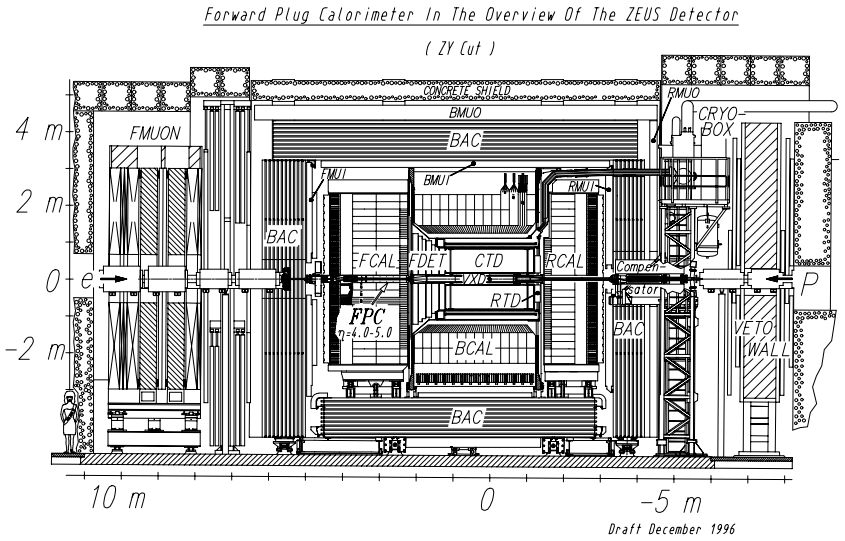

Figure 3.3: *The longitudinal cut of the ZEUS detector.*

The CAL is surrounded by Muon Identification Chambers (FMUI, BMUI and RMUI) on the inner side of the iron yoke. The yoke itself serves as absorber for the Backing Calorimeter (BAC), which measures the energy of late showering particles, and as the return path for the solenoid magnetic flux. BAC is also capable of detecting muons. On the other side of the yoke, the outer muon chambers are installed (FMUON, BMUON, RMUON).

Behind the main detector, at $z = -7.3\,\mathrm{m}$ an iron/scintillator VETO wall is used to reject beam related background. The C5 beam monitor, a small lead-scintillator counter located around the beam pipe at $z = -3.15\,\mathrm{m}$, monitors the synchrotron radiation coming from the beams as well as the longitudinal structure of the proton and electron bunches.

Even if the ZEUS apparatus covers most of the solid angle, some particles produced in ep collisions escape to the forward and rear beam-pipe holes. Some detectors have been therefore placed along the beam-lines in order to tag particles scattered at very small angles. Six stations of silicon strip detectors located at z = 26-96 m are mounted very close to the beam line and form the Leading Proton Spectrometer (LPS). It measures very forward scattered protons at the transverse momentum of less than $\sim 1\,\mathrm{GeV}$. Located at $z = 105.6\,\mathrm{m}$ the Forward Neutron Calorimeter (FNC), a lead-scintillator calorimeter, is

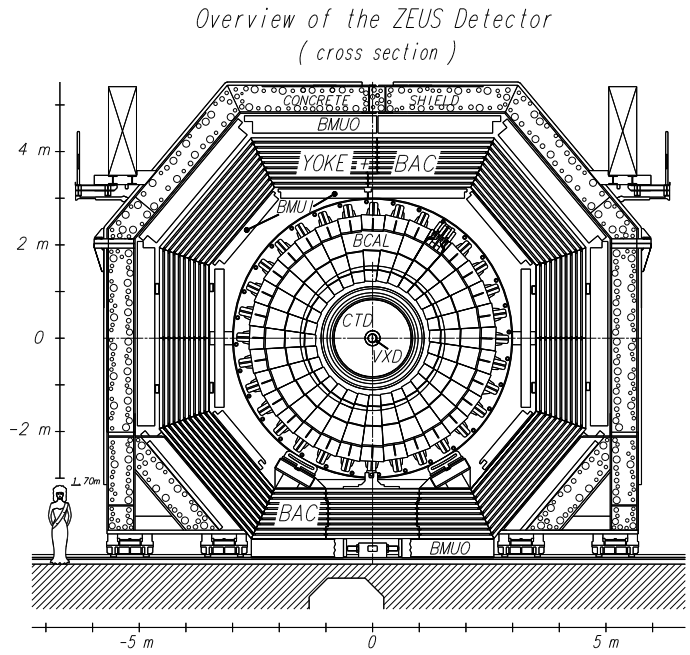

Figure 3.4: *The cross section of the ZEUS detector.*

designed to detect very forward produced neutrons.

Following the electron beam direction, two lead scintillator calorimeters are installed at $z = -35\,\mathrm{m}$ (LUMIe) and $z = -107\,\mathrm{m}$ (LUMIg) from the interaction point. They are part of the luminosity monitor (LUMI) and were designed to measure the small angles of outgoing electrons and photons from the bremsstrahlung process $ep \to ep\gamma$ used in the luminosity measurement. LUMIe and LUMIg detectors are also used to tag electrons from photoproduction events with $Q^2 \approx 0\,\mathrm{GeV}^2$ and to investigate radiative events. At $z = -8\,\mathrm{m}$ and $z = -44\,\mathrm{m}$ tungsten scintillator calorimeters (TAGGERS) were added to extend the acceptance of the positron tagging.

3.2.1 The Central Tracking Detector

The Central Tracking Detector (CTD) [55] measures the direction of tracks left by charged particles and makes their momenta reconstruction possible. It also allows to estimate the energy loss dE/dx which is used for particle identification.

The CTD is a cylindrical drift chamber located around the beam pipe in the centre of the ZEUS detector. It is 214 cm long with inner radius of 16.2 cm and outer radius of 85 cm. It covers polar angle range of $15° < \theta < 164°$. The CTD is made up of 72 radial layers grouped into 9 superlayers (see Fig. 3.5). The odd superlayers have wires

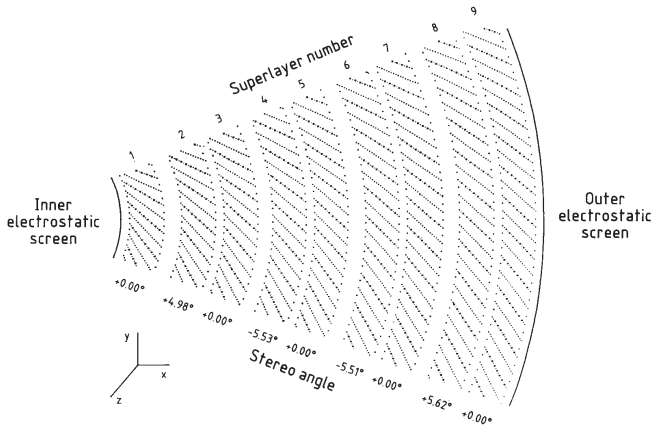

Figure 3.5: *Layout of the CTD octant. The superlayers are numbered and the stereo angles of their sense wires are indicated.*

parallel to the beam axis while the even superlayers have stereo wires tilted by a small angle ($\approx \pm 5°$) which allows to determine the z-position of the hits. The chamber is filled with mixture of Ar, CO_2, and C_2H_6, and operates in a magnetic field of 1.43 T which is produced by a thin superconducting solenoid. Additional information on the z-position of hits is obtained from the precise timing of the charge signals measured in both ends of sense wires in superlayers 1, 3, and 5 (z-by-timing system) [56].

Well reconstructed tracks, crossing at least three superlayers, can be extrapolated to the calorimeter face with small uncertainty. The transverse momentum resolution for tracks crossing all the superlayers is

$$\frac{\sigma(p_t)}{p_t} = 0.0058 p_t \oplus 0.0065 \oplus 0.0014/p_t \qquad (3.1)$$

with p_t in GeV and where $\oplus$ sign indicates a quadratic sum. The first term in the expression comes from the position resolution, whereas the second and third ones are due to multiple scattering before and inside the CTD respectively. The CTD provides the most accurate measurement of the vertex position—the accuracy of the z coordinate measurement is around 1.5-2 mm for well measured events [57].

3.2.2 The Uranium Calorimeter

The Uranium Calorimeter (CAL) [58] is essential for precise measurements of energies and positions of the particles originating from *ep*-scattering. The energy of a particle is measured through conversion of fraction of the initial energy into a visible signal. Incident particle interact with an inactive material (absorber) of the calorimeter producing secondary particles. This is the so-called *showering process*. Calorimeter can measure energies of both charged and neutral particles. The differences between the electromagnetic and hadronic showers are used to identify the scattered electron.

The CAL is a sampling calorimeter consisting of alternating layers of depleted uranium as absorber and plastic scintillator (SCSN-38 polystyrene) as active material for readout purposes. The thickness of the plates (2.6 mm scintillator and 3.3 mm = 1 X_0 uranium) was been chosen such that the calorimeter response to electrons and hadrons is equal ($e/h = 1 \pm 0.02$) over a wide range of energies. This characteristic is important particularly for energy resolution of hadrons as hadronic showers have a statistically fluctuating electromagnetic component. The energy resolution of the ZEUS calorimeter measured under test beam conditions is

$$\begin{aligned} \frac{\sigma(E)}{E} &= \frac{18\%}{\sqrt{E}} \oplus 1\% \quad \text{for electrons,} \\ \frac{\sigma(E)}{E} &= \frac{35\%}{\sqrt{E}} \oplus 2\% \quad \text{for hadrons,} \end{aligned} \tag{3.2}$$

where energy is in GeV and $\oplus$ means summation in quadrature.

The CAL is divided into three parts: the Forward (FCAL), the Barrel (BCAL) and the Rear (RCAL) (see Fig. 3.3) with the angular coverage shown in Table 3.2. The depth of the calorimeter is determined by the maximum jet energy it needs to absorb, requiring 99% energy containment. This energy is a function of polar angle, ranging from about 800 GeV in the forward direction, to about 30 GeV in the rear. The containment of very energetic jets is achieved by surrounding the CAL by a much cheaper iron Backing Calorimeter (BAC).

The calorimeter is vertically (FCAL and RCAL) and radially (BCAL) subdivided into modules (Fig. 3.6), which themselves are subdivided into towers of approximate transverse dimensions of $20 \times 20\,\mathrm{cm}^2$. Each tower is longitudinally segmented into an electromagnetic (EMC) and two (RCAL only one) hadronic sections (HAC1, HAC2; RCAL: HAC). The

Table 3.2: *Angular acceptance and longitudinal depth of the CAL modules.*

	FCAL	BCAL	RCAL
η range	3.95–1.01	1.1–(−0.74)	(−0.72)–(−3.49)
θ range	2.2°–39.9°	36.7°–129.1°	128.1°–176.5°
EMC rad. length X_0	25.9	24.6	24.3
total abs. length λ	7	5	4

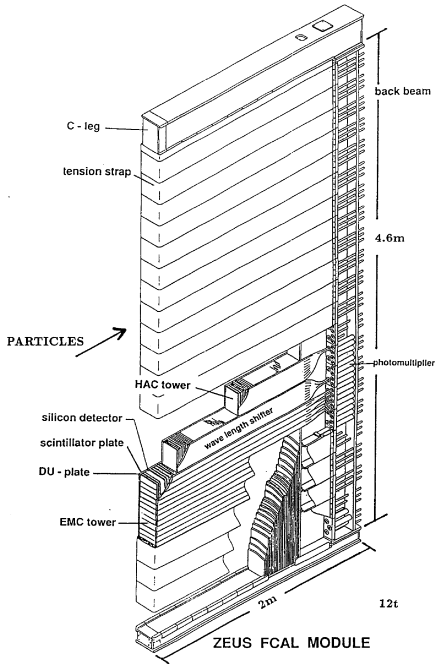

Figure 3.6: *A schematic picture of the FCAL module.*

EMC sections of each tower consists of four $5 \times 20\,\mathrm{cm}^2$ (RCAL: two $10 \times 20\,\mathrm{cm}^2$) cells, whereas the HAC sections consist of one cell only. The BCAL is projective in azimuthal

angle and the EMC sections also in polar angle (see Fig. 3.7). FCAL and RCAL however

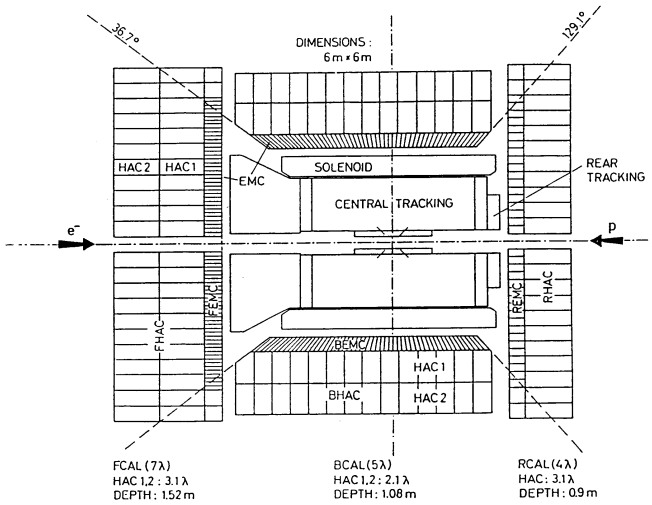

Figure 3.7: *The view of the CAL geometry. The different EMC and HAC sections are shown.*

are not projective. Each cell of the calorimeter is read out on two sides by wavelength shifters which are coupled to the photomultiplier tubes (PMT). The energy corresponds to the sum of both PMTs and is therefore independent of the impact point of the incident particle in the cell. A comparison of energies from both PMTs allows to determine a horizontal impact position. Very precise timing information, with a resolution of less then 1 ns for energy deposits greater than 4.5 GeV, allows to reduce the beam and cosmic background at the trigger level.

The natural radioactivity of ^{238}U provides a stable reference signal for a channel-by-channel calibration to less than 1% precision. The PMTs and the readout electronics are additionally calibrated using LED, LASER, and test pulses.

3.2.3 The Forward Plug Calorimeter

In 1998 a Forward Plug Calorimeter (FPC) [59] was installed into the FCAL beam hole. The FPC was built as a lead-scintillator sandwich calorimeter read out by wavelength shifter fibres and photomultipliers. A front view of the FPC is shown in Fig. 3.8. The active part of the FPC has outer dimensions of $192 \times 192 \times 1080\,\mathrm{mm}^3$. The 63 mm diameter

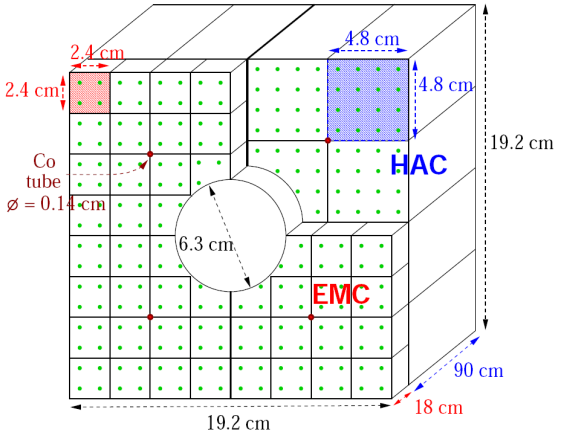

Figure 3.8: *Front view of the FPC.*

central hole accommodates the new reduced HERA beam pipe. The FPC is mechanically divided into two identical half modules. They are attached to the bottom and top half parts of the innermost FCAL module. In the FPC a 15 mm thick lead plates alternate with 2.6 mm thick scintillator layers.

The FPC is longitudinally subdivided into an electromagnetic (EMC) and a hadronic (HAC) sections which are read out separately. The EMC section consists of 10 layers of lead and scintillator corresponding to $26.5\,X_0$ and $0.9\,\lambda$. The HAC section consists of 50 layers resulting in $5.4\,\lambda$ for the complete FPC. With the chosen structure the radiation length $X_0 = 0.68\,\mathrm{cm}$ and nuclear absorption length $\lambda = 20\,\mathrm{cm}$ are similar to those of the FCAL[1]. It also results with an e/h ratio close to unity.

The FPC extends the calorimetric coverage in pseudorapidity from 4.0 to 5.0 which translates also to an increase in accessible mass of the diffractive system M_X by a factor of 1.7.

3.2.4 The luminosity measurement

Each cross section measurement strongly rely on information about the time integrated luminosity $\mathcal{L} = \int Ldt$. Precision of the cross section for certain reaction is directly affected

[1] $X_0 = 0.74\,\mathrm{cm}$, $\lambda = 21.0\,\mathrm{cm}$

by the accuracy of the integrated luminosity according to

$$\sigma = \frac{N}{\mathcal{L}}. \tag{3.3}$$

In the ZEUS experiment luminosity measurement is based on Bethe-Heitler process [60] (*bremsstrahlung*, $ep \to e\gamma p$), where the incoming electron radiates a high energy photon in the electromagnetic field of the proton. The cross section for this process is well known within the confines of QED. It was calculated with an accuracy of $< 0.5\%$.

The ZEUS luminosity monitor (LUMI) [61] consists of two parts, the electron calorimeters (LUMI-e) and the photon calorimeter (LUMI-γ) (see Fig. 3.9). The electron detectors

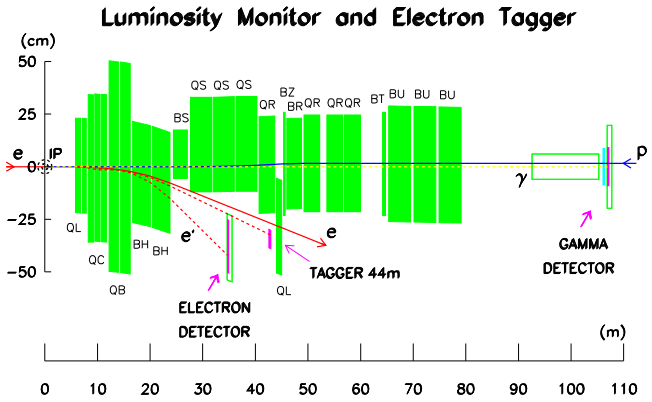

Figure 3.9: *The LUMI system—location of the LUMI-e and LUMI-γ components.*

are located at $z = -8\,\text{m}$, $-35\,\text{m}$, and $-44\,\text{m}$ on the inside of the HERA ring. The detectors placed at $z = -8\,\text{m}$ and $-44\,\text{m}$ are small tungsten-scintillator sampling calorimeters whereas the detector located at $z = -35\,\text{m}$ is a lead-scintillator calorimeter. They detect electrons that lost part of their energy via bremsstrahlung and are deflected from the nominal beam orbit by the magnetic field of HERA. The LUMI-γ lead-scintillator calorimeter is situated at $z = -107\,\text{m}$ and is protected against synchrotron radiation by a carbon-lead filter with a thickness adjustable between 0.5 and 3.5 X_0. This filter reduces the energy resolution to $23\%/\sqrt{E}$. The x and y scintillator strips provide a measurement of the transverse position of the shower which is obtained with a resolution of about 3 mm corresponding to an uncertainty of $\sim 30\,\mu$rad on the photon angle.

Initially the luminosity was measured via coincidence of a high energy photon and a scattered electron. However since 1992, due to sufficiently good background conditions

and due to well controlled photon acceptance, the luminosity calculations are based only on photon detector. The electron calorimeters are used for systematic checks and for tagging of photoproduction events.

There are several background processes that must be taken into account in luminosity measurement. The most important contribution comes from the electron beam-gas bremsstrahlung $eZ \to e\gamma Z$ and it is statistically subtracted using the electron pilot bunches. Also the synchrotron radiation from the electron beam can overestimate the photon rate in the photon detector and therefore it must be corrected offline. Taking into account these and other factors (like photon acceptance determination, energy scale errors) the uncertainty of the integrated luminosity measurement for the years 1999-2000 amounted to 2.25%.

3.2.5 The trigger and data acquisition system

The short bunch crossing time at HERA of 96 ns, which is equivalent to an event rate of $\sim 10.5\,\text{MHz}$, constitute a difficult task for the triggering and data acquisition system [62]. Since the writing speed is limited to a $\sim 0.5\,\text{MB/s}$ the output data rate has to be reduced to an acceptable level. Another reason for decreasing the size of the output is the fact that only a small part of events seen by the detector is of interest to us. Interactions between protons (or electrons) and residual gas molecules, as well as cosmic rays, make the unwanted background which rate amounts to 10-100 kHz. In ZEUS experiment a three level trigger system [63] was designed to fulfil this demanding task (Fig. 3.10).

The First Level Trigger (FLT) is a hardware trigger, designed to reduce the input rate below 1 kHz. Each detector component has its own FLT which stores the data in a pipelines (analog or digital). The decisions from the local FLTs are passed to the Global First Level Trigger (GFLT) which basing on quantities such as energy sums, thresholds, or timing information decides whether to accept or reject the event. This decision is made exactly 46 beam crossings (4.4 µs) after the event took place.

The accepted events are received by the Second Level Trigger (SLT) which is software-based and is realized on a network of transputers. Each component can also have its own SLT which passes a trigger decision to the Global Second Level Trigger (GSLT). At this level there is enough time to use the full spatial and energy resolution of the calorimeter and to reconstruct tracks. A better estimate of the vertex position, the number of clusters, and the timing in the calorimeter are available at this stage. The GSLT makes the decision in $\sim 7\,\text{ns}$ and reduces the event rate below 100 Hz.

All events accepted by the SLT are then treated by the event builder (EVB) [64] which combines information from all detector components in a single record of the ADAMO database tables [65] and transfers them to the Third Level Trigger (TLT) [66]. The TLT is a software-based trigger and includes faster and simplified versions of the offline reconstruction code. It is implemented on a farm of Silicon Graphics computers and is designed to reduce the level of rate to a few Hz

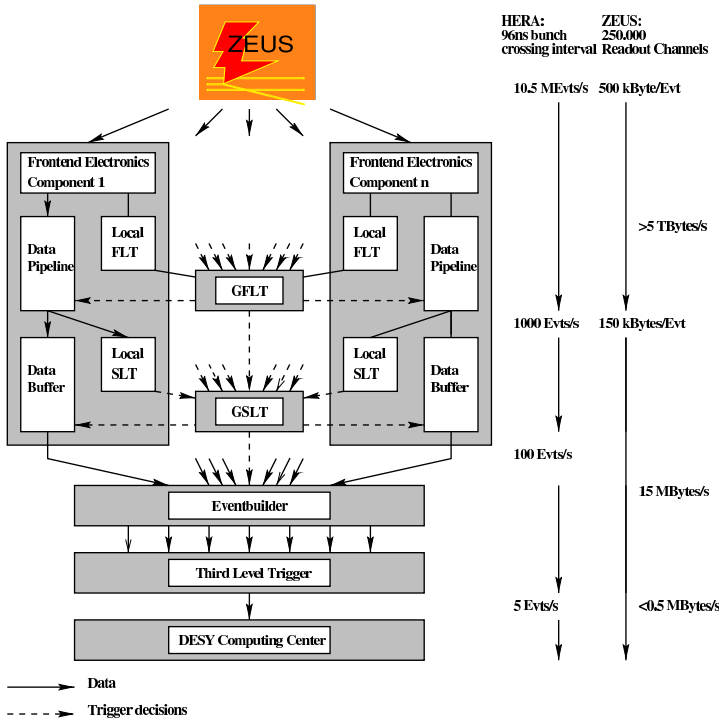

Figure 3.10: *Diagram of the ZEUS three level trigger and data acquisition system.*

Events passing three levels of triggering system are written to magnetic tapes via an optical fibre link (FLINK). From here on events are available for full offline reconstruction and data analysis.

Chapter 4

Event simulation

In order to experimentally verify theoretical predictions for studied processes, a reliable correspondence between the theory and measurement has to be obtained. For this important and complicated problem a numerical simulations based on Monte Carlo techniques are applied. In contemporary high energy physics experiments diverse Monte Carlo programs are used to design the analysis strategy, optimise selection criteria, calculate acceptance corrections, study resolution effects of measured variables, and estimate contributions of background processes.

A Monte Carlo simulation is carried out in two main steps:

1. **Event generation**, where the theoretical knowledge about the analysed process is implemented. It simulates the kinematics and the event topology of the reaction and provides the list of four-momenta of all produced particles.

2. **Simulation of the detector** and trigger system response to the particles generated in the first step. The best understanding of the detector geometry, the passage of particles through matter, and the signal propagation is put in practice here. Section 4.4 includes detailed description of this part.

The output from the Monte Carlo simulation and the data coming from the real detector are prepared according to the same output format. Therefore both data samples can be fed into the same physics analysis program.

Three MC programs were used in present analysis: Satrap [44] for the diffractive events, Djangoh 1.1 [67] for the inclusive DIS events generation, and Pythia [68] for simulation of photoproduction backgorund. The Satrap and Djangoh use Heracles 4.6 [69] to generate the lepton vertex, but the interaction of the photon with constituents of the proton differs in two of them. In both cases the fragmentation is taken care by Ariadne [70], which implements the Colour Dipole Model [71] of fragmentation, or Lepto [72], which implements the Matrix Elements Parton Shower, and Jetset [68] for the modelling of hadronization according to the LUND string model [73]. The general scheme of the Monte Carlo program is depicted in Fig. 4.1.

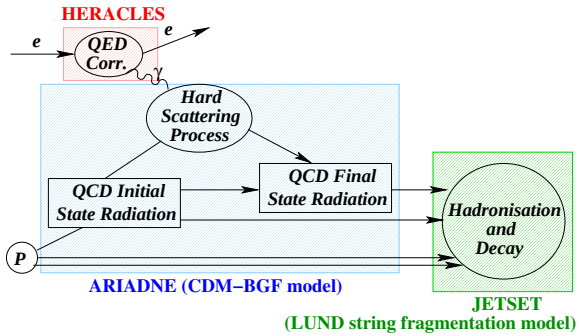

Figure 4.1: *Schematic diagram of an inclusive DIS Monte Carlo generator.*

4.1 Diffractive events simulation—Satrap MC

Interfaced to the RAPGAP 2.08 [74] framework SATRAP Monte Carlo generator is based on the saturation model by Golec-Biernat and Wüsthoff [52] introduced in Sect. 2.2.6. In the saturation model the photon splits into a $q\bar{q}$ pair which is described by the $\gamma q\bar{q}$ wave function. Fluctuations of the incoming photon into a $q\bar{q}g$ state are also taken into account where $\hat{\sigma}_{q\bar{q}} = \hat{\sigma}_{q\bar{q}g}$ is assumed. Using the gluon distribution which is determined by the assumed form of $\hat{\sigma}$, the cross section for the scattering of $q\bar{q}$ and $q\bar{q}g$ states originating from transverse and longitudinal photons was calculated. All free parameters of the model were determined from fits to HERA total DIS cross section data (i.e. $F_2(x, Q^2)$ data) yielding $\sigma_0 = 23\,\text{mb}$, $\lambda = 0.29$, and $x_0 = 0.0003$. For the t dependence of the diffractive cross section the form $d\sigma/dt \propto \exp(Bt)/B$ with $B = 6\,\text{GeV}^{-2}$ is assumed.

4.2 Inclusive DIS events simulation—Djangoh MC

The non-diffractive DIS events ($ep \to eX$) were simulated using DJANGOH 1.1 event generator which is interfaced to HERACLES for electroweak corrections. HERACLES, which was set to use the CTEQ4D [75] parametrisation of the parton distribution functions, includes leading order QED radiative corrections to the Born level cross section (see Fig. 4.2). Radiative corrections coming from the hadron line are smaller than the leptonic ones and are absorbed in the parton distribution functions. QED radiative effects not only change the Born level cross section, but also introduce new types of events since additional photons can emerge. These radiated photons affect the relation between the kinematics at the hadronic vertex and the quantities measured on the electron side.

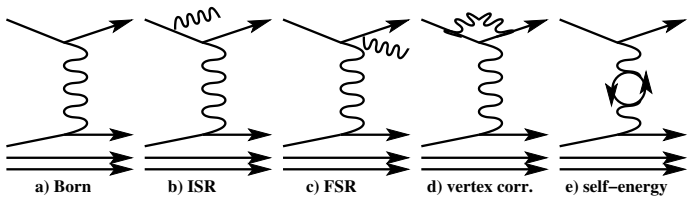

Figure 4.2: *Feynman diagrams of the Born level and the LO QED corrections to NC DIS scattering implemented in* HERACLES.

The QCD cascades are simulated using the Colour Dipole Model (CDM) including boson-gluon fusion as implemented in ARIADNE. In the CDM the colour dipole formed by the struck quark and the proton remnant radiates gluons which in turn can emit softer gluons or split into $q\bar{q}$ pairs. This model provides the best description of the characteristics of the non-diffractive DIS hadronic final state.

In the final step the coloured partons produced in the QCD cascades have to form colourless hadrons. This process is not yet understood from first principles since perturbative calculations are not applicable. Therefore the hadronization has to be described by phenomenological models. In the case of this analysis the LUND string fragmentation model as implemented in the JETSET program is applied.

4.3 Photoproduction events simulation—Pythia MC

Photoproduction (PhP) can represent a serious source of background. It is impossible to reject all PhP events because some of them are indistinguishable from DIS events. It happens when some hadronic activity is wrongly identified as scattered electron while the electron escaped through the beam hole. Therefore the remaining background have to be estimated and then subtracted. The contamination of the data sample was determined using PYTHIA [68] Monte Carlo generator. The sample was generated with $Q^2 < 0.1\,\text{GeV}^2$ and $y > 0.6$.

The PhP Monte Carlo sample consists of several processes with different production mechanisms:

- diffractive PhP processes: $\gamma p \to Vp$, $\gamma p \to Xp$, $\gamma p \to VN$ and $\gamma p \to XN$, where V is one of the light vector mesons ρ, ω or ϕ, and X (N) is the photon (proton) dissociative system,
- soft non-diffractive processes,
- hard (perturbative) PhP which consists of a direct and a resolved photon component.

The relative contribution of each of these subprocesses has been determined from fits to measured quantities. For subprocesses where ZEUS measurements are available (mainly diffractive processes) the measured cross sections have been used to constrain their contributions.

4.4 Simulation of the ZEUS detector and offline reconstruction

The MOZART package [54] is responsible for simulation of the ZEUS detector components. It is based on GEANT 3.13 program [76] which takes care of propagation of the final state particles coming from the event generator. GEANT simulates phenomena that occur when a particle passes through a volume of the detector: energy losses, multiple scatterings, particle decays, etc. Some of the GEANT input parameters were tuned with the help of the test beam data. In the next step data are passed to the ZEUS trigger system simulated by the ZGANA package [77].

Next stage is the offline reconstruction of the raw data coming from the ZEUS detector or its Monte Carlo simulation which is the task of the ZEPHYR package. It includes all calibration and correction factors and provides the higher level data structure (like EFO objects or jets for example). From now on real and Monte Carlo data are treated equally. The complete data flow diagram for both real and Monte Carlo simulated data streams is shown in Fig. 4.3.

4.5 Monte Carlo event samples

A summary of the Monte Carlo samples used in the analysis is given in Table 4.1.

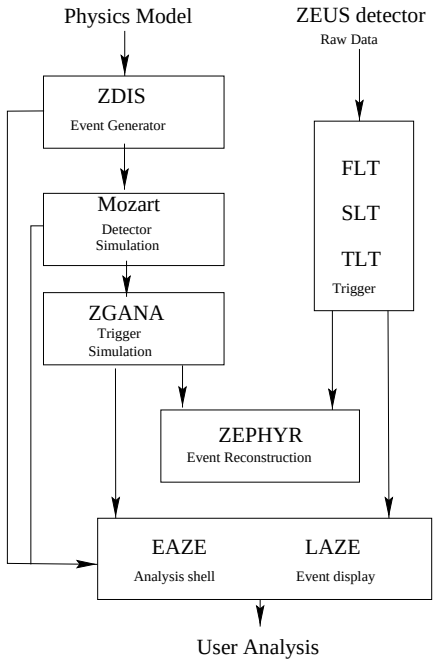

Figure 4.3: *Data flow diagram for the real data and Monte Carlo simulation chain in the ZEUS experiment.*

Table 4.1: *Summary of the Monte Carlo event samples used in the analysis.*

Process	MC set	Q^2 (GeV^2)	σ (nb)	N
Diffraction	SATRAP	$Q^2 > 0.9$	130.1	10999973
$ep \to eXp$		$3 < Q^2 < 20$	44.6	2249981
		$Q^2 > 20$	5.52	999990
		$Q^2 > 80$	0.965	250000
Non-diffraction	DJANGOH	$0.5 < Q^2 < 3$	1839.0	5049770
		$Q^2 > 3$	411.7	7493614
		$Q^2 > 15$	81.4	8036791
Photoproduction	PYTHIA	$0 < Q^2 < 0.1$	1241.0	5493534

Chapter 5

Event reconstruction

5.1 Vertex reconstruction

Measurement of the interaction point is important for the precise reconstruction of the event kinematics and acceptance calculation. The CTD can be used for vertex measurement if there are tracks within its acceptance, either due to the electron (events with high Q^2) or due to the hadronic system (events with medium or high W). The vertex is found by extrapolating the fitted CTD tracks to a common vertex [78]. An accuracy of 2 mm was achieved for this measurement. For events with no tracks within the reach of the CTD, vertex was set to the nominal interaction point.

The distribution of the z component of the vertex in data compared to MC simulation is shown in Fig. 5.1.[1] The plot was made with the diffractive selection described later, in Chapter 6. Achieved agreement is good. In the distribution the central peak with approximately Gaussian shape can be distinguished. The satellite peaks at $z \approx \pm 70$ cm originate from the collisions of particles which accidentally entered a neighbouring bunch.

Distribution of the z component of the vertex in the data should be described reliably by the MC simulation. It is important due to the following reasons:

- The vertex finding efficiency depends on γ_h, but also on the z component of the vertex itself. It can happen that there are no tracks in the CTD and the vertex has to be placed at some fixed value (for example at the nominal vertex), which causes incorrect determination of γ_h and θ_e and consequently—large migrations in the kinematic plane. This is why events without reconstructed vertex should be modelled correctly.

[1] From here on vertical dashed lines in the plots indicate cuts imposed on respective variables.
The SATRAP contribution in the control plots presented in this thesis is scaled up by a factor of 1.21. It originates from the ratio of the LPS to the LRG results and reflects the proton dissociative contribution in analysed data (see Sect. 6.4).

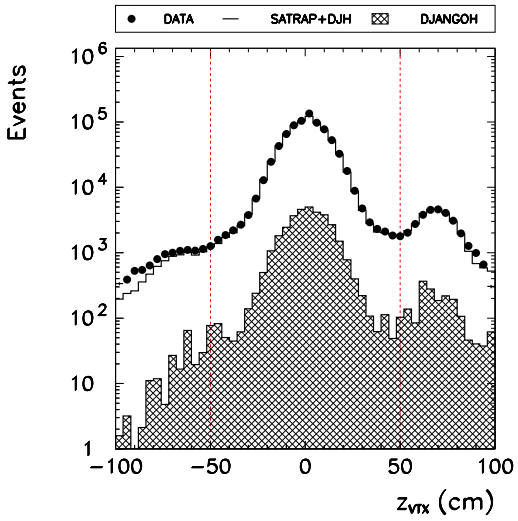

Figure 5.1: *The distribution of the z component of the vertex after the diffractive selection for data and MC.*

- The calorimeter acceptance for the scattered positron depends on the z vertex component, especially at low Q^2.
- Even though the events from the central peak only are selected for the analysis, the agreement in the region of satellite peaks is also important. Such events are, obviously, taken into account in luminosity measurement and potential difference in number of events in the satellite peaks could lead to the normalisation problems.

5.2 Reconstruction of scattered electron

Diffractive events in neutral current DIS were selected by identifying the electron among the final state particles. Scattered electron is characterised by a localised high energy electromagnetic deposit in the calorimeter. Sizes of the resulting electron showers are mostly much smaller than those originating from hadrons. Moreover, as a consequence of energy and momentum conservation, scattered electron transversely balances the hadronic system, which usually results in their good spatial separation. These features make the

electron identification relatively easy.

For scattered electrons identification the SINISTRA95 [79] program was used. It is based on a neural network technique and exploits characteristic features of the electron shower shape induced in the CAL. SINISTRA95 was trained with Monte Carlo events and was optimised for detection of leptons at low and medium Q^2. Identification could be problematic at high Q^2 or at high y where clusters originated from photons produced in the decay of neutral pions can fake the showering of an electron.

In the first step of the electron identification calorimeter cells are grouped into tower islands—objects composed of 3×3 cells in EMC and HAC sections where the central cell is the EMC cell with the highest energy. Each island is then analysed by SINISTRA95 which determines a probability that it corresponds to the scattered electron. Next, the geometric centres of all cells in the identified tower islands are corrected according to the energies measured by the PMTs. After that, the shower dimensions are transformed into a coordinate space in which the calorimeter is projective with respect to the vertex position. The centre of gravity of the shower is calculated and the line joining it with the event vertex is taken as the shower axis.

Measurement of the electron candidate position, when it was found in the RCAL, was improved by the use of HES and SRTD. Since the HES is located at 3.3 X_0 inside the calorimeter, which is close to the maximum of the electron cascade, it ensures a precise electron position determination. From the test beam data it was found that the resolution of the electron position measurement by HES is $\sigma_{x,y} \approx 4.5\,\text{mm}$. In turn, due to the fine segmentation of the SRTD (strips are 1 cm wide), the bias introduced to the electron position measurement by this detector is small. The effective SRTD resolution, after reconstruction procedure, is similar to that obtained with HES: $\sigma_{x,y} \approx 3\,\text{mm}$. Detailed information about the reconstruction using SRTD can be found in [80]. Unfortunately, both HES and SRTD were not able to provide a reliable electron position measurement during the whole data taking period. There was a large number of HES diodes for which the signal could not be measured [81]. Also the efficiency of the SRTD was below 100 % due to problems with the readout which was resulting from dead strips. For that reason a set of conditions was used for the decision which component should be used for the final electron position calculation. The distributions of the x and y coordinates of the scattered electron for data and MC are shown in Fig. 5.2. The electron scattering angle θ_{el} is presented on Fig. 5.3. The data are very well described by the MC simulation.

Energy of the scattered electron was calculated as the sum of energies of all cells associated to the corresponding tower island. The correction for energy loss in inactive material was done with the help of the SRTD and the Presampler which provide information about the size of pre-showering nearby the RCAL. The distribution of the inactive material in front of the BCAL and FCAL is better simulated and more uniform. In this case the energy corrections were obtained from the test beam studies of the calorimeter [82] and from the map of the inactive material basing on the Monte Carlo simulation. Corrections for the dead material were different for real and simulated data due to in-

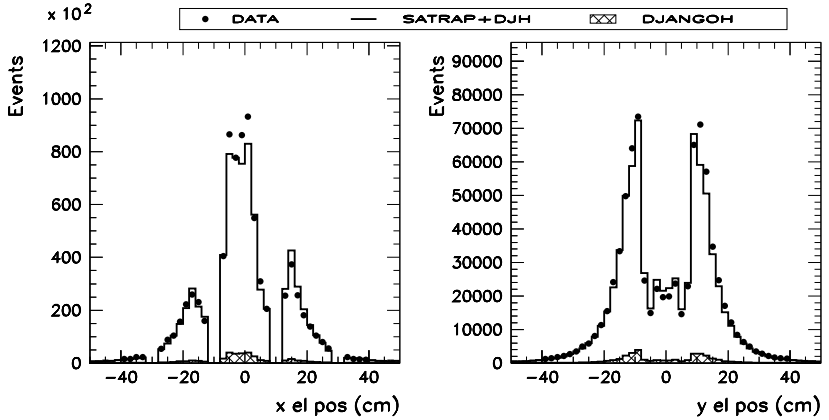

Figure 5.2: *The distributions of the x (left) and y (right) components of the scattered positron after the diffractive selection for data and MC.*

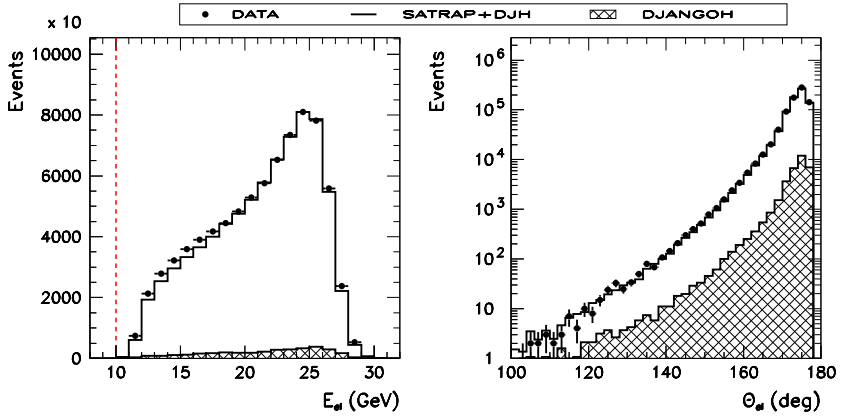

Figure 5.3: *The distributions of the scattered electron energy (left) and polar angle (right) after the diffractive selection for data and MC.*

sufficient description of the inactive parts in the simulated detector. Distributions of the scattered electron energy for data and MC are shown in Fig. 5.3.

Depleted uranium inside the calorimeter, as a radioactive material, creates a certain level of low-energetic noise signal which manifests oneself in the activity of the calorimeter not caused by the *ep* interactions. Energy deposits due to noise signal amount to about 1 GeV for entire CAL. In order to remove this contribution a noise suppression NOISE02S package was applied. It implements a special treatment for cells known to frequently exhibit noise signal and it takes care of cells with bad photomultipliers. The NOISE02S program introduced the following minimum energy requirements for single isolated cells: $E_{EMC} > 120\,\mathrm{MeV}$ and $E_{HAC} > 160\,\mathrm{MeV}$.

It was found that agreement between the data and Monte Carlo in calorimeter energy scale is still far from perfect. It is assumed that inactive material is not modelled reliably by the MC, where some simplifications had to be introduced. To improve the situation, a set of correction factors for different regions of the calorimeter was applied. For the RCAL the correction factors were applied separately to each cell. For the inner RCAL ring they were obtained from the kinematic peak events using the shift of the fitted peak between data and Monte Carlo. For the cells from outer ring the correction factors were determined by comparing the electron energy obtained from the measurement with the electron energy reconstructed from the double angle method. The RCAL electron energy corrections are at the level of 2–3 %. For the BCAL cells a global +5 % scaling was used. The FCAL energy was not corrected.

5.3 Hadronic system reconstruction

The hadronic final state system produced in *ep* interactions consists of neutral as well as charged particles. In order to determine parameters that describe the system, all these particles have to be measured as precisely as possible. Most of them are detected in cells of the uranium calorimeter, whereas only charged ones can be measured by the tracking detectors. Unfortunately, there are several problems that make the reconstruction imperfect.

The effect of the uranium noise was already mentioned in Sect. 5.2. To manage it, MC simulations include the noise parametrisation obtained from the randomly triggered events. Such events are taken during each run and sample the CAL between the *ep* interactions.

Nevertheless, there are other effects like noisy or sparking PMTs that are not simulated in the MC and need to be handled at the reconstruction level. Mini sparks in the data were removed by introducing an energy dependent imbalance cut applied to single isolated cells:

$$|Imb| < 0.7E_{cell} + 0.018\,(\,\mathrm{GeV}), \tag{5.1}$$

where imbalance, $Imb = E_L - E_R$, is the energy difference between left (E_L) and right (E_R)

PMT. The other problem are the so-called hot cells. Such cells fire with much higher frequency than the ones in working order. It happens when one of the PMTs is dead and the other one is faulty. Hot cells are removed by the firing frequency cut imposed on the data only.

Even after mini sparks and hot cells removing there is still around 600 MeV of noise signal per event. This remaining noise contribution is subtracted by removing of single isolated cells with energies below threshold values introduced in the NOISE02S program.

Another problem is also related to a calorimeter reconstruction. All hadronic final state variables were calculated under the assumption that each calorimeter deposit was due to a massless particle. Mass of the hadronic system calculated in this way includes a fake contribution related to the geometric granularity of the calorimeter. The solution of that problem could be the clustering of the calorimeter cells corresponding to a single particle. This procedure will be described later, in Section 5.3.1.

Next experimental problem depends on the construction of the detector itself. There are many components inside, like beam pipe, solenoid coil, screws, cables, which represent the so-called inactive material. Due to pre-showering effect particles may loose some part of their initial energy while crossing such inactive parts. As a result energy deposited in the calorimeter is reduced. Situation improves when, before the hadronic reconstruction, energy scale corrections are applied. The energy calibration factors in the data were determined by studying the p_t balance between the hadronic system and the scattered electron. This was then compared to the same quantity in the simulation, where known effects of dead material had been incorporated. The calibration corrections found for respective parts of the calorimeter are collected in Table 5.1. Independently, part of

Table 5.1: *Calorimeter calibration correction factors.*

	EMC	HAC
FCAL	+4%	−5%
BCAL	+4%	+8%
RCAL	cell-by-cell, +5–+13%	+2.2%

the energy lost in inactive material can be recovered if the tracking information is used together with the calorimeter information—see the next section.

5.3.1 Clustering of calorimeter cells and tracks matching

The particles which reach the ZEUS calorimeter shower and deposit their energy in several adjacent cells. The role of the clustering algorithm is then to merge cells which in an

ideal case belong to the shower of a single particle. Furthermore, some clusters can be matched to the charged tracks and replaced by them since the tracking system often yields a better accuracy for the measured energy of the particles than the calorimeter. This is true especially at low energies of the particles and in situations when a particle has to traverse inactive material. It was found that the combined information from the calorimeter and from the tracking detectors can significantly improve the reconstruction of the hadronic final state [83].

In the first step adjacent cells in EMC, HAC1, and HAC2 sections separately are grouped together into cell islands, see Fig. 5.4. In the second pass the cone island clus-

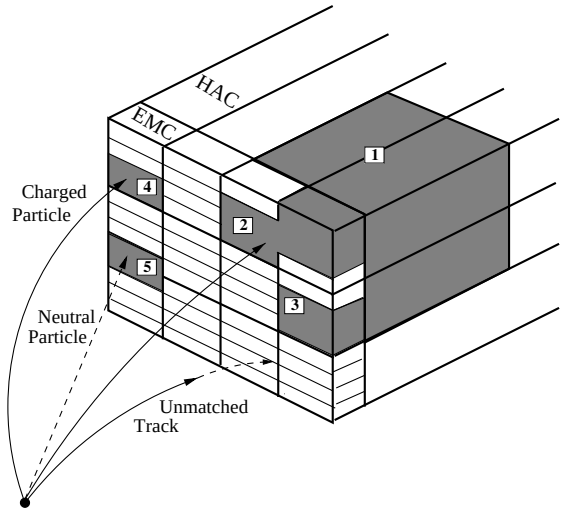

Figure 5.4: *The principle of combining neighbouring calorimeter cells into cell islands. There are four EMC islands and one HAC island in the picture. The matching of CTD tracks to the calorimeter objects is also shown.*

tering in the θ–ϕ space is performed. The resulting cell islands which belong to a shower of a single particle or a jet of particles, are joined into 3-dimensional objects—so-called cone islands, see Fig. 5.5. Position of the shower is estimated as the centre of gravity of the cluster [84]:

$$r = \frac{\sum_i w_i r_i}{\sum_i w_i}, \tag{5.2}$$

where r_i is the geometric centre of a cell i within the cluster. The weights w_i are given

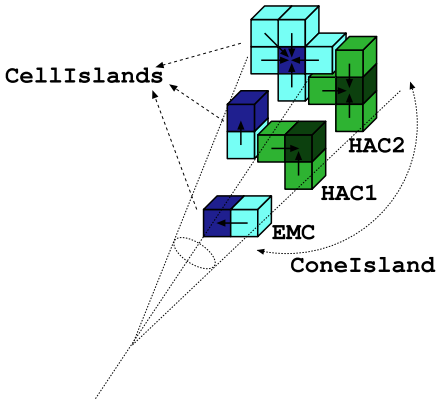

Figure 5.5: *Combining EMC and HAC cell islands into cone islands.*

by the following expressions [85]:

$$w_i^{EMC} = \max\left\{0, W_e + \ln\frac{E_i}{E_T}\right\},$$
$$w_i^{HAC} = \max\left\{0, W_h + \ln\frac{E_i}{E_T}\right\}, \tag{5.3}$$

where E_i is the energy deposited in the i-th cell, E_T is the total energy of the cluster $E_T = \sum_i E_i$, and W_e, W_h are tuned parameters. Contrary to the linear energy weights, the logarithmic ones take into account the exponential fall-off of the shower energy distribution from the shower maximum. Apart from that, if the linear weights were used, they would introduce systematic bias in the reconstructed cone island position due to varying cells projectivity as seen from the vertex. The reason for introducing two separate parameters W_e and W_h is to account for the different sizes of the EMC and HAC cells.

Geometric centre of each cell was corrected in one dimension by the energy imbalance information: $x_i = x_i^0 + \delta x$, where x_i^0 is the geometric centre of a cell and δx is given by:

$$\delta x = \frac{\lambda}{2}\ln\frac{E_R}{E_L}. \tag{5.4}$$

This expression was extracted from the test beam data [86] with $\lambda = 54\,\text{cm}$.

Procedure described above considerably improve cluster position reconstruction as the effect of shower fluctuations damping by the logarithmic weighting. On the other hand the agreement between the data and MC simulation of shower shapes becomes less crucial.

The next stage is the matching of the "good" tracks found by tracking detectors to the cone islands, see Fig. 5.4. A "good" track was this one which satisfied the following conditions:

- traversed at least 4 superlayers of the CTD,
- transverse momentum was in the range of $0.1 < p_t < 20\,\text{GeV}$; for the tracks that passed more than 7 superlayers, the maximum p_t was increased to 25 GeV,
- was fitted to the primary vertex.

Then, the tracks chosen with above criteria were extrapolated to the inner surface of the calorimeter. The good track matches an island if the distance of closest approach between the extrapolated track and the cone island position was less than 20 cm or if the distance of closest approach was less than the maximum radius of the island on the plane perpendicular to a ray drawn from the vertex to the island. The result of this operation are groups of matched tracks and islands. Finally, for each group of associated track(s) and island(s), the decision has to be made which energy flow information should be used. There are several rules depending on track-island configuration:

- good track without any calorimeter island matched—the energy was determined from the track momentum, assuming that it was left by a pion,
- calorimeter objects not associated to any track were counted as a neutral objects and the calorimeter information was used,
- calorimeter objects associated with more than 3 tracks were counted with the calorimeter energy.

The decision to take the tracking instead of the calorimeter information in the 1-to-1 track-island case was based on two requirements. The first one ensured that the energy deposit in the calorimeter was due to the associated track alone. The second requirement assured that the resolution of the track momentum was better than the energy resolution of the island.

There are two major advantages in using combined information from tracking and calorimeter islands. Firstly, a low energy charged particles which do not reach the calorimeter can be measured in the CTD and taken into account in calculation of hadronic variables. Secondly, the energy of hadronic particles that lost a large amount of energy in the inactive material between the CTD and the calorimeter is replaced by the CTD momentum and the energy loss could be avoided in this way.

5.3.2 Hadronic final state variables

The output from the cells clustering and tracks matching procedures is a set of objects known as Energy Flow Objects (EFOs). The total four-momentum for an event was reconstructed according to the following relations:

$$E_{had} = \sum_{i=1}^{\#EFOs} E_i,$$
$$p_{j,had} = \sum_{i=1}^{\#EFOs} p_{ji}, \tag{5.5}$$

where the sums run over all EFOs and $j = x, y, z$. The mass of the hadronic system was calculated from its four-momentum:

$$M^2_{X\,EFO} = E^2_{had} - p^2_{x,had} - p^2_{y,had} - p^2_{z,had}. \tag{5.6}$$

In order to improve agreement between generated and reconstructed diffractive masses, the reconstructed one was multiplied by an additional scaling factor: $M_X = M_{X\,EFO} \cdot 1.12$ in MC and in real data as well. Mass was not rescaled for the events when there were only two EFOs found and both of them had a track matched to it. It was assumed that in such cases these two EFOs correspond to a pair of pions, which are measured reliably. Figure 5.6 shows the distributions of the total energy and momentum of the hadronic final state system in data and in MC that were made using the diffractive selection described in Chapter 6. Distribution of the reconstructed diffractive mass is shown in Fig. 5.7.

Relative difference between the generated value and the measured one was determined from Monte Carlo simulation for the kinematic variables essential for this analysis. The mean value of this quantity is a measure of the systematic shift from generated to measured value. The width of this distribution estimates the resolution of the measured kinematic variable. For example, relative difference between the generated and measured M_X can be written as:

$$\frac{M_{X,rec} - M_{X,gen}}{M_{X,gen}}. \tag{5.7}$$

It is shown in Figure 5.8. Quality of the diffractive mass reconstruction is presented also in Figs. 5.14 and 5.15, where $(M_{X,rec} - M_{X,gen})/M_{X,gen}$ as a function of generated and reconstructed mass are plotted.

5.4 Reconstruction of the kinematic variables

Reconstruction quality strongly depends on precise measurement of the final state system. For diffractive NC DIS process it is composed of the electron, hadronic system, and

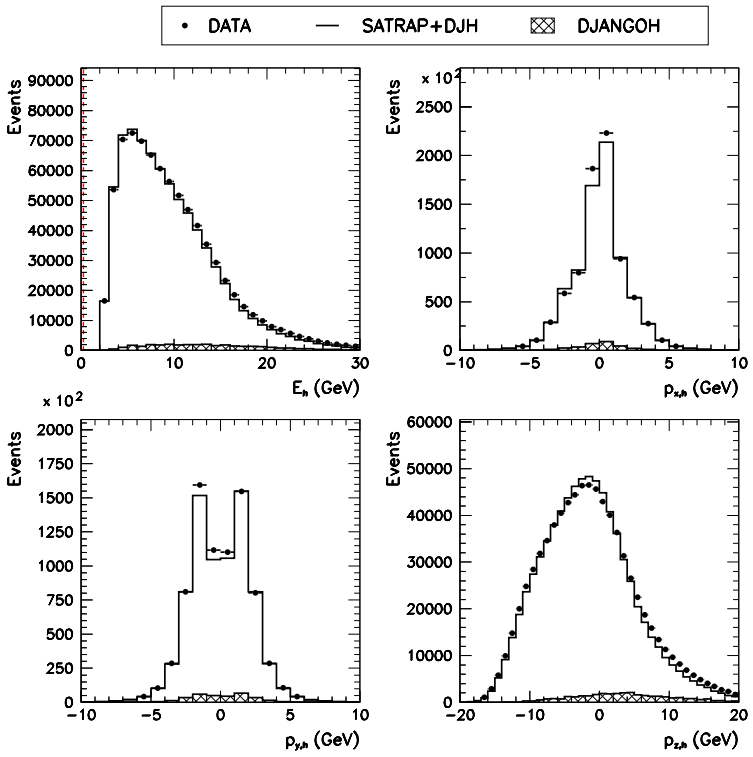

Figure 5.6: *The four-momentum of the hadronic final state system: distributions of the energy (upper left), p_x (upper right), p_y (lower left) and p_z (lower right) after the diffractive selection for data and MC.*

the proton system, which is not detected in present analysis. The fact that parameters describing final state system vary a lot over the phase space (see Fig. 5.9) affects directly the reconstruction quality of the kinematic variables. The need of careful choice of the reconstruction method arises. Figure 5.9 shows the energy and angle of the scattered electron and current jet in the (Q^2, W) kinematic plane.

There are many possibilities of obtaining kinematic variables on the basis of measure-

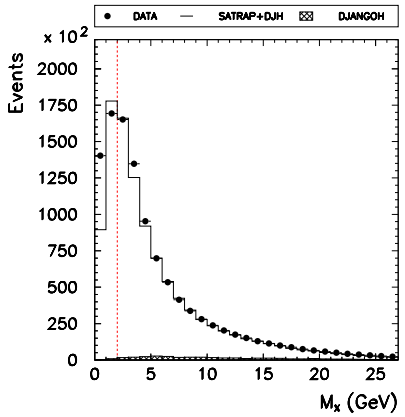

Figure 5.7: *The reconstructed mass of the diffractive system after the diffractive selection for data and MC. Vertical dashed line indicate the cut value.*

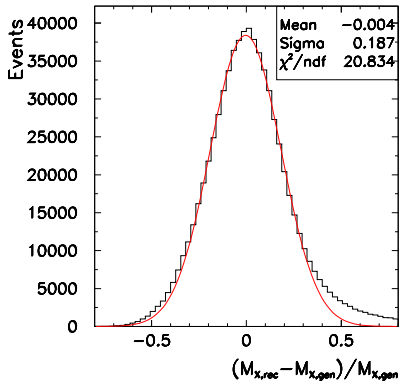

Figure 5.8: *Relative difference between the generated and measured diffractive masses.*

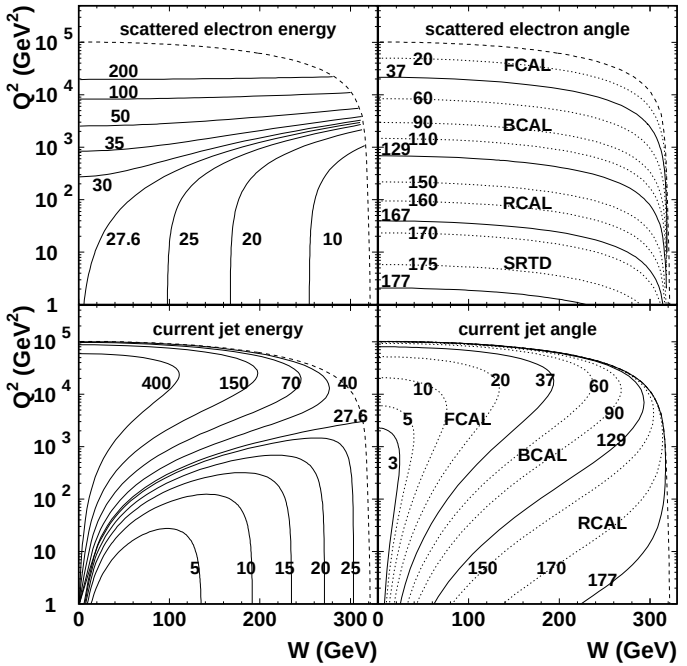

Figure 5.9: *Isolines of the constant energy and polar angle drawn for the scattered electron and current jet in the (Q^2, W) plane. The labels: FCAL, BCAL, RCAL, and SRTD refer to a different parts of the ZEUS detector.*

ment. Usually used are the electron method, Jacquet-Blondel method, double angle, or Σ-method. In some cases, when the analysis covers wide kinematic range, mix of the two methods could be beneficial (e.g. double angle and electron method).

5.4.1 The electron method

This method relies on measurement of the outgoing electron—its energy, E'_e, and polar angle, θ_e. Having such an information one can easily calculate Q^2, x, and y:

$$Q^2 = 2E_e E'_e(1+\cos\theta_e), \tag{5.8}$$

$$y = 1 - \frac{E'_e}{2E_e}(1-\cos\theta_e), \tag{5.9}$$

$$x = \frac{Q^2}{sy}. \tag{5.10}$$

The Q^2 reconstruction with the electron method is precise, however W is poorly reconstructed at low W values since a small error in the measurement of θ_e or E'_e leads to a large migrations in the reconstructed kinematic variables (see Fig. 5.9). In addition this method is affected by QED radiation.

5.4.2 The Jacquet-Blondel method

The kinematic reconstruction method developed by Jacquet and Blondel [87] relies entirely on the hadronic system. It is based on the assumption that the total transverse momentum carried by the hadrons which escape detection through the beam hole in the proton direction, as well as the energy carried by the particles escaping through the beam hole in the electron direction can be neglected. This method is based on the quantities:

$$\delta_{had} = \sum_i^{\#hadrons} E_i(1-\cos\theta_i) = E_{had} - p_{z\,had} \tag{5.11}$$

and

$$\begin{aligned} p^2_{t\,had} &= \left(\sum_i^{\#hadrons} p_{x\,i}\right)^2 + \left(\sum_i^{\#hadrons} p_{y\,i}\right)^2 \\ &= p^2_{x\,had} + p^2_{y\,had}, \end{aligned} \tag{5.12}$$

where the sums run over all final state hadrons. In practice the final-state hadrons are represented by tracks or calorimeter energy deposits.

In the Jacquet-Blondel method the kinematic variables are obtained with the following formulas:

$$y = \frac{\delta_{had}}{2E_e}, \tag{5.13}$$

$$Q^2 = \frac{p^2_{t\,had}}{1-y}, \tag{5.14}$$

$$x = \frac{Q^2}{sy}. \tag{5.15}$$

While the resolution of W at low values is superior to the electron method, the Q^2 reconstruction is poor.

5.4.3 The double angle method

The double angle method of kinematic variables reconstruction takes into account both, the scattered electron and the hadronic final state system [88] and makes use of their polar angles only. The measurement of these angles is often less affected by detector effects and resolution than measurements of energy. This method is to a good approximation independent of the energy scale of the detector. However, it is sensitive to QED radiation.

For the hadronic system, described by the energy E_{had}, the transverse momentum $p_{t\,had}$, and the z-component of momentum $p_{z\,had}$, one can define the γ_h angle:

$$\cos\gamma_h = \frac{p^2_{t\,had} - \delta^2_{had}}{p^2_{t\,had} + \delta^2_{had}}. \tag{5.16}$$

In the naive quark parton model the γ_h angle is interpreted as the polar angle of the struck quark. The kinematic variables are then calculated with the relations:

$$Q^2 = 4E_e^2 \frac{\sin\gamma_h(1+\cos\theta_e)}{\sin\gamma_h + \sin\theta_e - \sin(\theta_e+\gamma_h)}, \tag{5.17}$$

$$y = \frac{\sin\theta_e(1-\cos\gamma_h)}{\sin\gamma_h + \sin\theta_e - \sin(\theta_e+\gamma_h)}, \tag{5.18}$$

$$x = \frac{E_e}{E_p}\frac{\sin\gamma_h + \sin\theta_e + \sin(\theta_e+\gamma_h)}{\sin\gamma_h + \sin\theta_e - \sin(\theta_e+\gamma_h)}. \tag{5.19}$$

5.4.4 Weighted reconstruction method

The variables Q^2 and W were reconstructed using the following combination of the electron and double angle methods (so-called weighted method) [88]:

$$f = \min\left(1,\ \left(\frac{E'_e}{25}\right)^2\right), \tag{5.20}$$

$$\begin{aligned} W_w &= (1-f)\cdot W_{el} + f\cdot W_{DA}, \\ Q^2_w &= (1-f)\cdot Q^2_{el} + f\cdot Q^2_{DA}, \end{aligned} \tag{5.21}$$

where E'_e is given in GeV. This procedure improves the kinematic reconstruction, especially in the regions close to the kinematic space limits. It provides a satisfactory resolution over the entire phase space used in this analysis and therefore was applied here. The electron, double angle, and weighted reconstruction methods are compared in Figs. 5.10 and 5.11. Figures show the profile plots with the relative differences between

the generated and measured values as a function of generated and reconstructed value, respectively for Q^2 and W. The analogous plots, but made in the binnings of Q^2 and W that were used to extract final results, for weighted reconstruction method, are included in Figs. 5.14 and 5.15.

In Fig. 5.12 the $(Q^2_{rec} - Q^2_{gen})/Q^2_{gen}$ and $(W_{rec} - W_{gen})/W_{gen}$ obtained using weighted method are plotted. The kinematic variables x_{IP} and β were calculated according to equations (2.50) and (2.51) where Q^2 and W were reconstructed in the way described above. The quantities of $(x_{\mathrm{IP}\,rec} - x_{\mathrm{IP}\,gen})/x_{\mathrm{IP}\,gen}$ and $(\beta_{rec} - \beta_{gen})/\beta_{gen}$ are shown in Fig. 5.13. Dependences of these parameters on the generated and reconstructed values of x_{IP} and β are presented in Figs. 5.14 and 5.15.

5.5 Comparison of data with MC simulation

Several remaining control plots which were not shown hitherto are presented in this section. In Fig. 5.16 the distributions of Q^2, W (both reconstructed using weighted method), x_{IP}, and β are compared with the result of the Monte Carlo simulation. Next, Fig. 5.17 shows the comparisons for $E - p_z$, η_{max}, and γ_h. Shapes of the distributions show a good agreement. Analysed data are satisfactorily described by the Monte Carlo simulation.

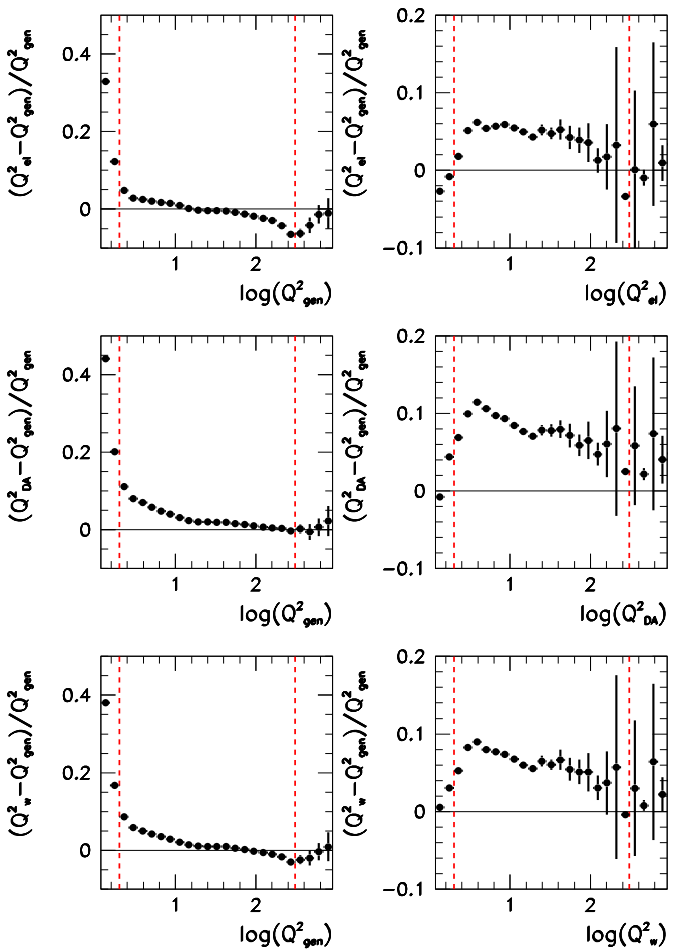

Figure 5.10: *Relative difference between the generated and measured values of Q^2 for the electron, double angle, and weighted reconstruction methods as a function of generated (left plots) and reconstructed Q^2 values (right plots). Vertical dashed lines indicate the cut values.*

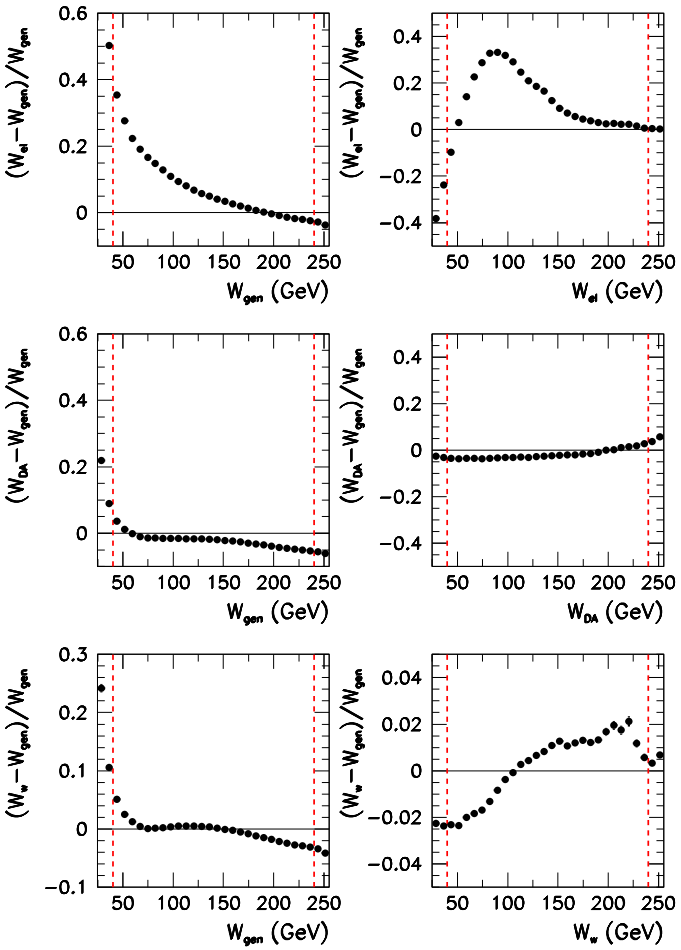

Figure 5.11: *Relative difference between the generated and measured values of W for electron, double angle, and weighted reconstruction methods as a function of generated (left plots) and reconstructed W values (right plots). Vertical dashed lines indicate the cut values.*

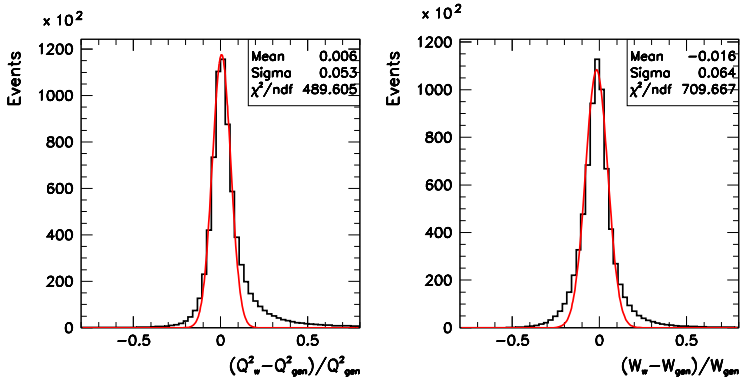

Figure 5.12: *Relative difference between the generated and measured values of Q^2 (left) and W (right) for weighted reconstruction method.*

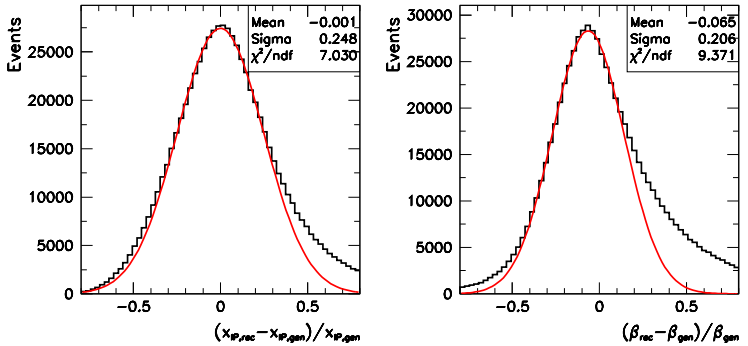

Figure 5.13: *Relative difference between the generated and measured values of x_{IP} (left) and β (right).*

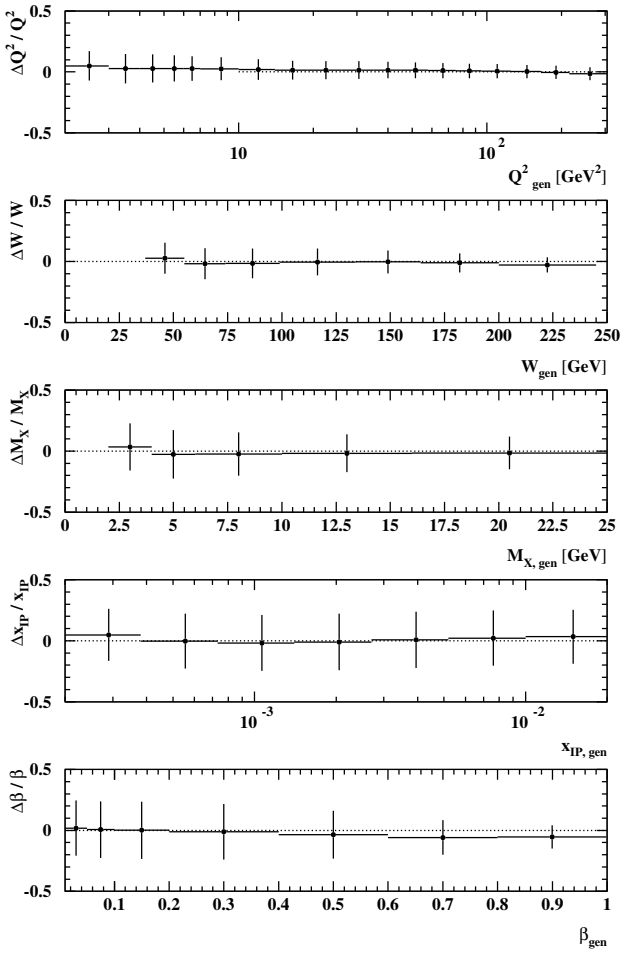

Figure 5.14: *Relative differences between the generated and measured value of Q^2, W, M_X, x_{IP}, and β as a function of generated value of respective variable.*

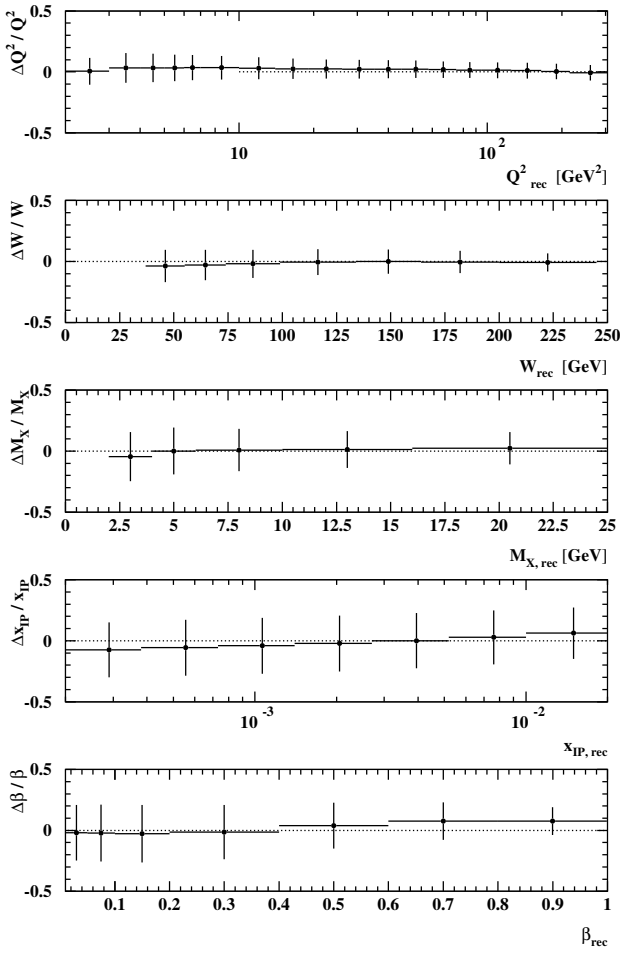

Figure 5.15: *Relative differences between the generated and measured value of Q^2, W, M_X, x_{IP}, and β as a function of reconstructed value of respective variable.*

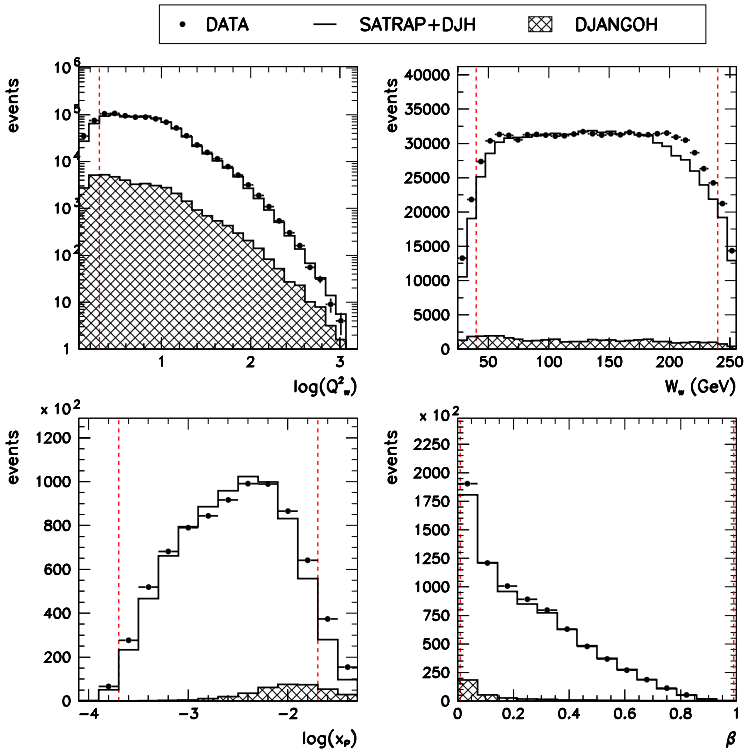

Figure 5.16: *Distributions of the reconstructed Q^2 shown as a $\log Q^2$ (upper left), W (upper right), x_{IP} shown as a $\log x_{\mathrm{IP}}$ (lower left), and β (lower right) after the diffractive selection for data and MC.*

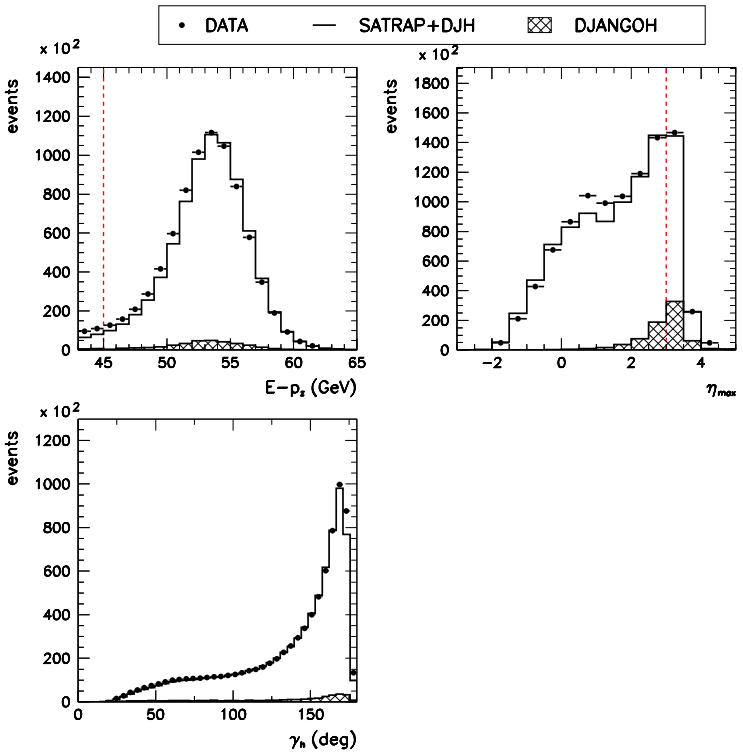

Figure 5.17: *Distributions of the reconstructed $E - p_z$ (upper left), η_{max} (upper right), and γ_h (lower) after the diffractive selection for data and MC.*

Chapter 6

Event selection and background estimation

6.1 Methods of the diffractive contribution selection

Three different methods were used at HERA for the diffractive events selection:

- a reconstructed proton track was required in the Leading Proton Spectrometer (LPS);
- the diffractive events were identified as the excess of events populating the small mass M_X region, in the inclusive $\ln M_X^2$ distribution;
- the hadronic system X measured in the central detector was required to be separated by a large rapidity gap from the rest of the hadronic final state.

In this section all these selection methods are presented.

6.1.1 Use of the Leading Proton Spectrometer

In most of the diffractive events outgoing proton stays intact and provides a clean experimental signature. Since the transverse momentum p_T of the outgoing proton is expected to be small ($< 1\,\mathrm{GeV}$ typically), it escapes through the beam hole in the main detector. Fraction of such events can be detected by the Leading Proton Spectrometer (LPS), a system of silicon microstrip detectors that could be inserted very close to the proton beam. The particle deflections induced by the magnets of the proton beam-line allowed a momentum measurement of the scattered proton. The resulting spectrum of protons measured in the LPS is shown in Fig. 6.1 as a function of $x_L = |p_f|/|p_i|$, where the p_i and p_f are the initial and final proton momenta respectively [89].

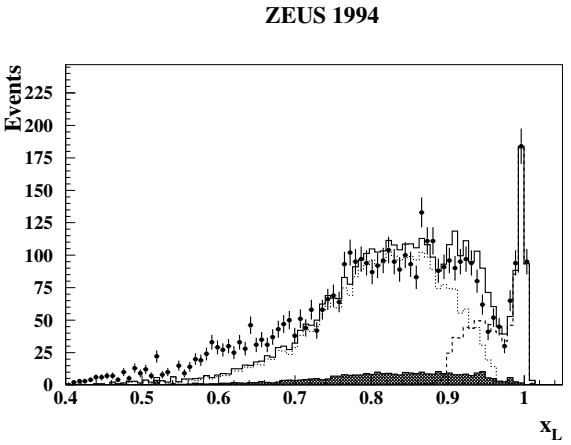

Figure 6.1: *The x_L spectrum measured by LPS. Overlaid (solid line) is the result of fitting this distribution with a sum of contributions from MC generators for double dissociation (shaded area), for pion exchange (dotted line), and for photon diffractive dissociation (dashed line).*

A characteristic peak is observed at $x_L \simeq 1$ which corresponds to photon diffractive dissociation events. A clean sample of diffractive events is obtained by requiring $x_L > 0.97$. The measurement of the momentum vector of the scattered proton allows to determine the t value and to study the t distribution in inclusive diffractive dissociation. However, the drawback of this method is the limited acceptance of the LPS (of the order of 10%), dependent on x_L and p_T of outgoing proton.

6.1.2 Selection of events with a large rapidity gap

Final state particles in the non-diffractive DIS events are distributed uniformly in terms of rapidity $\eta = -\ln\tan(\theta/2)$. Therefore, presence of a large rapidity gap (LRG) $\Delta\eta$ between the system X and outgoing proton (or proton remnant system N) for diffractive interactions can be utilised for extraction of the diffractive sample (see exemplary event display diagram in the Fig. 6.2).

Experimental determination of the rapidity gap rely on calculation of the pseudorapidity of the most forward going particle η_{max}, which deposits some minimum amount of energy (above the noise level) in the detector. Figure 6.3 shows the η_{max} distribution in the DIS sample. A pronounced non-diffractive peak is observed at $\eta_{max} \approx 5$, which

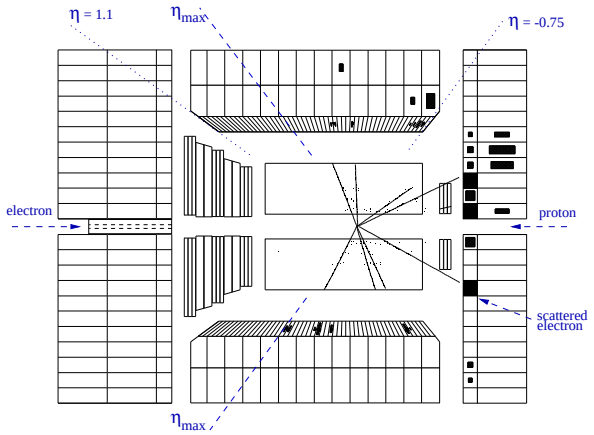

Figure 6.2: *Event display diagram for the diffractive DIS event with a maximum pseudorapidity of $\eta_{max} = 0.6$. There is no activity in the $\eta > \eta_{max}$ region.*

corresponds to the limit of the forward calorimetry. Plateau like structure, due to diffractive events mainly, extends to a low η_{max} (large $\Delta\eta$) values. By setting an upper limit on the maximum pseudorapidity η_{max}, a diffractive sample with relatively low non-diffractive background can be selected. For example, a cut of $\eta_{max} < 3$ corresponds to an effective rapidity gap in the event to be $\Delta\eta \gtrsim 2$.

The large rapidity gap method relies on Monte Carlo simulation and requires a good understanding of the hadronic final state system. Another drawback is the presence of the proton dissociation events, which could be wrongly selected as single photon dissociation events.

6.1.3 The M_X method

The M_X method [7, 90] of the diffractive contribution extraction is based on several properties of the measured invariant mass distribution. Invariant mass M_X is calculated from all the particles in the central detector, excluding the scattered electron. It was observed that $\ln M_X^2$ distribution consists of two components with different behaviour. For non-diffractive events it exhibits exponential fall-off towards low masses (see Fig. 6.4), whereas in the diffractive low mass region, which is mainly populated by the events with large rapidity gap (shaded area on the plot), it evinces a plateau like structure. Another feature of the invariant mass distribution is that the position of the non-diffractive peak

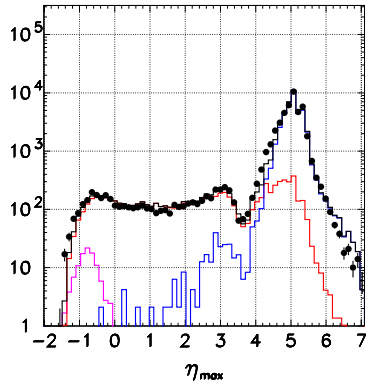

Figure 6.3: *Distribution of the η_{max} for the DIS data (dots) made for $134 < W < 164\ GeV$ and $20 < Q^2 < 40\ GeV^2$. The solid black line represents the sum of the Monte Carlo contributions: non-diffractive (*Djangoh*)—blue line, diffractive (*Satrap*)—red line, diffractive ρ^0 production (*Zeusvm*)—purple line.*

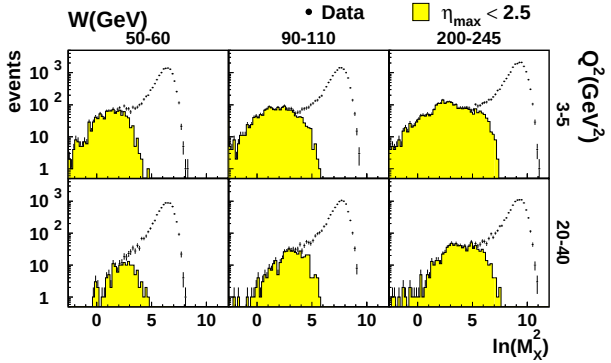

Figure 6.4: *The distribution of $\ln M_X^2$ in several Q^2 and W bins. The shaded areas show the distributions for events with $\eta_{max} < 2.5$.*

scales with $\ln(M_X^2/W^2)$.

In the M_X method the diffractive contribution is identified as the excess of events over the exponential fall-off of the non-diffractive part with decreasing $\ln M_X^2$. The M_X distribution is expected of the form

$$\frac{dN}{d\ln M_X^2} = D + c\exp\left(b\ln M_X^2\right), \tag{6.1}$$

where D denotes the diffractive contribution. Assuming an M_X^{-2} dependence for photon dissociation, expected to hold for $M_X^2 \gg Q^2$ [32, 91], D is a constant. The second term on the RHS represents the non-diffractive contribution. Expression (6.1) is fitted to the measured $\ln M_X^2$ distribution in bins of W and Q^2. The fits are performed to the data in a limited range of M_X, in which the expression (6.1) is expected to hold to a good approximation. It was proven in Monte Carlo study that the b slope values are practically independent on W and Q^2. The same tendency is visible also in the data.

Once the fit parameters for the non-diffractive part are found, it is extrapolated to the low M_X values and then, the diffractive contribution is obtained by statistical subtraction of the non-diffractive component

$$N_{diff} = N - \int_{\ln M_a^2}^{\ln M_b^2} c\exp\left(b\ln M_X^2\right) d\ln M_X^2, \tag{6.2}$$

where N is the observed number of events in considered bin and M_a, M_b are the M_X bin boundaries. The b parameter can be determined either for whole sample globally, or for each W and Q^2 bin separately.

The M_X method allows to extract the diffractive signal without assuming its exact M_X dependence. However, the method is sensitive to the background coming from proton dissociation.

6.2 Trigger selection

The requirements introduced at the First Level Trigger aim at a selection of events with an electron in the calorimeter. In the present analysis they can be summarised as follows:

- **Slot 30** requires at least one isolated electromagnetic cluster in the RCAL; the energy deposits in the RCAL have to satisfy one of the following conditions:
  - energy of the RCAL EMC excluding the first inner ring $> 2032\,\text{MeV}$,
  - energy of the RCAL EMC including the first inner ring $\geq 5000\,\text{MeV}$.

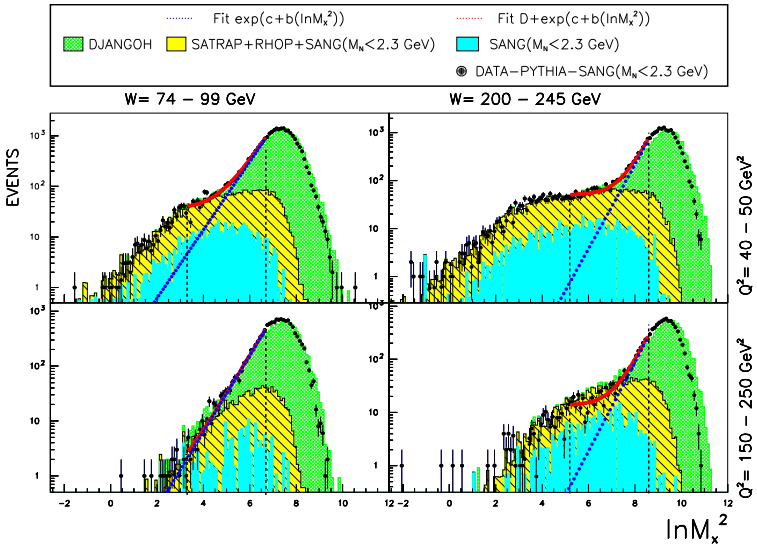

Figure 6.5: *Distributions of* $\ln M_X^2$ *at the detector level for different* (W, Q^2) *bins. The points with error bars show the data. The contributions from non-diffractive (predicted by* DJANGOH *MC) and from diffractive interactions* ($\gamma^* p \to Xp$, $\gamma^* p \to XN$ *for* $M_N < 2.3\,GeV$*; as predicted by* SATRAP, ZEUSVM *and* SANG *MC) are shown. The dash-dotted lines show the non-diffractive contribution as obtained from fitting the data in the* $\ln M_X^2$ *range delimited by the two vertical dashed lines.*

Moreover, the veto conditions on the timing of C5, SRTD, and VETO wall have to be satisfied.

- **Slot 40** requires that the CAL EMC energy is $> 14968\,\text{MeV}$ and the veto conditions on the timing of C5, SRTD, and VETO wall have to be satisfied.
- **Slot 44** requires that the CAL EMC energy has to satisfy one of the following conditions:
  - energy of the BCAL EMC $\geq 4776\,\text{MeV}$ and a track pattern is found by the CTD FLT,
  - energy of the RCAL EMC excluding the first inner ring $> 3404\,\text{MeV}$,

and the same veto conditions as in slot 30 have to be satisfied.

- **Slot 46** requires a minimum energy deposit in the calorimeter or good tracks and vetoes non-ep events.

At the Second Level Trigger the alternative of the DIS6 and SPP11 slots was used. The requirements that are behind it can be summarised as follows:

- minimum energy deposits in either EMC part of the CAL,
- $(E - p_z) - 2E_{LUMI\,\gamma} > 24\,\mathrm{GeV}$, where $(E - p_z)$ is the total $E - p_z$ measured in the CAL using the reconstructed vertex position and $E_{LUMI\,\gamma}$ is the energy in the LUMI calorimeter.

At the Third Level Trigger the DIS06 slot was used for online event selection. The logic of the DIS06 slot during the data taking period used in this analysis was the following:

- $E - p_z > 30\,\mathrm{GeV}$,
- $E'_e > 4\,\mathrm{GeV}$,
- electron box cut: $12 \times 6\,\mathrm{cm}^2$,
- $E_{FPC} < 20\,\mathrm{GeV}$.

6.3 Offline selection cuts

The online trigger selection is rough, because the decision had to be taken quickly and without using any of the corrections, that are available after offline studies. Moreover, the trigger does not select the kinematic space that we are interested in. Therefore the following selection criteria were applied on analysed data sample.

6.3.1 DIS selection cuts

- $|z_{vtx}| \leq 50\,\mathrm{cm}$
  Acceptance depends on the z-component of the reconstructed vertex. When the event occurs far away from the nominal point of interaction, uncertainty of the acceptance could be large. Cut on z_{vtx} reduces this uncertainty.
- $E'_e \geq 10\,\mathrm{GeV}$, $P_{SI} > 0.9$
  Sinistra electron finder, which is based on neutral network technique, was used for reconstruction of scattered electron parameters. Cuts on energy, E'_e, and on probability of electron identification, P_{SI}, were applied to achieve high purity and efficiency of scattered lepton recognition.

- $E_{cone,not\,el} \leq 5\,\mathrm{GeV}$,
  where $E_{cone,not\,el}$ is the energy in the η-ϕ cone of radius 0.8 not associated to the electron. It assures good electron isolation.
- $45 < E - p_z < 65\,\mathrm{GeV}$
  Cuts on the total $E - p_z$, calculated as $E_{had} - p_{z\,had} + E'_e(1 - \cos\theta_e)$, remove majority of the photoproduction and beam-gas events that belongs to the background of present analysis.
- $E_h > 0.25\,\mathrm{GeV}$
  Cut on the total hadronic energy was set above the noise level.
- $y_{JB} \geq 0.002$
  Cut on the variable y_{JB} was imposed in order to limit event migration from the low y region.
- $|p_{t,el} + p_{t,had}| \leq 4\,\mathrm{GeV}$,
  where $p_{t,el}$ is the electron transverse momentum and $p_{t,had}$ is the transverse momentum of the hadronic system. Transverse momentum imbalance cut reduces cosmic event rate in the data sample.

6.3.2 RCAL electron position cuts

Events were required to have at least one electron candidate with a Sinistra95 probability greater than 0.9. In cases when more than one electron candidate was found, the one with the highest probability was selected. In addition, if the candidate was within the region of the CTD acceptance, a track in the CTD was required for such candidate. A track was matched to an electron island if the distance of closest approach from the centre of gravity of the electron shower to the point where the track extrapolated from the vertex intersect the CAL surface was less than 20 cm. If more than one candidate with equal probability was found, the one with highest energy was chosen.

To ensure precise scattered electron measurement, as well as its reliable identification by the electron finder program, the set of cuts on electron position was used. Always when electron hit the RCAL and was found inside certain regions (definitions are undermentioned)—the event was rejected. These unsafe regions are:

- grazing cut: $|x| < 10\,\mathrm{cm}$, $-9.35 < y < 10\,\mathrm{cm}$
  Electrons having such positions could enter into the RCAL from the beam side, behind its front face. They leave energy deposits in the cells adjacent to the beam pipe mostly, what makes the measurement inexact.
- box cut: $13.2 \times 7\,\mathrm{cm}^2$
  Events with electron found in this region are excluded because some part of its shower may be lost in the rear beam hole.

- pipe cut:
  Cooling pipes represents a substantial amount of inactive material which worsens the measurement. They are located at:
  - $\diamond$ $-16 < x < -7\,\text{cm}$, $4 < y < 12\,\text{cm}$
  - $\diamond$ $3 < x < 12\,\text{cm}$, $4 < y < 12\,\text{cm}$
  - $\diamond$ $-16 < x < -7\,\text{cm}$, $-12 < y < -4\,\text{cm}$
  - $\diamond$ $3 < x < 12\,\text{cm}$, $-12 < y < -4\,\text{cm}$
- crack cut
  Crack cut removes the events with electron measured close to the crack between the SRTD segments.
  - $\diamond$ $-13 < x < -8\,\text{cm}$, $-32 < y < 4\,\text{cm}$
  - $\diamond$ $8 < x < 13\,\text{cm}$, $-4 < y < 32\,\text{cm}$
- chimney cut: $-30 < x < 30\,\text{cm}$, $y > 90\,\text{cm}$
  Chimney cut is defined by the part of the RCAL, where the HAC sections are present only.
- intermodule gap cut
  Intermodule gap cut specifies the region with the boundaries between the RCAL modules.
  - $\diamond$ $||x| - 10| < 2.5\,\text{cm}$
  - $\diamond$ $||x| - 30| < 2.5\,\text{cm}$

6.3.3 Kinematic phase space cuts

- The momentum transfer in the electron vertex was restricted to $2 < Q^2 < 2000\,\text{GeV}^2$, but the presented final results were further limited to $Q^2 < 305\,\text{GeV}^2$ by the binning scheme (see Sect. 7.1).
- $40 < W < 240\,\text{GeV}$
  The lower cut on the photon-proton centre-of-mass energy was limited by the resolution which is observed to be poor in the low W region. The highest accessible W values were limited by the cut on minimum energy of the scattered electron ($E'_e \geq 10\,\text{GeV}$).
- $M_X > 2\,\text{GeV}$
  The lower limit on the diffractive mass was set above the ρ resonance region. The final results are presented with the upper cut on the M_X, $M_X < 25\,\text{GeV}$ (see the M_X binning in Sect. 7.1).

- $x_{\text{IP}} < 0.03$
  The upper limit on the proton fractional momentum loss was imposed in order to reduce the contribution of Reggeon exchange. The x_{IP} binning further delimits its range (to $0.0002 < x_{\text{IP}} < 0.02$, see Sect. 7.1).

6.3.4 Diffractive events selection

In the present analysis, the large rapidity gap (LRG) method, described in Section 6.1.2, was used for selection of diffractive events. This method is based on the fact, that in diffractive deep inelastic ep scattering, a large gap in rapidity exists between the hadronic system X and the outgoing proton system.

The upper limitation on η_{max} can provide quite clean diffractive sample. In the analysis this cut was set at:

- $\eta_{max} < 3$,

which corresponds to a rapidity gap ~ 2. Additionally, the upper cut on the energy in the forward plug calorimeter was applied:

- $E_{FPC} < 1\,\text{GeV}$.

It lets through the events with only a little amount of energy, that could be the noise.

6.4 Background discussion

Main part of the background comes from the non-diffractive DIS events. Nevertheless that the $\eta_{max} < 3$ and $E_{FPC} < 1\,\text{GeV}$ cuts were used to reduce it, a non negligible contribution remained in analysed data. This background was studied by means of Djangoh 1.1 MC program (see Section 4.2). The Djangoh sample was generated with the CTEQ4D parton densities parametrisation. The non-diffractive background amounts to about 10% at high x_{IP} and rapidly falls down towards low values of x_{IP}. This contribution (it is shown in Figs. 6.6–6.8) was subtracted from the analysed results.

Estimation of the proton dissociation background ($ep \to eXN$) for LRG analysis is not trivial. First of all the proton dissociation events with $M_N < 2.3\,\text{GeV}$ on average, when all the particles from the N system escape through the forward beam hole or deposit energy less than approximately 1 GeV in the FPC, are indistinguishable from the single dissociative events. Therefore no information could be gained from the data on the contribution from double dissociation process with $M_N \lesssim 2.3\,\text{GeV}$ and consequently it is not possible to adjust the adequate Monte Carlo generator in that region.

In the present analysis the proton dissociation background is significantly suppressed by the $\eta_{max} < 3$ and $E_{FPC} < 1\,\text{GeV}$ cuts. The contribution of proton dissociative events in which the dissociated system escapes undetected in the beam-pipe was estimated from

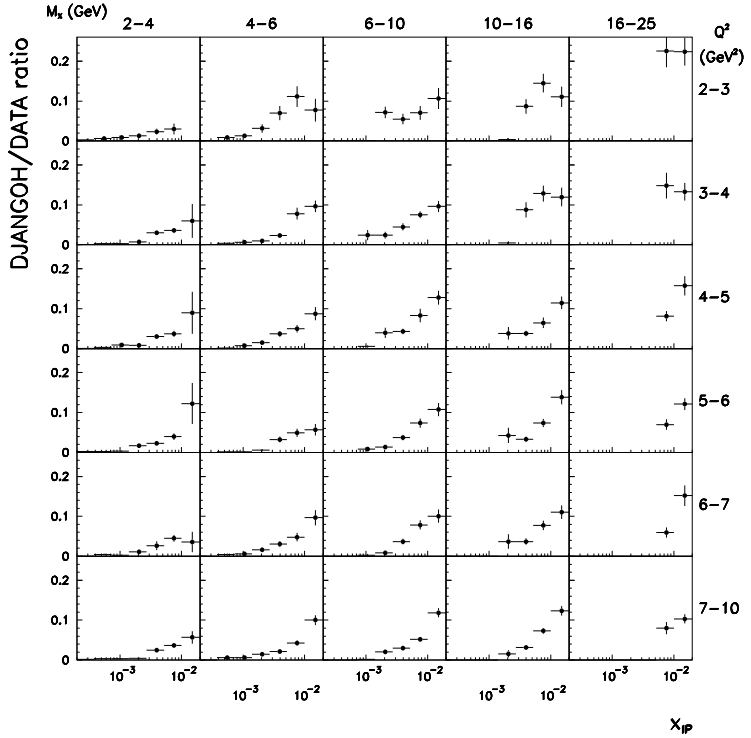

Figure 6.6: *The ratio of number of the non-diffractive events predicted by* Djangoh *to the number of data events after the final event selection. This ratio is shown as a function of x_{IP} in different M_X and Q^2 regions in low Q^2 bins.*

the ratio of the LPS and LRG results, which averages $0.82 \pm 0.01(stat) \pm 0.03(syst)$, independent of Q^2, x_{IP} and β, as discussed in Section 7.4 (Fig. 7.8). The additional uncertainty of 10 % due to unknown normalisation of LPS data is not included. Using the terminology of [92] this implies that the contribution from the proton dissociation in the LRG sample is around ~ 18 %. This background contribution was not subtracted.

The Pythia Monte Carlo generator was used to check the photoproduction back-

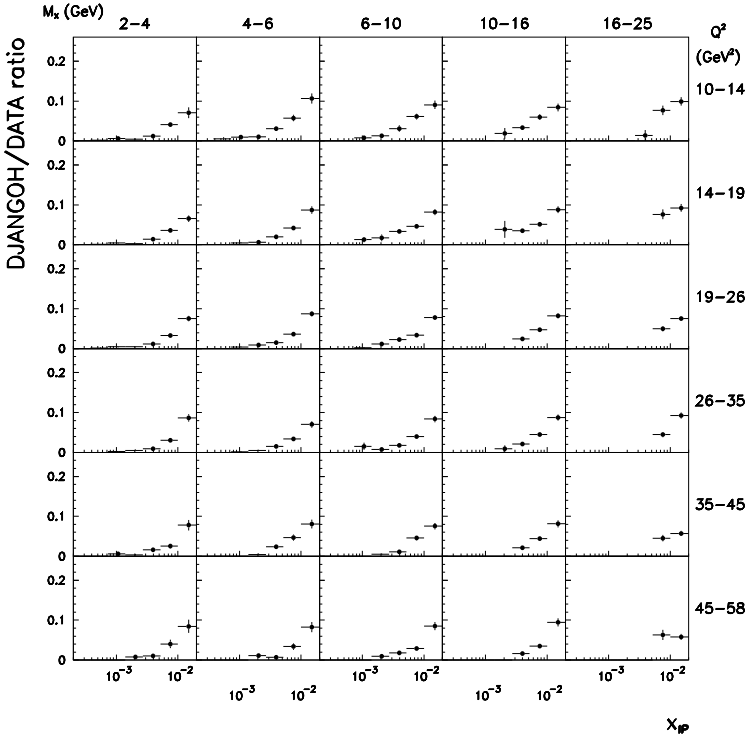

Figure 6.7: *The ratio of number of the non-diffractive events predicted by* Djangoh *to the number of data events after the final event selection. This ratio is shown as a function of x_{IP} in different M_X and Q^2 regions in medium Q^2 bins.*

ground. This kind of background quickly falls with Q^2. The highest contribution of photoproduction was found in the lowest Q^2 bin used in analysis ($2 < Q^2 < 3\,\mathrm{GeV}^2$), where it amounted to approximately 1.2%. Due to so low contamination, this background was neglected in the calculations.

The elastic QED Compton scattering events ($ep \to ep\gamma$) represent another source of background. It may happen that both the electron and the photon are detected in the

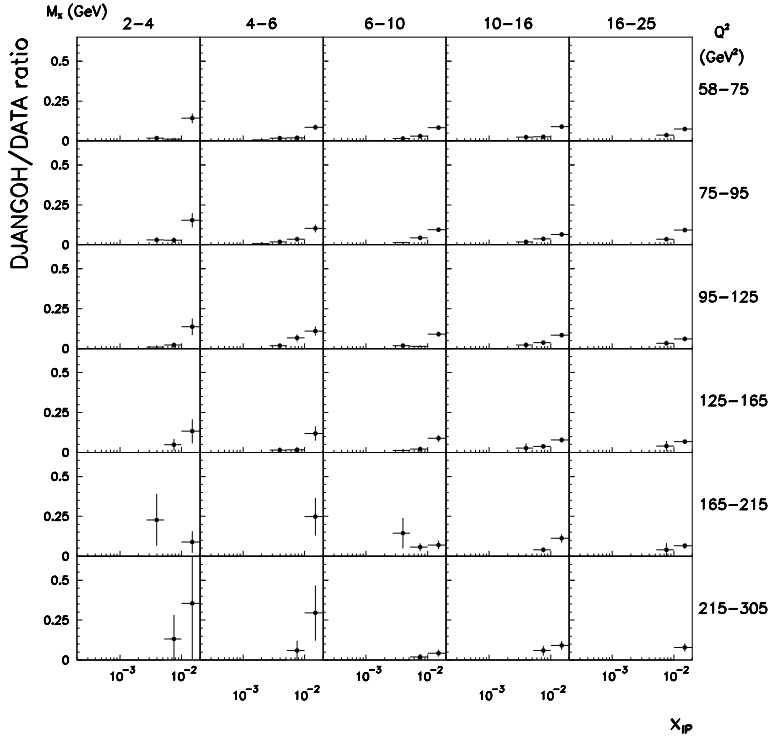

Figure 6.8: *The ratio of number of the non-diffractive events predicted by* DJANGOH *to the number of data events after the final event selection. This ratio is shown as a function of x_{IP} in different M_X and Q^2 regions in high Q^2 bins.*

calorimeter and can fake a DIS event with a low hadronic mass. These events are therefore inconvenient in this analysis. In order to reduce event rate coming from the elastic QED Compton scattering, the following conditions taking into account several features of QED Compton events were used. The event was considered QED Compton (and rejected) if all of the conditions were fulfilled:

- exactly two electron candidates were found with an energy of $\geq 5\,\mathrm{GeV}$,

- there was one, at the most, track fitted to the vertex,
- at least one electron candidate was without a track associated to it,
- the two electron candidates were back-to-back in azimuth plane (exact to a 5°),
- the total energy in the CAL not associated with either of the electron candidates was $< 2\,\mathrm{GeV}$,
- the difference between the polar angles of the two electron candidates was $< 85°$.

Chapter 7

Results

The results of the analysis will be presented as a function of M_X, Q^2, x_{IP} or β. The details of the kinematic variables reconstruction are discussed in Section 5.4. In present analysis the weighted method (described in Section 5.4.4) was used for the reconstruction of Q^2, x_{IP} and β variables.

7.1 Kinematic range and binning

The kinematic region used in the analysis was limited by the detector acceptance, kinematic variable resolution, and the available event statistics. The presented results cover photon virtualities $2 < Q^2 < 305\,\mathrm{GeV}^2$, photon-proton centre-of-mass energies $40 < W < 240\,\mathrm{GeV}$, diffractive masses $2 < M_X < 25\,\mathrm{GeV}$, and proton fractional momentum losses $0.0002 < x_{\mathrm{IP}} < 0.02$. The event selection described in Chapter 6 yielded 792594 events in this kinematic subspace.

The kinematic space was divided into bins in the following way:

- Q^2: 2, 3, 4, 5, 6, 7, 10, 14, 19, 26, 35, 45, 58, 75, 95, 125, 165, 215, 305 GeV^2 (18 bins),
  central values: 2.5, 3.5, 4.5, 5.5, 6.5, 8.5, 12, 16, 22, 30, 40, 50, 65, 85, 110, 140, 185, 255 GeV^2,

- M_X: 2, 4, 6, 10, 16, 25 GeV (5 bins),
  central values: 3, 5, 8, 13, 20 GeV,

- x_{IP}: 0.0002, 0.00038, 0.00073, 0.0014, 0.0027, 0.0052, 0.01, 0.02 (7 bins),
  central values: 0.0003, 0.00054, 0.001, 0.002, 0.0038, 0.0073, 0.014,

- β : 0.01, 0.05, 0.1, 0.2, 0.4, 0.6, 0.8, 0.999 (7 bins),
  central values: 0.025, 0.07, 0.15, 0.3, 0.5, 0.7, 0.9.

The central values specified above are close to the average values of the corresponding bins. The final results are presented at these central values.

7.2 Acceptance corrections

Number of diffractive events obtained after the final data selection and background subtraction have to be corrected for the overall acceptance, which include various experimental factors (like geometrical acceptance of the detectors, trigger efficiency, reconstruction efficiency, limited resolution). In order to determine the "true" distributions (which can be compared with our theoretical predictions) from the measured ones, we often use an unfolding procedure [93, 94]. In the bin-by-bin unfolding method the acceptance correction factor is defined as the number of events which are reconstructed in a given bin and are selected after final selection cuts divided by the number of events which are generated in this bin:

$$A_i = \frac{\#events\ reconstructed\ in\ bin\ i\ and\ selected}{\#events\ generated\ in\ bin\ i}. \tag{7.1}$$

The purity is the ratio of the number of events generated and reconstructed in a given bin to the number of events reconstructed in this bin:

$$P_i = \frac{\#events\ generated\ and\ reconstructed\ in\ bin\ i}{\#events\ reconstructed\ in\ bin\ i}. \tag{7.2}$$

The acceptances and purities calculated with Satrap MC are presented in Figs. 7.1–7.3 in bins of (M_X, Q^2) as a function of x_{IP}.

The reduced diffractive cross section at a given point i was calculated from the ratio of the cross sections in data and MC, multiplied by the reduced diffractive cross section used in the MC generator:

$$x_{\mathrm{IP}}\sigma_r^{D(3),meas}(i) = x_{\mathrm{IP}}\sigma_r^{D(3),MC}(i)\frac{\sigma_i^{data}}{\sigma_i^{MC}}, \tag{7.3}$$

where

$$\frac{\sigma_i^{data}}{\sigma_i^{MC}} = \frac{N_i^{data,rec}/\mathcal{L}_{data}}{N_i^{MC,rec}/\mathcal{L}_{MC}}, \tag{7.4}$$

and i denotes the bin in which value of the reduced diffractive cross section is evaluated. The reduced diffractive cross section $x_{\mathrm{IP}}\sigma_r^{D(3),MC}$, which was used to generate the Satrap MC, corresponds to the QED Born level cross section. The bin centring correction factors were determined by the MC simulation and are included in the $x_{\mathrm{IP}}\sigma_r^{D(3),MC}$.

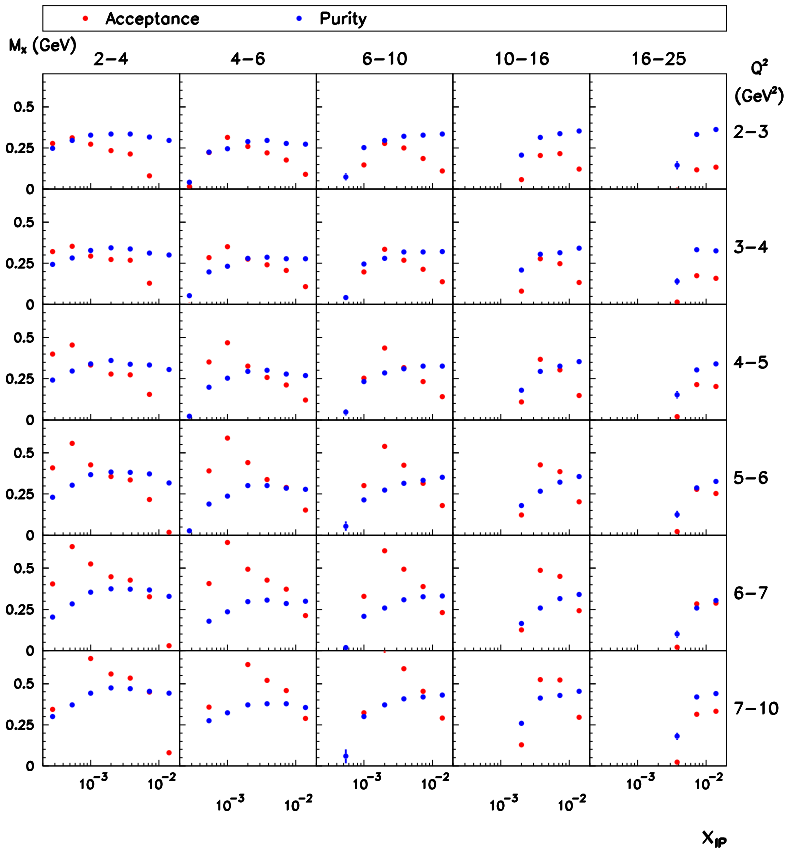

Figure 7.1: *Acceptance corrections (red points) and purity values (blue points) obtained with* SATRAP *MC in bins of* (M_X, Q^2) *as a function of* x_{IP} *in low* Q^2 *bins.*

7.3 Systematic uncertainties

The systematic uncertainties were estimated by varying the cuts and modifying the analysis procedure. The variations of the cuts were typically adequate to the resolutions of the

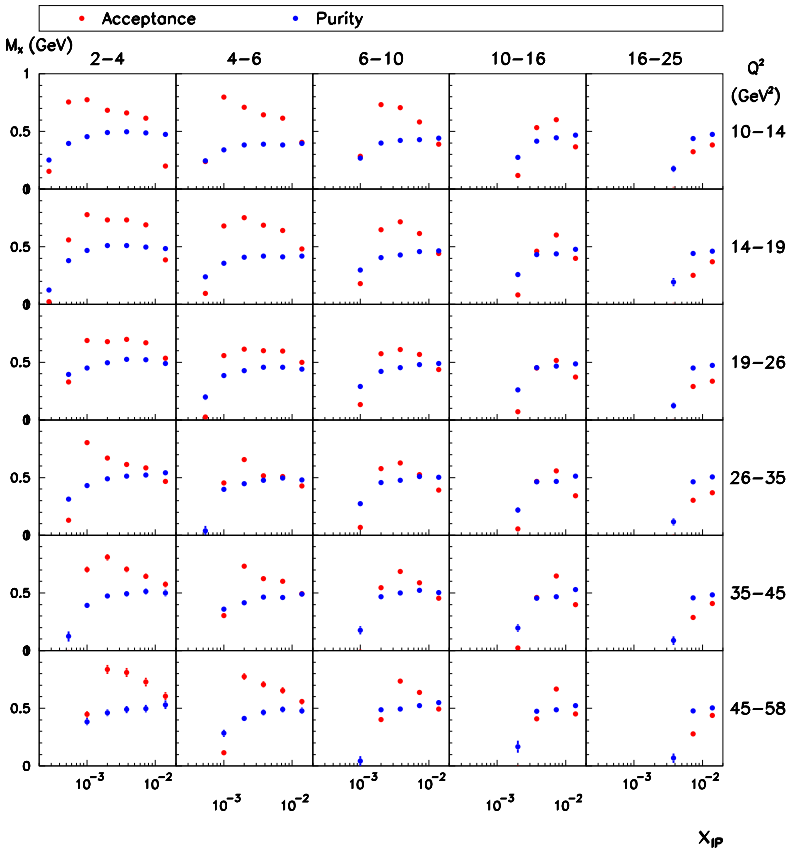

Figure 7.2: *Acceptance corrections (red points) and purity values (blue points) obtained with SATRAP MC in bins of* (M_X, Q^2) *as a function of* x_{IP} *in medium* Q^2 *bins.*

relevant variables. The resulting changes of the reduced diffractive cross section $x_{\mathrm{IP}}\sigma_r^{D(3)}$ were compared to its nominal value. The corresponding average effect of each systematic check in the measured bins is given below, using the notation $(^{+a}_{-b}\%)$. Given systematic check produces an increase of the results in some bins and a decrease in some other bins;

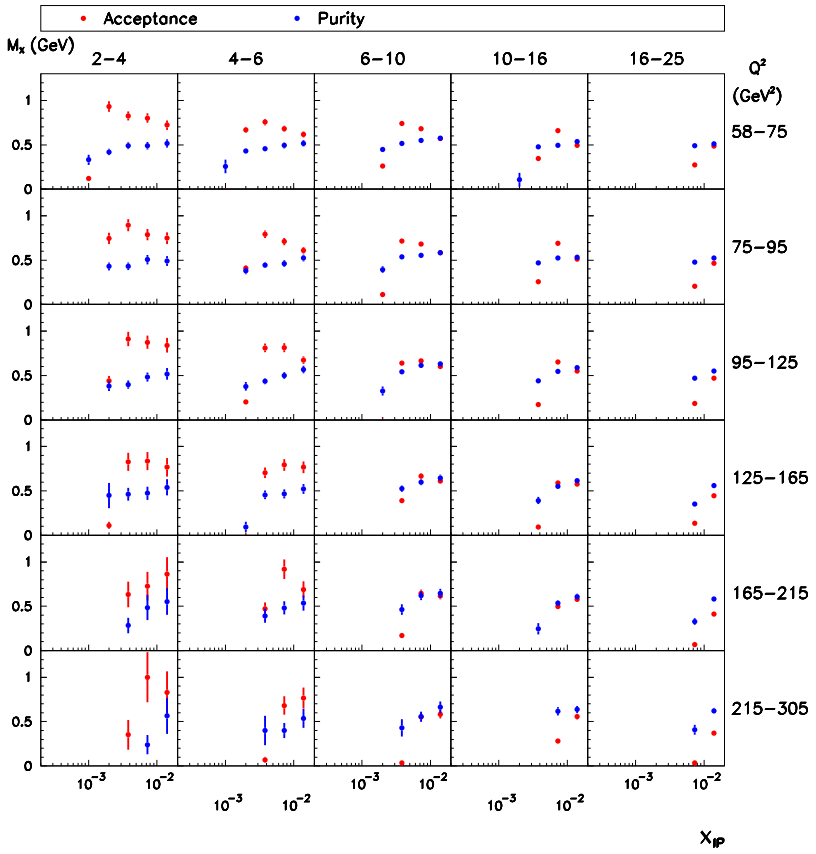

Figure 7.3: *Acceptance corrections (red points) and purity values (blue points) obtained with SATRAP MC in bins of (M_X, Q^2) as a function of x_{IP} in high Q^2 bins.*

the a is the average increase and b is the average decrease of results.

The following checks were performed for both data and MC or for data only (then it will be mentioned explicitly).

1. The cut on the scattered electron energy was increased to 12 GeV ($^{+0.9}_{-0.9}\%$).

2. The fiducial region for the impact position of the electron was enlarged by a 1 cm in each direction ($^{+1.4}_{-0.8}\%$). This cut affects the low-Q^2 data mainly ($Q^2 \lesssim 7\,\mathrm{GeV}^2$).
3. The minimum value of $E - p_z$ was raised from 45 GeV to 47 GeV ($^{+1.3}_{-1.3}\%$).
4. The effect of the energy scale uncertainty of the scattered electron was tested by changing the electron energy in the data by $\pm 2\%$ ($^{+2.7}_{-2.6}\%$). The high-Q^2 data ($Q^2 \gtrsim 95\,\mathrm{GeV}^2$) are affected the most.
5. The energy scale of the CAL for the hadronic system in the data was varied by $\pm 2\%$ ($^{+2.8}_{-2.6}\%$).
6. The z coordinate of the vertex was restricted to $|z_{vtx}| < 40$ cm (originally: $|z_{vtx}| < 50$ cm) ($^{+1.0}_{-1.0}\%$).
7. The standard cut on the $\eta_{\max}$ ($\eta_{\max} < 3$) was changed by a ± 0.3 ($^{+2.6}_{-1.6}\%$). This variation acts on the results measured at high x_{IP} values mostly.
8. The FPC energy cut was lowered from 1 GeV to 0.7 GeV ($^{+0.9}_{-1.0}\%$).
9. The shape of generated x_{IP} distribution in SATRAP MC was reweighted by a factor of $(x_{\mathrm{IP}}/0.01)^k$, with $k = \pm 0.03$ ($^{+3.0}_{-2.9}\%$). Effect of this modification rises with decreasing x_{IP}.
10. The amount of subtracted non-diffractive background was changed by -50% and $+100\%$ ($^{+3.1}_{-5.6}\%$). The most significant changes of results were observed at high x_{IP} and low Q^2 values.

The total systematic uncertainty for each bin was calculated as the quadratic sum of the individual systematic errors, separately for the negative and the positive contributions. The possible correlations between the individual systematic checks were not taken into consideration. The total errors were evaluated as the quadratic sum of the statistical and systematic error. The overall normalisation uncertainty of $\pm 2.25\%$ due to the uncertainty on the integrated luminosity measurement was not included.

7.4 Diffractive reduced cross section $x_{\mathrm{IP}}\sigma_r^{D(3)}$

The cross section for the reaction $ep \to eXp$ can be expressed in terms of the structure function $F_2^{D(4)}$ or the reduced diffractive cross section $x_{\mathrm{IP}}\sigma_r^{D(4)}$, which are defined by the following equations

$$\begin{aligned}\frac{d\sigma^{ep\to eXp}}{d\beta dQ^2 dx_{\mathrm{IP}} dt} &= \frac{4\pi\alpha^2}{\beta Q^4}\left[1 - y + \frac{y^2}{2(1+R^D)}\right] F_2^{D(4)}(\beta, Q^2, x_{\mathrm{IP}}, t) \\ &= \frac{4\pi\alpha^2}{\beta Q^4}\left[1 - y + \frac{y^2}{2}\right] \sigma_r^{D(4)}(\beta, Q^2, x_{\mathrm{IP}}, t). \qquad (7.5)\end{aligned}$$

The quantity

$$R^D = \frac{\sigma_L^{\gamma^* p \to Xp}}{\sigma_T^{\gamma^* p \to Xp}} \tag{7.6}$$

is the ratio of the cross sections for longitudinally and transversely polarised virtual photons. In the region covered by the present data, R^D is expected to be small [95]. The longitudinal structure function F_L^D is related to R^D via $F_L^D = F_2^D R^D/(1+R^D)$.

The reduced diffractive cross section $\sigma_r^{D(3)}(\beta, Q^2, x_{\mathrm{IP}})$ is obtained by integrating $\sigma_r^{D(4)}$ over t:

$$\sigma_r^{D(3)}(\beta, Q^2, x_{\mathrm{IP}}) = \int \sigma_r^{D(4)}(\beta, Q^2, x_{\mathrm{IP}}, t) dt. \tag{7.7}$$

The data are presented in terms of the reduced diffractive cross section $\sigma_r^{D(3)}$. Figures 7.4-7.6 show $x_{\mathrm{IP}}\sigma_r^{D(3)}(\beta, Q^2, x_{\mathrm{IP}})$ as a function of x_{IP} in different β and Q^2 regions.

The quantity $x_{\mathrm{IP}}\sigma_r^{D(3)}$ rises with decreasing x_{IP}. Since the high x_{IP} values are not reached (for the data points on the plots $x_{\mathrm{IP}} \leq 0.014$), no rise of the $x_{\mathrm{IP}}\sigma_r^{D(3)}$ can be seen. The same data are shown as a function of Q^2 for different β and x_{IP} bins in Fig. 7.7. The data are dominated by positive scaling violations. The values of $x_{\mathrm{IP}}\sigma_r^{D(3)}$ exhibit a logarithmic rise with Q^2 up to the high β values (~ 0.7), reminiscent of that of F_2 at low x, suggesting that the diffractive PDFs of the proton are gluon-dominated.

The ratio of the $\sigma_r^{D(3)}$ values obtained with the LPS method to the LRG data is shown in Fig. 7.8 up to the $Q^2 = 40\,\mathrm{GeV}^2$. The ratio is independent of x_{IP} and equal in each β and Q^2 bin with the average value $0.82 \pm 0.01(stat) \pm 0.03(syst)$. The additional 10% normalisation uncertainty of the LPS data is not included. This shows that the $\sigma_r^{D(3)}$ measurements from the LPS and the LRG methods are consistent in terms of the x_{IP}, β and Q^2 dependences. Since the contribution from proton dissociation was subtracted from the LPS data, this normalisation difference is ascribed to the proton dissociative contribution to the LRG data sample.

7.5 Pomeron trajectory

In the framework of Regge phenomenology the x_{IP} dependence of $F_2^{D(4)}$ and $F_2^{D(3)}$ is related to the intercept of the Pomeron trajectory, the parameter that drives the energy dependence of the total hadron-hadron cross section at high energies [96]. The Pomeron intercept was determined to be $1.0964^{+0.0115}_{-0.0091}$ [97] in soft hadronic interactions. However the same parameter is significantly larger in the diffractive production of heavy vector mesons, notably in J/ψ photoproduction (see e.g. [98, 99]), reflecting the rapid rise of the cross section with W. This is a consequence of the increase of the parton densities in the proton at low x, which drives the rise of the cross section with decreasing x, and hence with decreasing x_{IP} (since $x_{\mathrm{IP}} \propto 1/W^2 \propto x$). The slope of the Pomeron

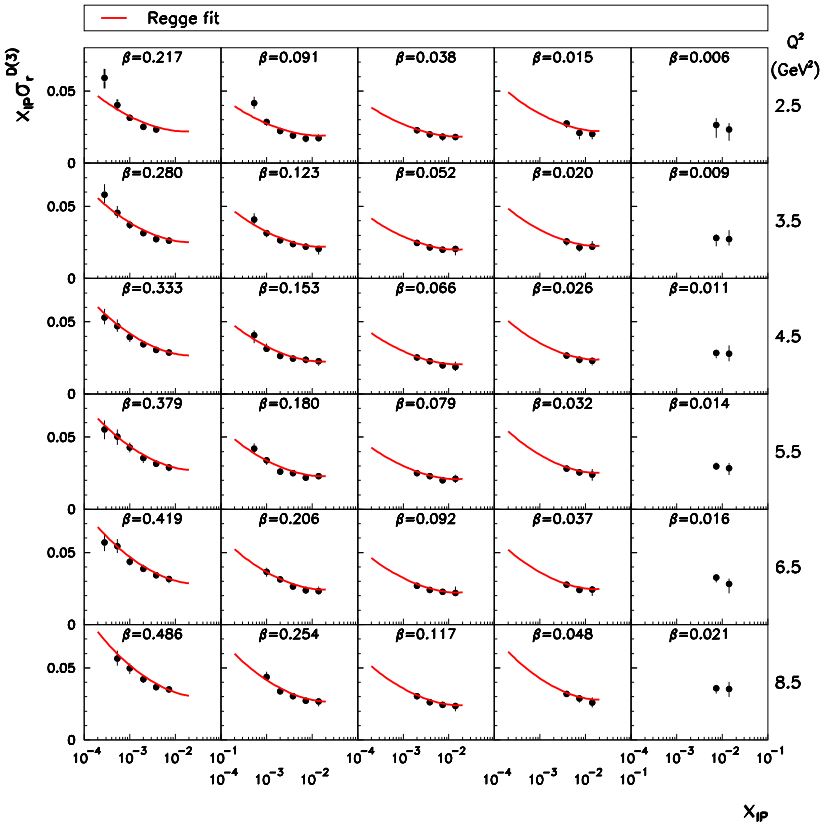

Figure 7.4: *The reduced diffractive cross section multiplied by x_{IP}, $x_{\mathrm{IP}}\sigma_r^{D(3)}$, as a function of x_{IP} in different β and Q^2 regions shown in low Q^2 bins. The inner error bars indicate the statistical uncertainties, the outer bars represent the statistical and systematic uncertainties added in quadrature. The normalisation uncertainty of ±2.25 % is not shown. The continuous lines are the result of the Regge fit described in the text.*

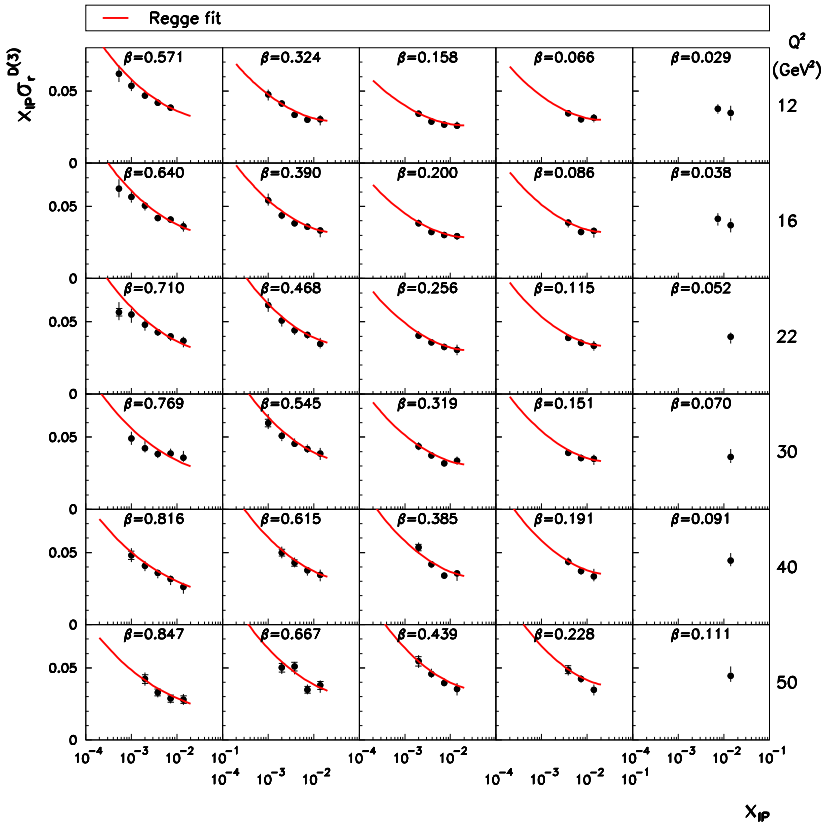

Figure 7.5: *The reduced diffractive cross section multiplied by x_{IP}, $x_{\mathrm{IP}}\sigma_r^{D(3)}$, as a function of x_{IP} in different β and Q^2 regions shown in medium Q^2 bins. The inner error bars indicate the statistical uncertainties, the outer bars represent the statistical and systematic uncertainties added in quadrature. The normalisation uncertainty of $\pm 2.25\,\%$ is not shown. The continuous lines are the result of the Regge fit described in the text.*

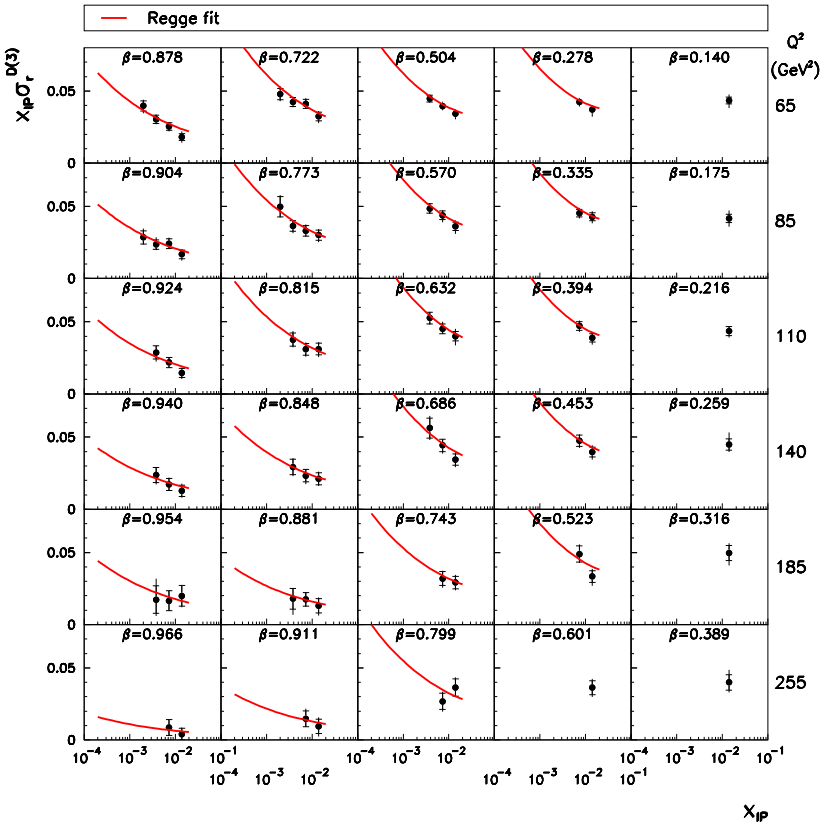

Figure 7.6: *The reduced diffractive cross section multiplied by x_{IP}, $x_{\mathrm{IP}}\sigma_r^{D(3)}$, as a function of x_{IP} in different β and Q^2 regions shown in high Q^2 bins. The inner error bars indicate the statistical uncertainties, the outer bars represent the statistical and systematic uncertainties added in quadrature. The normalisation uncertainty of $\pm 2.25\,\%$ is not shown. The continuous lines are the result of the Regge fit described in the text.*

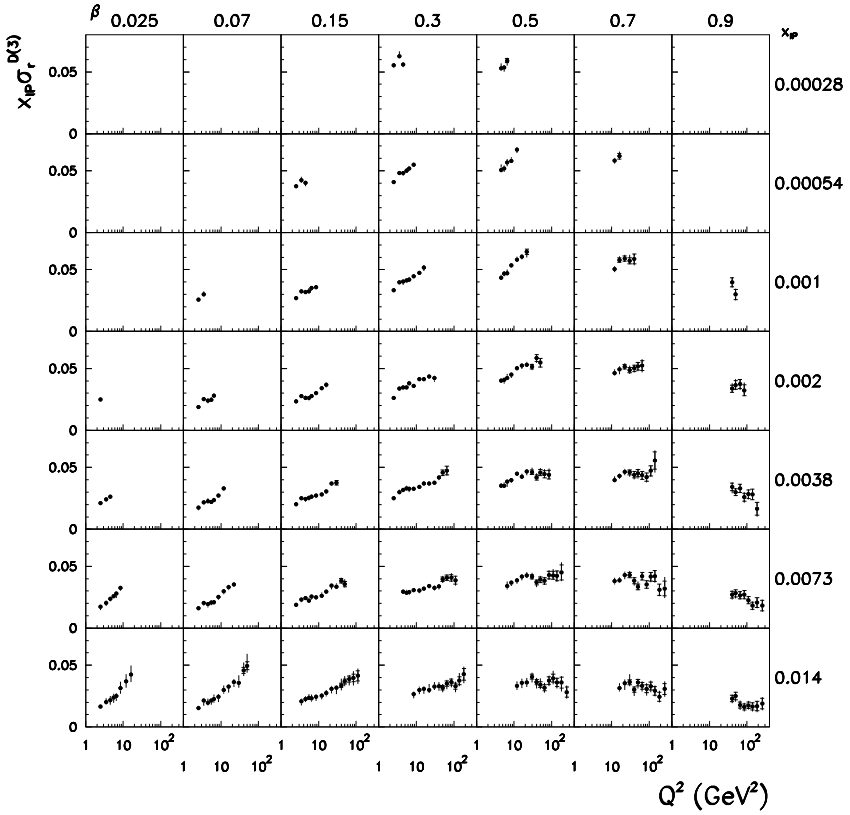

Figure 7.7: *The reduced diffractive cross section multiplied by $x_{\rm IP}$, $x_{\rm IP}\sigma_r^{D(3)}$, as a function of Q^2 for different β and $x_{\rm IP}$ regions. The inner error bars indicate the statistical uncertainties, the outer bars represent the statistical and systematic uncertainties added in quadrature. The normalisation uncertainty of $\pm 2.25\,\%$ is not shown.*

trajectory, determined to be $\alpha'_{\rm IP} = 0.25\,{\rm GeV}^{-2}$ in soft hadron-hadron collisions [96], has been measured to be smaller in the diffractive production of vector mesons [99]. It is

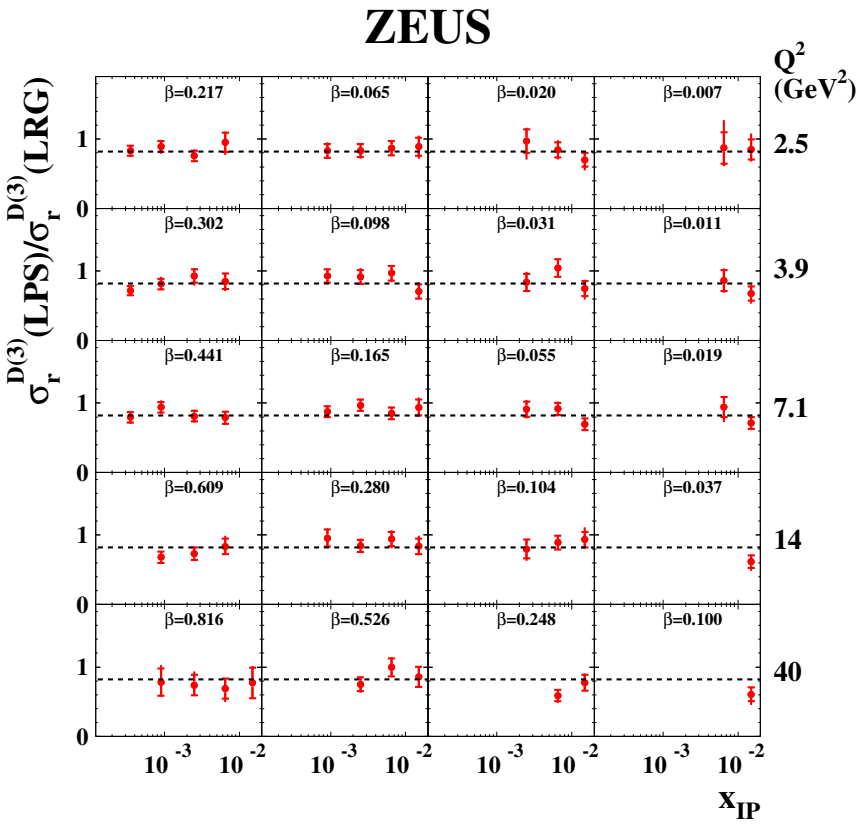

Figure 7.8: *The ratio of the reduced diffractive cross sections $\sigma_r^{D(3)}$ obtained with the LPS and the LRG methods as a function of $x_{\rm IP}$ for different values of β and Q^2. The inner error bars indicate the statistical uncertainties, the outer bars represent the statistical and systematic uncertainties added in quadrature. The normalisation uncertainty of $^{+12}_{-10}\%$ is not shown. The lines indicate the average value of the ratio.*

interesting to determine if such deviations from the behaviour of the hadron-hadron data are also apparent in the inclusive diffractive dissociation of virtual photons.

The sum of two contributions was fitted to the data according to

$$F_2^{D(4)} = f_{\mathrm{IP}}(x_{\mathrm{IP}}, t) \cdot F_2^{\mathrm{IP}}(\beta, Q^2) + n_{\mathrm{IR}} \cdot f_{\mathrm{IR}}(x_{\mathrm{IP}}, t) \cdot F_2^{\mathrm{IR}}(\beta, Q^2). \tag{7.8}$$

The first term of this sum is the contribution from Pomeron exchange and the second one, from the exchanges of the Reggeon trajectories. The Pomeron flux was parametrised as [1]

$$f_{\mathrm{IP}}(x_{\mathrm{IP}}, t) = \frac{e^{B_{\mathrm{IP}} t}}{x_{\mathrm{IP}}^{2\alpha_{\mathrm{IP}}(t)-1}}, \tag{7.9}$$

and the Reggeon flux as

$$f_{\mathrm{IR}}(x_{\mathrm{IP}}, t) = \frac{e^{B_{\mathrm{IR}} t}}{x_{\mathrm{IP}}^{2\alpha_{\mathrm{IR}}(t)-1}}, \tag{7.10}$$

assuming that the Pomeron and Reggeon trajectories are both linear:

$$\alpha_{\mathrm{IP}}(t) = \alpha'_{\mathrm{IP}} t + \alpha_{\mathrm{IP}}(0), \tag{7.11}$$

$$\alpha_{\mathrm{IR}}(t) = \alpha'_{\mathrm{IR}} t + \alpha_{\mathrm{IR}}(0). \tag{7.12}$$

The assumption that $F_2^{D(4)}$ can be expressed as the product of a flux, depending only on x_{IP} and t, and the structure function of a particle-like object is known as the *Regge factorisation* hypothesis. It gives a fair description of the data, although it has no justification in QCD, where only the concept of diffractive PDFs, which are functions of $x_{\mathrm{IP}}, t, \beta, Q^2$, has a firm basis.

A fit to the $\sigma_r^{D(3)}$ data was performed in a way modified according to Equation (7.7). The Pomeron and Reggeon fluxes integrated over t[1] take the form of

$$f_{\mathrm{IP}}(x_{\mathrm{IP}}) = \frac{1}{x_{\mathrm{IP}}^{2\alpha_{\mathrm{IP}}(0)-1}} \frac{1 - e^{-b_{\mathrm{IP}}(x_{\mathrm{IP}})}}{b_{\mathrm{IP}}(x_{\mathrm{IP}})}, \tag{7.13}$$

$$f_{\mathrm{IR}}(x_{\mathrm{IP}}) = \frac{1}{x_{\mathrm{IP}}^{2\alpha_{\mathrm{IR}}(0)-1}} \frac{1 - e^{-b_{\mathrm{IR}}(x_{\mathrm{IP}})}}{b_{\mathrm{IR}}(x_{\mathrm{IP}})}, \tag{7.14}$$

where the b_{IP} and b_{IR} functions of x_{IP} are equal to, respectively:

$$b_{\mathrm{IP}}(x_{\mathrm{IP}}) = B_{\mathrm{IP}} + 2\alpha'_{\mathrm{IP}} \ln \frac{0.01}{x_{\mathrm{IP}}}, \tag{7.15}$$

$$b_{\mathrm{IR}}(x_{\mathrm{IP}}) = B_{\mathrm{IR}} + 2\alpha'_{\mathrm{IR}} \ln \frac{1}{x_{\mathrm{IP}}}. \tag{7.16}$$

[1]Since the Pomeron and Reggeon fluxes, (7.9) and (7.10), converge quickly to 0 when $|t| \to \infty$, the accurate integration could be performed in the range of $|t| \leq 1\,\mathrm{GeV}^{-2}$.

Since the t-slope of the Pomeron flux at $x_{\mathrm{IP}} = 0.01$ was known from the LPS measurement, it was applied in the fitting of the $\sigma_r^{D(3)}$ LRG data. Such an adjusting of the shape of the Pomeron flux results in above relation for $b_{\mathrm{IP}}(x_{\mathrm{IP}})$.

The parameters obtained from the fit were the Pomeron trajectory, the intercept of the Reggeon trajectory, and the Reggeon normalisation term n_{IR}. The slope of the Pomeron trajectory B_{IP} was taken from the fit to the LPS data. The Reggeon structure function $F_2^{\mathrm{IR}}(\beta, Q^2)$ was taken to be equal to the pion structure function as parametrised by GRV [100–102]. The fit was limited to $y < 0.5$ to reduce the influence of F_L^D.

The lines in Figs. 7.4-7.6 show the result of the fit. The obtained Pomeron intercept is

$$\alpha_{\mathrm{IP}}(0) = 1.118 \pm 0.007(\mathrm{exp.})^{+0.019}_{-0.010}(\mathrm{model}). \tag{7.17}$$

In the fit, α'_{IP} was kept fixed to zero, $\alpha_{\mathrm{IR}}(0)$ to $0.75\,\mathrm{GeV}^{-2}$ and B_{IP} to $7.2\,\mathrm{GeV}^{-2}$. The first uncertainty is that from the fit in which the quadratic sum of statistical and systematic uncertainties was used; this is dominated by the systematic uncertainty. The model uncertainty reflects the variation of α'_{IP} between 0 and $0.1\,\mathrm{GeV}^{-2}$ and that of $\alpha_{\mathrm{IR}}(0)$ between 0.55 and 0.75. In addition the pion structure function parametrisation was changed from that of GRV to that of Owens [103]. The quality of the fit is good, with $\chi^2/ndf = 75.5/185$. The resulting $\alpha_{\mathrm{IP}}(0)$ is consistent with the values obtained by the H1 collaboration from the analysis based on a large rapidity gap method: $\alpha_{\mathrm{IP}}(0) = 1.118 \pm 0.008(\mathrm{exp.})^{+0.029}_{-0.010}(\mathrm{model})$ [104] and from the events with leading proton in the final state: $\alpha_{\mathrm{IP}}(0) = 1.114 \pm 0.018(\mathrm{stat.}) \pm 0.012(\mathrm{syst.})^{+0.040}_{-0.020}(\mathrm{model})$ [105]. If α'_{IP} is fixed to $0.25\,\mathrm{GeV}^{-2}$, then one obtains $\alpha_{\mathrm{IP}}(0) = 1.149 \pm 0.007(\mathrm{exp.})$ with $\alpha_{\mathrm{IR}}(0)$ fixed to 0.75.

The Pomeron intercept obtained from the Regge fit where only the statistical uncertainties were taken into account amounts to $\alpha_{\mathrm{IP}}(0) = 1.140 \pm 0.002(\mathrm{stat.})$. This fitting was performed with standard input parameters. The quality of the fit is: $\chi^2/ndf = 1039.6/185$.

Figure 7.9 shows $\alpha_{\mathrm{IP}}(0)$ as a function of Q^2. This dependence was obtained by repeating the fit described earlier in bins of Q^2. In the region explored, the data do not exhibit a significant dependence on Q^2.

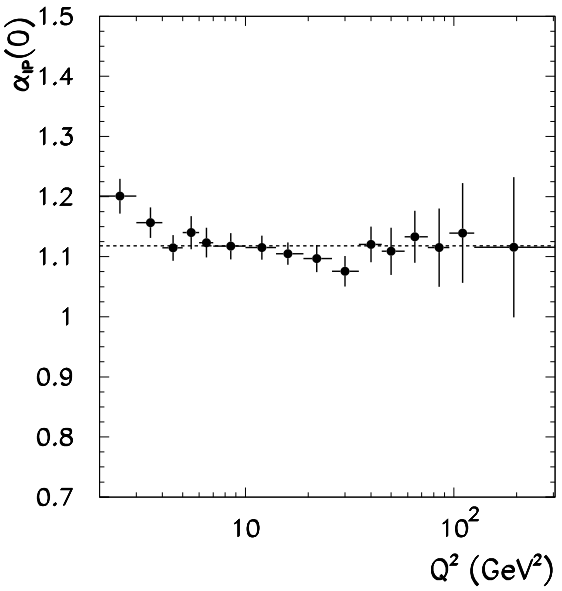

Figure 7.9: *The Pomeron intercept $\alpha_{\rm IP}(0)$ as a function of Q^2. The horizontal dashed line corresponds to the Pomeron intercept obtained from the fit to the full data set.*

Chapter 8

Conclusions

The study of the diffractive process $\gamma^* p \to Xp$ in deep inelastic e^+p scattering with the ZEUS detector at HERA is presented in this thesis. The high statistic data collected in the years 1999 and 2000, corresponding to an integrated luminosity of $62.07\,\mathrm{pb}^{-1}$, have been worked out. It allowed for a considerable decreasing of the statistical uncertainties of the measurement. The reduced diffractive cross section $\sigma_r^{D(3)}$ has been extracted with the requirement of a large rapidity gap (LRG) in the forward direction. The analysis was restricted to the kinematic range $2 < Q^2 < 305\,\mathrm{GeV}^2$, $40 < W < 240\,\mathrm{GeV}$, $2 < M_X < 25\,\mathrm{GeV}$ and covers the proton fractional momentum loss of $0.0002 < x_{\rm IP} < 0.02$.

The obtained $\sigma_r^{D(3)}$ falls with $x_{\rm IP}$ faster than $1/x_{\rm IP}$ for $x_{\rm IP} \lesssim 0.01$. The data are in agreement with Regge theory predictions. From the $x_{\rm IP}$ dependence of $\sigma_r^{D(3)}$ the Pomeron intercept $\alpha_{\rm IP}(0)$ was extracted:

$$\alpha_{\rm IP}(0) = 1.118 \pm 0.007(\mathrm{exp.})^{+0.019}_{-0.010}(\mathrm{model}). \tag{8.1}$$

It is only marginally higher than that of the soft Pomeron. It agrees with recent measurements of H1 collaboration [104, 105]. No significant dependence of $\alpha_{\rm IP}(0)$ on Q^2 is observed.

The flat ratio of the $\sigma_r^{D(3)}$ results obtained from the LPS analysis and from the LRG results shows that these two measurements are consistent, apart for a normalisation shift ascribed to proton-dissociative events and in spite of different sources of systematic uncertainties. This result lends support to the hypothesis that, apart from proton dissociation, the LRG method is sensitive to the same physics.

Appendix A

Tables of the reduced diffractive cross section $x_{\rm IP}\sigma_r^{D(3)}$

Table A.1: *The reduced diffractive cross section multiplied by $x_{\rm IP}$, $x_{\rm IP}\sigma_r^{D(3)}$, as a function of $x_{\rm IP}$ for different values of M_X, for $Q^2 = 2.5\ GeV^2$. The normalisation uncertainty of $\pm 2.25\%$ is not included.*

Q^2 (GeV^2)	M_X (GeV)	β	$x_{\rm IP}$	$x_{\rm IP}\sigma_r^{D(3)} \pm (stat) \pm (syst)$
2.5	3	0.2174	0.00028	$0.0591 \pm 0.0007^{+0.0064}_{-0.0071}$
2.5	3	0.2174	0.00054	$0.0403 \pm 0.0004^{+0.0038}_{-0.0038}$
2.5	3	0.2174	0.001	$0.0315 \pm 0.0004^{+0.0023}_{-0.0022}$
2.5	3	0.2174	0.002	$0.0253 \pm 0.0004^{+0.0024}_{-0.0012}$
2.5	3	0.2174	0.0038	$0.0234 \pm 0.0004^{+0.0011}_{-0.0010}$
2.5	5	0.0909	0.00054	$0.0416 \pm 0.0008^{+0.0045}_{-0.0038}$
2.5	5	0.0909	0.001	$0.0286 \pm 0.0005^{+0.0021}_{-0.0026}$
2.5	5	0.0909	0.002	$0.0223 \pm 0.0005^{+0.0012}_{-0.0017}$
2.5	5	0.0909	0.0038	$0.0192 \pm 0.0005^{+0.0009}_{-0.0021}$
2.5	5	0.0909	0.0073	$0.0170 \pm 0.0006^{+0.0015}_{-0.0026}$
2.5	5	0.0909	0.014	$0.0174 \pm 0.0008^{+0.0028}_{-0.0017}$
2.5	8	0.0376	0.002	$0.0228 \pm 0.0005^{+0.0014}_{-0.0023}$
2.5	8	0.0376	0.0038	$0.0201 \pm 0.0004^{+0.0010}_{-0.0015}$
2.5	8	0.0376	0.0073	$0.0183 \pm 0.0005^{+0.0003}_{-0.0028}$
2.5	8	0.0376	0.014	$0.0181 \pm 0.0007^{+0.0023}_{-0.0017}$
2.5	13	0.0146	0.0038	$0.0274 \pm 0.0008^{+0.0020}_{-0.0031}$
2.5	13	0.0146	0.0073	$0.0210 \pm 0.0007^{+0.0018}_{-0.0042}$
2.5	13	0.0146	0.014	$0.0202 \pm 0.0008^{+0.0020}_{-0.0036}$
2.5	20	0.0062	0.0073	$0.0265 \pm 0.0016^{+0.0044}_{-0.0087}$
2.5	20	0.0062	0.014	$0.0233 \pm 0.0012^{+0.0044}_{-0.0078}$

Table A.2: *The reduced diffractive cross section multiplied by $x_{\rm IP}$, $x_{\rm IP}\sigma_r^{D(3)}$, as a function of $x_{\rm IP}$ for different values of M_X, for $Q^2 = 3.5\ GeV^2$ and $4.5\ GeV^2$. The normalisation uncertainty of $\pm 2.25\%$ is not included.*

Q^2 (GeV^2)	M_X (GeV)	β	$x_{\rm IP}$	$x_{\rm IP}\sigma_r^{D(3)} \pm (stat) \pm (syst)$
3.5	3	0.2800	0.00028	$0.0583 \pm 0.0008^{+0.0072}_{-0.0060}$
3.5	3	0.2800	0.00054	$0.0457 \pm 0.0006^{+0.0045}_{-0.0037}$
3.5	3	0.2800	0.001	$0.0373 \pm 0.0005^{+0.0028}_{-0.0028}$
3.5	3	0.2800	0.002	$0.0314 \pm 0.0005^{+0.0018}_{-0.0015}$
3.5	3	0.2800	0.0038	$0.0274 \pm 0.0005^{+0.0017}_{-0.0016}$
3.5	3	0.2800	0.0073	$0.0262 \pm 0.0007^{+0.0007}_{-0.0022}$
3.5	5	0.1228	0.00054	$0.0409 \pm 0.0008^{+0.0043}_{-0.0037}$
3.5	5	0.1228	0.001	$0.0315 \pm 0.0006^{+0.0020}_{-0.0029}$
3.5	5	0.1228	0.002	$0.0266 \pm 0.0005^{+0.0010}_{-0.0016}$
3.5	5	0.1228	0.0038	$0.0239 \pm 0.0005^{+0.0008}_{-0.0016}$
3.5	5	0.1228	0.0073	$0.0220 \pm 0.0007^{+0.0019}_{-0.0017}$
3.5	5	0.1228	0.014	$0.0205 \pm 0.0008^{+0.0012}_{-0.0038}$
3.5	8	0.0519	0.002	$0.0248 \pm 0.0005^{+0.0022}_{-0.0015}$
3.5	8	0.0519	0.0038	$0.0215 \pm 0.0005^{+0.0011}_{-0.0012}$
3.5	8	0.0519	0.0073	$0.0200 \pm 0.0005^{+0.0010}_{-0.0021}$
3.5	8	0.0519	0.014	$0.0206 \pm 0.0007^{+0.0010}_{-0.0044}$
3.5	13	0.0203	0.0038	$0.0258 \pm 0.0008^{+0.0015}_{-0.0028}$
3.5	13	0.0203	0.0073	$0.0216 \pm 0.0007^{+0.0025}_{-0.0030}$
3.5	13	0.0203	0.014	$0.0221 \pm 0.0009^{+0.0038}_{-0.0023}$
3.5	20	0.0087	0.0073	$0.0280 \pm 0.0013^{+0.0022}_{-0.0056}$
3.5	20	0.0087	0.014	$0.0273 \pm 0.0010^{+0.0062}_{-0.0043}$
4.5	3	0.3333	0.00028	$0.0530 \pm 0.0009^{+0.0059}_{-0.0046}$
4.5	3	0.3333	0.00054	$0.0471 \pm 0.0007^{+0.0046}_{-0.0040}$
4.5	3	0.3333	0.001	$0.0393 \pm 0.0007^{+0.0026}_{-0.0031}$
4.5	3	0.3333	0.002	$0.0345 \pm 0.0007^{+0.0020}_{-0.0015}$
4.5	3	0.3333	0.0038	$0.0306 \pm 0.0006^{+0.0015}_{-0.0012}$
4.5	3	0.3333	0.0073	$0.0287 \pm 0.0008^{+0.0022}_{-0.0006}$
4.5	5	0.1525	0.00054	$0.0406 \pm 0.0009^{+0.0033}_{-0.0053}$
4.5	5	0.1525	0.001	$0.0314 \pm 0.0006^{+0.0035}_{-0.0018}$
4.5	5	0.1525	0.002	$0.0262 \pm 0.0006^{+0.0020}_{-0.0010}$
4.5	5	0.1525	0.0038	$0.0244 \pm 0.0007^{+0.0012}_{-0.0017}$
4.5	5	0.1525	0.0073	$0.0236 \pm 0.0007^{+0.0007}_{-0.0024}$
4.5	5	0.1525	0.014	$0.0226 \pm 0.0010^{+0.0019}_{-0.0028}$
4.5	8	0.0657	0.002	$0.0252 \pm 0.0006^{+0.0011}_{-0.0017}$
4.5	8	0.0657	0.0038	$0.0227 \pm 0.0005^{+0.0022}_{-0.0007}$
4.5	8	0.0657	0.0073	$0.0197 \pm 0.0007^{+0.0006}_{-0.0020}$
4.5	8	0.0657	0.014	$0.0188 \pm 0.0008^{+0.0035}_{-0.0029}$
4.5	13	0.0259	0.0038	$0.0265 \pm 0.0007^{+0.0010}_{-0.0017}$
4.5	13	0.0259	0.0073	$0.0237 \pm 0.0007^{+0.0014}_{-0.0026}$
4.5	13	0.0259	0.014	$0.0228 \pm 0.0009^{+0.0022}_{-0.0029}$
4.5	20	0.0111	0.0073	$0.0283 \pm 0.0010^{+0.0018}_{-0.0034}$
4.5	20	0.0111	0.014	$0.0278 \pm 0.0011^{+0.0058}_{-0.0050}$

Table A.3: *The reduced diffractive cross section multiplied by $x_{\rm IP}$, $x_{\rm IP}\sigma_r^{D(3)}$, as a function of $x_{\rm IP}$ for different values of M_X, for $Q^2 = 5.5\ GeV^2$ and $6.5\ GeV^2$. The normalisation uncertainty of $\pm 2.25\%$ is not included.*

Q^2 (GeV^2)	M_X (GeV)	β	$x_{\rm IP}$	$x_{\rm IP}\sigma_r^{D(3)} \pm (stat) \pm (syst)$
5.5	3	0.3793	0.00028	$0.0553 \pm 0.0011^{+0.0062}_{-0.0067}$
5.5	3	0.3793	0.00054	$0.0504 \pm 0.0008^{+0.0048}_{-0.0057}$
5.5	3	0.3793	0.001	$0.0427 \pm 0.0008^{+0.0033}_{-0.0032}$
5.5	3	0.3793	0.002	$0.0354 \pm 0.0007^{+0.0020}_{-0.0033}$
5.5	3	0.3793	0.0038	$0.0317 \pm 0.0007^{+0.0015}_{-0.0017}$
5.5	3	0.3793	0.0073	$0.0290 \pm 0.0009^{+0.0010}_{-0.0026}$
5.5	5	0.1803	0.00054	$0.0420 \pm 0.0011^{+0.0035}_{-0.0032}$
5.5	5	0.1803	0.001	$0.0340 \pm 0.0007^{+0.0022}_{-0.0031}$
5.5	5	0.1803	0.002	$0.0261 \pm 0.0006^{+0.0015}_{-0.0020}$
5.5	5	0.1803	0.0038	$0.0251 \pm 0.0007^{+0.0012}_{-0.0017}$
5.5	5	0.1803	0.0073	$0.0220 \pm 0.0007^{+0.0021}_{-0.0015}$
5.5	5	0.1803	0.014	$0.0229 \pm 0.0011^{+0.0019}_{-0.0015}$
5.5	8	0.0791	0.002	$0.0249 \pm 0.0005^{+0.0018}_{-0.0010}$
5.5	8	0.0791	0.0038	$0.0231 \pm 0.0006^{+0.0008}_{-0.0021}$
5.5	8	0.0791	0.0073	$0.0200 \pm 0.0006^{+0.0022}_{-0.0018}$
5.5	8	0.0791	0.014	$0.0212 \pm 0.0009^{+0.0027}_{-0.0028}$
5.5	13	0.0315	0.0038	$0.0281 \pm 0.0007^{+0.0008}_{-0.0022}$
5.5	13	0.0315	0.0073	$0.0256 \pm 0.0007^{+0.0016}_{-0.0022}$
5.5	13	0.0315	0.014	$0.0240 \pm 0.0010^{+0.0036}_{-0.0041}$
5.5	20	0.0136	0.0073	$0.0298 \pm 0.0011^{+0.0021}_{-0.0020}$
5.5	20	0.0136	0.014	$0.0284 \pm 0.0010^{+0.0036}_{-0.0047}$
6.5	3	0.4194	0.00028	$0.0568 \pm 0.0014^{+0.0064}_{-0.0057}$
6.5	3	0.4194	0.00054	$0.0542 \pm 0.0009^{+0.0050}_{-0.0045}$
6.5	3	0.4194	0.001	$0.0437 \pm 0.0009^{+0.0038}_{-0.0025}$
6.5	3	0.4194	0.002	$0.0388 \pm 0.0008^{+0.0025}_{-0.0013}$
6.5	3	0.4194	0.0038	$0.0342 \pm 0.0009^{+0.0009}_{-0.0020}$
6.5	3	0.4194	0.0073	$0.0316 \pm 0.0009^{+0.0010}_{-0.0026}$
6.5	5	0.2063	0.001	$0.0367 \pm 0.0009^{+0.0026}_{-0.0033}$
6.5	5	0.2063	0.002	$0.0313 \pm 0.0008^{+0.0016}_{-0.0022}$
6.5	5	0.2063	0.0038	$0.0263 \pm 0.0008^{+0.0010}_{-0.0015}$
6.5	5	0.2063	0.0073	$0.0239 \pm 0.0008^{+0.0026}_{-0.0023}$
6.5	5	0.2063	0.014	$0.0233 \pm 0.0011^{+0.0027}_{-0.0022}$
6.5	8	0.0922	0.002	$0.0269 \pm 0.0006^{+0.0018}_{-0.0014}$
6.5	8	0.0922	0.0038	$0.0241 \pm 0.0006^{+0.0019}_{-0.0008}$
6.5	8	0.0922	0.0073	$0.0227 \pm 0.0007^{+0.0014}_{-0.0021}$
6.5	8	0.0922	0.014	$0.0219 \pm 0.0009^{+0.0044}_{-0.0020}$
6.5	13	0.0370	0.0038	$0.0276 \pm 0.0008^{+0.0020}_{-0.0010}$
6.5	13	0.0370	0.0073	$0.0241 \pm 0.0008^{+0.0014}_{-0.0020}$
6.5	13	0.0370	0.014	$0.0243 \pm 0.0010^{+0.0020}_{-0.0044}$
6.5	20	0.0160	0.0073	$0.0328 \pm 0.0013^{+0.0014}_{-0.0034}$
6.5	20	0.0160	0.014	$0.0283 \pm 0.0013^{+0.0034}_{-0.0065}$

Table A.4: *The reduced diffractive cross section multiplied by $x_{\rm IP}$, $x_{\rm IP}\sigma_r^{D(3)}$, as a function of $x_{\rm IP}$ for different values of M_X, for $Q^2 = 8.5\ GeV^2$ and $12\ GeV^2$. The normalisation uncertainty of $\pm 2.25\%$ is not included.*

Q^2 (GeV^2)	M_X (GeV)	β	$x_{\rm IP}$	$x_{\rm IP}\sigma_r^{D(3)} \pm (stat) \pm (syst)$
8.5	3	0.4857	0.00054	$0.0564 \pm 0.0007^{+0.0055}_{-0.0048}$
8.5	3	0.4857	0.001	$0.0496 \pm 0.0007^{+0.0035}_{-0.0037}$
8.5	3	0.4857	0.002	$0.0421 \pm 0.0006^{+0.0020}_{-0.0026}$
8.5	3	0.4857	0.0038	$0.0367 \pm 0.0006^{+0.0009}_{-0.0020}$
8.5	3	0.4857	0.0073	$0.0351 \pm 0.0007^{+0.0010}_{-0.0021}$
8.5	5	0.2537	0.001	$0.0436 \pm 0.0007^{+0.0037}_{-0.0026}$
8.5	5	0.2537	0.002	$0.0337 \pm 0.0006^{+0.0023}_{-0.0020}$
8.5	5	0.2537	0.0038	$0.0305 \pm 0.0006^{+0.0012}_{-0.0020}$
8.5	5	0.2537	0.0073	$0.0273 \pm 0.0006^{+0.0011}_{-0.0010}$
8.5	5	0.2537	0.014	$0.0266 \pm 0.0008^{+0.0021}_{-0.0032}$
8.5	8	0.1172	0.002	$0.0303 \pm 0.0005^{+0.0014}_{-0.0017}$
8.5	8	0.1172	0.0038	$0.0263 \pm 0.0005^{+0.0008}_{-0.0014}$
8.5	8	0.1172	0.0073	$0.0243 \pm 0.0005^{+0.0016}_{-0.0016}$
8.5	8	0.1172	0.014	$0.0237 \pm 0.0007^{+0.0017}_{-0.0038}$
8.5	13	0.0479	0.0038	$0.0318 \pm 0.0006^{+0.0012}_{-0.0018}$
8.5	13	0.0479	0.0073	$0.0287 \pm 0.0006^{+0.0013}_{-0.0027}$
8.5	13	0.0479	0.014	$0.0260 \pm 0.0007^{+0.0036}_{-0.0033}$
8.5	20	0.0208	0.0073	$0.0358 \pm 0.0011^{+0.0021}_{-0.0035}$
8.5	20	0.0208	0.014	$0.0353 \pm 0.0009^{+0.0050}_{-0.0053}$
12	3	0.5714	0.00054	$0.0619 \pm 0.0010^{+0.0058}_{-0.0055}$
12	3	0.5714	0.001	$0.0537 \pm 0.0009^{+0.0044}_{-0.0035}$
12	3	0.5714	0.002	$0.0468 \pm 0.0008^{+0.0032}_{-0.0021}$
12	3	0.5714	0.0038	$0.0420 \pm 0.0008^{+0.0024}_{-0.0016}$
12	3	0.5714	0.0073	$0.0384 \pm 0.0008^{+0.0018}_{-0.0019}$
12	5	0.3243	0.001	$0.0476 \pm 0.0009^{+0.0032}_{-0.0040}$
12	5	0.3243	0.002	$0.0413 \pm 0.0008^{+0.0023}_{-0.0020}$
12	5	0.3243	0.0038	$0.0336 \pm 0.0008^{+0.0012}_{-0.0017}$
12	5	0.3243	0.0073	$0.0300 \pm 0.0007^{+0.0023}_{-0.0019}$
12	5	0.3243	0.014	$0.0305 \pm 0.0010^{+0.0026}_{-0.0040}$
12	8	0.1579	0.002	$0.0344 \pm 0.0006^{+0.0018}_{-0.0020}$
12	8	0.1579	0.0038	$0.0289 \pm 0.0006^{+0.0012}_{-0.0016}$
12	8	0.1579	0.0073	$0.0267 \pm 0.0006^{+0.0014}_{-0.0015}$
12	8	0.1579	0.014	$0.0259 \pm 0.0007^{+0.0028}_{-0.0022}$
12	13	0.0663	0.0038	$0.0345 \pm 0.0008^{+0.0013}_{-0.0016}$
12	13	0.0663	0.0073	$0.0303 \pm 0.0007^{+0.0013}_{-0.0018}$
12	13	0.0663	0.014	$0.0314 \pm 0.0009^{+0.0026}_{-0.0030}$
12	20	0.0291	0.0073	$0.0376 \pm 0.0012^{+0.0029}_{-0.0032}$
12	20	0.0291	0.014	$0.0348 \pm 0.0010^{+0.0049}_{-0.0050}$

Table A.5: *The reduced diffractive cross section multiplied by $x_{\rm IP}$, $x_{\rm IP}\sigma_r^{D(3)}$, as a function of $x_{\rm IP}$ for different values of M_X, for $Q^2 = 16\,GeV^2$ and $22\,GeV^2$. The normalisation uncertainty of $\pm 2.25\%$ is not included.*

Q^2 (GeV^2)	M_X (GeV)	β	$x_{\rm IP}$	$x_{\rm IP}\sigma_r^{D(3)} \pm (stat) \pm (syst)$
16	3	0.6400	0.00054	$0.0622 \pm 0.0017^{+0.0063}_{-0.0056}$
16	3	0.6400	0.001	$0.0565 \pm 0.0012^{+0.0041}_{-0.0037}$
16	3	0.6400	0.002	$0.0505 \pm 0.0011^{+0.0020}_{-0.0032}$
16	3	0.6400	0.0038	$0.0418 \pm 0.0010^{+0.0018}_{-0.0021}$
16	3	0.6400	0.0073	$0.0408 \pm 0.0011^{+0.0021}_{-0.0016}$
16	3	0.6400	0.014	$0.0361 \pm 0.0014^{+0.0032}_{-0.0033}$
16	5	0.3902	0.001	$0.0543 \pm 0.0014^{+0.0046}_{-0.0035}$
16	5	0.3902	0.002	$0.0437 \pm 0.0011^{+0.0019}_{-0.0023}$
16	5	0.3902	0.0038	$0.0383 \pm 0.0010^{+0.0023}_{-0.0015}$
16	5	0.3902	0.0073	$0.0359 \pm 0.0010^{+0.0013}_{-0.0017}$
16	5	0.3902	0.014	$0.0333 \pm 0.0011^{+0.0019}_{-0.0046}$
16	8	0.2000	0.002	$0.0382 \pm 0.0010^{+0.0025}_{-0.0019}$
16	8	0.2000	0.0038	$0.0322 \pm 0.0007^{+0.0017}_{-0.0013}$
16	8	0.2000	0.0073	$0.0301 \pm 0.0008^{+0.0010}_{-0.0018}$
16	8	0.2000	0.014	$0.0294 \pm 0.0009^{+0.0017}_{-0.0026}$
16	13	0.0865	0.0038	$0.0388 \pm 0.0012^{+0.0008}_{-0.0033}$
16	13	0.0865	0.0073	$0.0324 \pm 0.0008^{+0.0017}_{-0.0019}$
16	13	0.0865	0.014	$0.0330 \pm 0.0010^{+0.0017}_{-0.0045}$
16	20	0.0385	0.0073	$0.0413 \pm 0.0017^{+0.0035}_{-0.0042}$
16	20	0.0385	0.014	$0.0371 \pm 0.0012^{+0.0044}_{-0.0049}$
22	3	0.7097	0.00054	$0.0566 \pm 0.0026^{+0.0066}_{-0.0049}$
22	3	0.7097	0.001	$0.0552 \pm 0.0016^{+0.0037}_{-0.0056}$
22	3	0.7097	0.002	$0.0481 \pm 0.0014^{+0.0032}_{-0.0039}$
22	3	0.7097	0.0038	$0.0429 \pm 0.0013^{+0.0015}_{-0.0023}$
22	3	0.7097	0.0073	$0.0400 \pm 0.0013^{+0.0013}_{-0.0029}$
22	3	0.7097	0.014	$0.0366 \pm 0.0014^{+0.0026}_{-0.0040}$
22	5	0.4681	0.001	$0.0616 \pm 0.0019^{+0.0044}_{-0.0044}$
22	5	0.4681	0.002	$0.0509 \pm 0.0015^{+0.0031}_{-0.0038}$
22	5	0.4681	0.0038	$0.0440 \pm 0.0013^{+0.0009}_{-0.0028}$
22	5	0.4681	0.0073	$0.0409 \pm 0.0013^{+0.0019}_{-0.0024}$
22	5	0.4681	0.014	$0.0347 \pm 0.0013^{+0.0041}_{-0.0030}$
22	8	0.2558	0.002	$0.0404 \pm 0.0011^{+0.0030}_{-0.0015}$
22	8	0.2558	0.0038	$0.0358 \pm 0.0010^{+0.0015}_{-0.0014}$
22	8	0.2558	0.0073	$0.0326 \pm 0.0009^{+0.0011}_{-0.0021}$
22	8	0.2558	0.014	$0.0304 \pm 0.0010^{+0.0036}_{-0.0034}$
22	13	0.1152	0.0038	$0.0389 \pm 0.0013^{+0.0019}_{-0.0017}$
22	13	0.1152	0.0073	$0.0355 \pm 0.0010^{+0.0018}_{-0.0021}$
22	13	0.1152	0.014	$0.0332 \pm 0.0011^{+0.0033}_{-0.0032}$
22	20	0.0521	0.014	$0.0395 \pm 0.0014^{+0.0026}_{-0.0044}$

Table A.6: *The reduced diffractive cross section multiplied by $x_{\rm IP}$, $x_{\rm IP}\sigma_r^{D(3)}$, as a function of $x_{\rm IP}$ for different values of M_X, for $Q^2 = 30\,GeV^2$ and $40\,GeV^2$. The normalisation uncertainty of $\pm 2.25\%$ is not included.*

Q^2 (GeV^2)	M_X (GeV)	β	$x_{\rm IP}$	$x_{\rm IP}\sigma_r^{D(3)} \pm (stat) \pm (syst)$
30	3	0.7692	0.001	$0.0491 \pm 0.0019^{+0.0043}_{-0.0041}$
30	3	0.7692	0.002	$0.0423 \pm 0.0017^{+0.0047}_{-0.0022}$
30	3	0.7692	0.0038	$0.0384 \pm 0.0016^{+0.0024}_{-0.0026}$
30	3	0.7692	0.0073	$0.0385 \pm 0.0017^{+0.0032}_{-0.0008}$
30	3	0.7692	0.014	$0.0357 \pm 0.0019^{+0.0044}_{-0.0021}$
30	5	0.5455	0.001	$0.0598 \pm 0.0027^{+0.0055}_{-0.0031}$
30	5	0.5455	0.002	$0.0508 \pm 0.0018^{+0.0022}_{-0.0030}$
30	5	0.5455	0.0038	$0.0455 \pm 0.0018^{+0.0032}_{-0.0012}$
30	5	0.5455	0.0073	$0.0418 \pm 0.0018^{+0.0024}_{-0.0022}$
30	5	0.5455	0.014	$0.0387 \pm 0.0018^{+0.0033}_{-0.0043}$
30	8	0.3191	0.002	$0.0437 \pm 0.0015^{+0.0025}_{-0.0023}$
30	8	0.3191	0.0038	$0.0373 \pm 0.0012^{+0.0010}_{-0.0017}$
30	8	0.3191	0.0073	$0.0318 \pm 0.0011^{+0.0014}_{-0.0016}$
30	8	0.3191	0.014	$0.0336 \pm 0.0014^{+0.0025}_{-0.0025}$
30	13	0.1508	0.0038	$0.0392 \pm 0.0015^{+0.0016}_{-0.0018}$
30	13	0.1508	0.0073	$0.0354 \pm 0.0012^{+0.0023}_{-0.0011}$
30	13	0.1508	0.014	$0.0349 \pm 0.0015^{+0.0026}_{-0.0040}$
30	20	0.0698	0.014	$0.0363 \pm 0.0014^{+0.0053}_{-0.0039}$
40	3	0.8163	0.001	$0.0481 \pm 0.0029^{+0.0040}_{-0.0038}$
40	3	0.8163	0.002	$0.0408 \pm 0.0022^{+0.0025}_{-0.0029}$
40	3	0.8163	0.0038	$0.0358 \pm 0.0021^{+0.0012}_{-0.0030}$
40	3	0.8163	0.0073	$0.0315 \pm 0.0020^{+0.0012}_{-0.0034}$
40	3	0.8163	0.014	$0.0262 \pm 0.0020^{+0.0019}_{-0.0043}$
40	5	0.6154	0.002	$0.0500 \pm 0.0024^{+0.0033}_{-0.0033}$
40	5	0.6154	0.0038	$0.0428 \pm 0.0022^{+0.0028}_{-0.0020}$
40	5	0.6154	0.0073	$0.0376 \pm 0.0021^{+0.0004}_{-0.0030}$
40	5	0.6154	0.014	$0.0345 \pm 0.0022^{+0.0030}_{-0.0040}$
40	8	0.3846	0.002	$0.0535 \pm 0.0022^{+0.0027}_{-0.0039}$
40	8	0.3846	0.0038	$0.0418 \pm 0.0016^{+0.0013}_{-0.0019}$
40	8	0.3846	0.0073	$0.0340 \pm 0.0015^{+0.0014}_{-0.0020}$
40	8	0.3846	0.014	$0.0357 \pm 0.0017^{+0.0014}_{-0.0050}$
40	13	0.1914	0.0038	$0.0437 \pm 0.0021^{+0.0019}_{-0.0015}$
40	13	0.1914	0.0073	$0.0371 \pm 0.0015^{+0.0016}_{-0.0022}$
40	13	0.1914	0.014	$0.0335 \pm 0.0016^{+0.0050}_{-0.0030}$
40	20	0.0909	0.014	$0.0445 \pm 0.0020^{+0.0046}_{-0.0035}$

Table A.7: *The reduced diffractive cross section multiplied by $x_{\rm IP}$, $x_{\rm IP}\sigma_r^{D(3)}$, as a function of $x_{\rm IP}$ for different values of M_X, for $Q^2 = 50\ GeV^2$, $65\ GeV^2$, and $85\ GeV^2$. The normalisation uncertainty of $\pm 2.25\%$ is not included.*

Q^2 (GeV^2)	M_X (GeV)	β	$x_{\rm IP}$	$x_{\rm IP}\sigma_r^{D(3)} \pm (stat) \pm (syst)$
50	3	0.8475	0.002	$0.0423 \pm 0.0030^{+0.0033}_{-0.0035}$
50	3	0.8475	0.0038	$0.0330 \pm 0.0024^{+0.0017}_{-0.0023}$
50	3	0.8475	0.0073	$0.0287 \pm 0.0024^{+0.0009}_{-0.0022}$
50	3	0.8475	0.014	$0.0280 \pm 0.0026^{+0.0030}_{-0.0027}$
50	5	0.6667	0.002	$0.0501 \pm 0.0030^{+0.0028}_{-0.0031}$
50	5	0.6667	0.0038	$0.0509 \pm 0.0030^{+0.0008}_{-0.0046}$
50	5	0.6667	0.0073	$0.0348 \pm 0.0024^{+0.0028}_{-0.0019}$
50	5	0.6667	0.014	$0.0379 \pm 0.0028^{+0.0020}_{-0.0044}$
50	8	0.4386	0.002	$0.0546 \pm 0.0032^{+0.0026}_{-0.0034}$
50	8	0.4386	0.0038	$0.0459 \pm 0.0020^{+0.0030}_{-0.0017}$
50	8	0.4386	0.0073	$0.0396 \pm 0.0019^{+0.0024}_{-0.0013}$
50	8	0.4386	0.014	$0.0353 \pm 0.0019^{+0.0036}_{-0.0040}$
50	13	0.2283	0.0038	$0.0487 \pm 0.0028^{+0.0012}_{-0.0028}$
50	13	0.2283	0.0073	$0.0423 \pm 0.0018^{+0.0018}_{-0.0020}$
50	13	0.2283	0.014	$0.0348 \pm 0.0018^{+0.0030}_{-0.0035}$
50	20	0.1111	0.014	$0.0445 \pm 0.0022^{+0.0060}_{-0.0036}$
65	3	0.8784	0.002	$0.0398 \pm 0.0035^{+0.0021}_{-0.0038}$
65	3	0.8784	0.0038	$0.0304 \pm 0.0029^{+0.0021}_{-0.0018}$
65	3	0.8784	0.0073	$0.0255 \pm 0.0026^{+0.0011}_{-0.0022}$
65	3	0.8784	0.014	$0.0181 \pm 0.0024^{+0.0031}_{-0.0033}$
65	5	0.7222	0.002	$0.0480 \pm 0.0039^{+0.0038}_{-0.0033}$
65	5	0.7222	0.0038	$0.0424 \pm 0.0032^{+0.0019}_{-0.0020}$
65	5	0.7222	0.0073	$0.0411 \pm 0.0032^{+0.0022}_{-0.0014}$
65	5	0.7222	0.014	$0.0324 \pm 0.0030^{+0.0024}_{-0.0035}$
65	8	0.5039	0.0038	$0.0447 \pm 0.0023^{+0.0016}_{-0.0017}$
65	8	0.5039	0.0073	$0.0396 \pm 0.0022^{+0.0021}_{-0.0019}$
65	8	0.5039	0.014	$0.0342 \pm 0.0022^{+0.0021}_{-0.0032}$
65	13	0.2778	0.0073	$0.0425 \pm 0.0021^{+0.0019}_{-0.0024}$
65	13	0.2778	0.014	$0.0371 \pm 0.0021^{+0.0023}_{-0.0043}$
65	20	0.1398	0.014	$0.0435 \pm 0.0024^{+0.0032}_{-0.0046}$
85	3	0.9043	0.002	$0.0285 \pm 0.0045^{+0.0043}_{-0.0020}$
85	3	0.9043	0.0038	$0.0235 \pm 0.0033^{+0.0040}_{-0.0019}$
85	3	0.9043	0.0073	$0.0242 \pm 0.0033^{+0.0023}_{-0.0017}$
85	3	0.9043	0.014	$0.0168 \pm 0.0030^{+0.0021}_{-0.0031}$
85	5	0.7727	0.002	$0.0498 \pm 0.0070^{+0.0041}_{-0.0021}$
85	5	0.7727	0.0038	$0.0364 \pm 0.0037^{+0.0014}_{-0.0031}$
85	5	0.7727	0.0073	$0.0330 \pm 0.0036^{+0.0026}_{-0.0014}$
85	5	0.7727	0.014	$0.0301 \pm 0.0036^{+0.0021}_{-0.0034}$
85	8	0.5705	0.0038	$0.0485 \pm 0.0032^{+0.0023}_{-0.0019}$
85	8	0.5705	0.0073	$0.0438 \pm 0.0030^{+0.0021}_{-0.0036}$
85	8	0.5705	0.014	$0.0362 \pm 0.0028^{+0.0031}_{-0.0045}$
85	13	0.3346	0.0073	$0.0453 \pm 0.0027^{+0.0027}_{-0.0024}$
85	13	0.3346	0.014	$0.0428 \pm 0.0028^{+0.0026}_{-0.0035}$
85	20	0.1753	0.014	$0.0417 \pm 0.0029^{+0.0045}_{-0.0050}$

Table A.8: *The reduced diffractive cross section multiplied by $x_{\rm IP}$, $x_{\rm IP}\sigma_r^{D(3)}$, as a function of $x_{\rm IP}$ for different values of M_X, for $Q^2 = 110\ GeV^2$, $140\ GeV^2$, $185\ GeV^2$, and $255\ GeV^2$. The normalisation uncertainty of $\pm 2.25\%$ is not included.*

Q^2 (GeV^2)	M_X (GeV)	β	$x_{\rm IP}$	$x_{\rm IP}\sigma_r^{D(3)} \pm (stat) \pm (syst)$
110	3	0.9244	0.0038	$0.0287 \pm 0.0045^{+0.0015}_{-0.0043}$
110	3	0.9244	0.0073	$0.0218 \pm 0.0035^{+0.0010}_{-0.0011}$
110	3	0.9244	0.014	$0.0145 \pm 0.0031^{+0.0021}_{-0.0026}$
110	5	0.8148	0.0038	$0.0377 \pm 0.0046^{+0.0036}_{-0.0027}$
110	5	0.8148	0.0073	$0.0309 \pm 0.0040^{+0.0025}_{-0.0033}$
110	5	0.8148	0.014	$0.0311 \pm 0.0041^{+0.0026}_{-0.0039}$
110	8	0.6322	0.0038	$0.0526 \pm 0.0041^{+0.0016}_{-0.0022}$
110	8	0.6322	0.0073	$0.0452 \pm 0.0033^{+0.0034}_{-0.0010}$
110	8	0.6322	0.014	$0.0400 \pm 0.0033^{+0.0041}_{-0.0054}$
110	13	0.3943	0.0073	$0.0471 \pm 0.0031^{+0.0021}_{-0.0025}$
110	13	0.3943	0.014	$0.0388 \pm 0.0028^{+0.0029}_{-0.0037}$
110	20	0.2157	0.014	$0.0435 \pm 0.0030^{+0.0017}_{-0.0034}$
140	3	0.9396	0.0038	$0.0237 \pm 0.0052^{+0.0022}_{-0.0040}$
140	3	0.9396	0.0073	$0.0173 \pm 0.0042^{+0.0017}_{-0.0018}$
140	3	0.9396	0.014	$0.0127 \pm 0.0040^{+0.0030}_{-0.0022}$
140	5	0.8485	0.0038	$0.0293 \pm 0.0054^{+0.0032}_{-0.0036}$
140	5	0.8485	0.0073	$0.0233 \pm 0.0043^{+0.0009}_{-0.0038}$
140	5	0.8485	0.014	$0.0211 \pm 0.0041^{+0.0028}_{-0.0030}$
140	8	0.6863	0.0038	$0.0563 \pm 0.0069^{+0.0049}_{-0.0045}$
140	8	0.6863	0.0073	$0.0443 \pm 0.0043^{+0.0007}_{-0.0037}$
140	8	0.6863	0.014	$0.0345 \pm 0.0039^{+0.0029}_{-0.0038}$
140	13	0.4531	0.0073	$0.0475 \pm 0.0040^{+0.0018}_{-0.0028}$
140	13	0.4531	0.014	$0.0396 \pm 0.0034^{+0.0033}_{-0.0038}$
140	20	0.2593	0.014	$0.0449 \pm 0.0038^{+0.0075}_{-0.0034}$
185	3	0.9536	0.0038	$0.0174 \pm 0.0095^{+0.0110}_{-0.0061}$
185	3	0.9536	0.0073	$0.0166 \pm 0.0069^{+0.0024}_{-0.0001}$
185	3	0.9536	0.014	$0.0199 \pm 0.0072^{+0.0012}_{-0.0032}$
185	5	0.8810	0.0038	$0.0179 \pm 0.0071^{+0.0005}_{-0.0086}$
185	5	0.8810	0.0073	$0.0175 \pm 0.0048^{+0.0017}_{-0.0013}$
185	5	0.8810	0.014	$0.0130 \pm 0.0049^{+0.0030}_{-0.0044}$
185	8	0.7430	0.0073	$0.0319 \pm 0.0049^{+0.0022}_{-0.0039}$
185	8	0.7430	0.014	$0.0292 \pm 0.0044^{+0.0029}_{-0.0031}$
185	13	0.5226	0.0073	$0.0490 \pm 0.0057^{+0.0032}_{-0.0024}$
185	13	0.5226	0.014	$0.0334 \pm 0.0040^{+0.0035}_{-0.0051}$
185	20	0.3162	0.014	$0.0497 \pm 0.0052^{+0.0044}_{-0.0071}$
255	3	0.9659	0.0073	$0.0087 \pm 0.0055^{+0.0008}_{-0.0013}$
255	3	0.9659	0.014	$0.0040 \pm 0.0040^{+0.0024}_{-0.0022}$
255	5	0.9107	0.0073	$0.0147 \pm 0.0056^{+0.0045}_{-0.0009}$
255	5	0.9107	0.014	$0.0095 \pm 0.0050^{+0.0036}_{-0.0051}$
255	8	0.7994	0.0073	$0.0268 \pm 0.0056^{+0.0039}_{-0.0044}$
255	8	0.7994	0.014	$0.0365 \pm 0.0060^{+0.0035}_{-0.0028}$
255	13	0.6014	0.014	$0.0364 \pm 0.0048^{+0.0036}_{-0.0045}$
255	20	0.3893	0.014	$0.0399 \pm 0.0054^{+0.0067}_{-0.0043}$

Table A.9: *The reduced diffractive cross section multiplied by x_{IP}, $x_{\mathrm{IP}}\sigma_r^{D(3)}$, as a function of Q^2 for different values of β, for $x_{\mathrm{IP}} = 0.00028$, 0.00054, and 0.001. The normalisation uncertainty of $\pm 2.25\%$ is not included.*

x_{IP}	β	Q^2 (GeV^2)	$x_{\mathrm{IP}}\sigma_r^{D(3)} \pm (stat) \pm (syst)$
0.00028	0.3	2.5	$0.0554 \pm 0.0008^{+0.0011}_{-0.0020}$
0.00028	0.3	3.5	$0.0626 \pm 0.0010^{+0.0037}_{-0.0012}$
0.00028	0.3	4.5	$0.0560 \pm 0.0013^{+0.0013}_{-0.0019}$
0.00028	0.5	4.5	$0.0529 \pm 0.0014^{+0.0037}_{-0.0017}$
0.00028	0.5	5.5	$0.0535 \pm 0.0014^{+0.0011}_{-0.0029}$
0.00028	0.5	6.5	$0.0592 \pm 0.0018^{+0.0017}_{-0.0036}$
0.00054	0.2	2.5	$0.0375 \pm 0.0006^{+0.0019}_{-0.0009}$
0.00054	0.2	3.5	$0.0424 \pm 0.0008^{+0.0027}_{-0.0021}$
0.00054	0.2	4.5	$0.0403 \pm 0.0011^{+0.0010}_{-0.0026}$
0.00054	0.3	2.5	$0.0407 \pm 0.0006^{+0.0015}_{-0.0009}$
0.00054	0.3	3.5	$0.0483 \pm 0.0008^{+0.0016}_{-0.0014}$
0.00054	0.3	4.5	$0.0480 \pm 0.0008^{+0.0012}_{-0.0023}$
0.00054	0.3	5.5	$0.0499 \pm 0.0010^{+0.0020}_{-0.0014}$
0.00054	0.3	6.5	$0.0520 \pm 0.0012^{+0.0006}_{-0.0013}$
0.00054	0.3	8.5	$0.0548 \pm 0.0011^{+0.0010}_{-0.0014}$
0.00054	0.5	4.5	$0.0507 \pm 0.0014^{+0.0041}_{-0.0013}$
0.00054	0.5	5.5	$0.0518 \pm 0.0013^{+0.0022}_{-0.0024}$
0.00054	0.5	6.5	$0.0566 \pm 0.0015^{+0.0025}_{-0.0025}$
0.00054	0.5	8.5	$0.0580 \pm 0.0010^{+0.0027}_{-0.0008}$
0.00054	0.5	12	$0.0669 \pm 0.0016^{+0.0011}_{-0.0022}$
0.00054	0.7	12	$0.0584 \pm 0.0017^{+0.0013}_{-0.0020}$
0.00054	0.7	16	$0.0618 \pm 0.0022^{+0.0032}_{-0.0014}$
0.001	0.1	2.5	$0.0257 \pm 0.0005^{+0.0009}_{-0.0013}$
0.001	0.1	3.5	$0.0301 \pm 0.0008^{+0.0023}_{-0.0007}$
0.001	0.2	2.5	$0.0269 \pm 0.0005^{+0.0008}_{-0.0014}$
0.001	0.2	3.5	$0.0324 \pm 0.0006^{+0.0007}_{-0.0018}$
0.001	0.2	4.5	$0.0317 \pm 0.0007^{+0.0019}_{-0.0009}$
0.001	0.2	5.5	$0.0326 \pm 0.0008^{+0.0026}_{-0.0005}$
0.001	0.2	6.5	$0.0352 \pm 0.0010^{+0.0006}_{-0.0023}$
0.001	0.2	8.5	$0.0356 \pm 0.0009^{+0.0009}_{-0.0009}$
0.001	0.3	2.5	$0.0334 \pm 0.0005^{+0.0006}_{-0.0016}$
0.001	0.3	3.5	$0.0397 \pm 0.0007^{+0.0014}_{-0.0004}$
0.001	0.3	4.5	$0.0402 \pm 0.0008^{+0.0008}_{-0.0026}$
0.001	0.3	5.5	$0.0414 \pm 0.0009^{+0.0011}_{-0.0008}$
0.001	0.3	6.5	$0.0418 \pm 0.0010^{+0.0019}_{-0.0007}$
0.001	0.3	8.5	$0.0447 \pm 0.0007^{+0.0008}_{-0.0009}$
0.001	0.3	12	$0.0474 \pm 0.0010^{+0.0004}_{-0.0016}$
0.001	0.3	16	$0.0515 \pm 0.0017^{+0.0014}_{-0.0019}$
0.001	0.5	4.5	$0.0434 \pm 0.0013^{+0.0020}_{-0.0006}$
0.001	0.5	5.5	$0.0467 \pm 0.0013^{+0.0018}_{-0.0016}$
0.001	0.5	6.5	$0.0470 \pm 0.0013^{+0.0029}_{-0.0009}$
0.001	0.5	8.5	$0.0533 \pm 0.0010^{+0.0013}_{-0.0018}$
0.001	0.5	12	$0.0581 \pm 0.0013^{+0.0022}_{-0.0007}$
0.001	0.5	16	$0.0606 \pm 0.0017^{+0.0011}_{-0.0013}$
0.001	0.5	22	$0.0645 \pm 0.0021^{+0.0006}_{-0.0039}$
0.001	0.7	12	$0.0505 \pm 0.0015^{+0.0018}_{-0.0019}$
0.001	0.7	16	$0.0578 \pm 0.0018^{+0.0024}_{-0.0014}$
0.001	0.7	22	$0.0589 \pm 0.0021^{+0.0024}_{-0.0018}$
0.001	0.7	30	$0.0572 \pm 0.0024^{+0.0041}_{-0.0015}$
0.001	0.7	40	$0.0587 \pm 0.0039^{+0.0011}_{-0.0033}$
0.001	0.9	40	$0.0398 \pm 0.0036^{+0.0022}_{-0.0024}$
0.001	0.9	50	$0.0299 \pm 0.0041^{+0.0025}_{-0.0025}$

Table A.10: *The reduced diffractive cross section multiplied by x_{IP}, $x_{\mathrm{IP}}\sigma_r^{D(3)}$, as a function of Q^2 for different values of β, for $x_{\mathrm{IP}} = 0.002$. The normalisation uncertainty of $\pm 2.25\%$ is not included.*

x_{IP}	β	Q^2 (GeV^2)	$x_{\mathrm{IP}}\sigma_r^{D(3)} \pm (stat) \pm (syst)$
0.002	0.025	2.5	$0.0249 \pm 0.0006^{+0.0006}_{-0.0016}$
0.002	0.1	2.5	$0.0187 \pm 0.0005^{+0.0010}_{-0.0013}$
0.002	0.1	3.5	$0.0252 \pm 0.0006^{+0.0006}_{-0.0015}$
0.002	0.1	4.5	$0.0240 \pm 0.0007^{+0.0007}_{-0.0021}$
0.002	0.1	5.5	$0.0245 \pm 0.0007^{+0.0021}_{-0.0005}$
0.002	0.1	6.5	$0.0279 \pm 0.0009^{+0.0018}_{-0.0005}$
0.002	0.2	2.5	$0.0234 \pm 0.0005^{+0.0019}_{-0.0003}$
0.002	0.2	3.5	$0.0278 \pm 0.0006^{+0.0005}_{-0.0010}$
0.002	0.2	4.5	$0.0261 \pm 0.0007^{+0.0021}_{-0.0006}$
0.002	0.2	5.5	$0.0262 \pm 0.0007^{+0.0005}_{-0.0021}$
0.002	0.2	6.5	$0.0277 \pm 0.0008^{+0.0008}_{-0.0008}$
0.002	0.2	8.5	$0.0302 \pm 0.0006^{+0.0004}_{-0.0011}$
0.002	0.2	12	$0.0341 \pm 0.0008^{+0.0017}_{-0.0006}$
0.002	0.2	16	$0.0369 \pm 0.0017^{+0.0014}_{-0.0015}$
0.002	0.3	2.5	$0.0262 \pm 0.0005^{+0.0016}_{-0.0004}$
0.002	0.3	3.5	$0.0339 \pm 0.0006^{+0.0005}_{-0.0015}$
0.002	0.3	4.5	$0.0348 \pm 0.0008^{+0.0017}_{-0.0007}$
0.002	0.3	5.5	$0.0347 \pm 0.0009^{+0.0006}_{-0.0013}$
0.002	0.3	6.5	$0.0381 \pm 0.0010^{+0.0014}_{-0.0016}$
0.002	0.3	8.5	$0.0360 \pm 0.0006^{+0.0014}_{-0.0002}$
0.002	0.3	12	$0.0415 \pm 0.0008^{+0.0006}_{-0.0009}$
0.002	0.3	16	$0.0413 \pm 0.0010^{+0.0009}_{-0.0006}$
0.002	0.3	22	$0.0434 \pm 0.0013^{+0.0009}_{-0.0009}$
0.002	0.3	30	$0.0423 \pm 0.0017^{+0.0008}_{-0.0023}$
0.002	0.5	4.5	$0.0402 \pm 0.0014^{+0.0014}_{-0.0010}$
0.002	0.5	5.5	$0.0407 \pm 0.0013^{+0.0016}_{-0.0025}$
0.002	0.5	6.5	$0.0423 \pm 0.0013^{+0.0030}_{-0.0008}$
0.002	0.5	8.5	$0.0451 \pm 0.0009^{+0.0008}_{-0.0024}$
0.002	0.5	12	$0.0502 \pm 0.0012^{+0.0015}_{-0.0009}$
0.002	0.5	16	$0.0525 \pm 0.0015^{+0.0011}_{-0.0024}$
0.002	0.5	22	$0.0530 \pm 0.0017^{+0.0019}_{-0.0007}$
0.002	0.5	30	$0.0515 \pm 0.0019^{+0.0014}_{-0.0019}$
0.002	0.5	40	$0.0585 \pm 0.0027^{+0.0014}_{-0.0029}$
0.002	0.5	50	$0.0547 \pm 0.0035^{+0.0010}_{-0.0018}$
0.002	0.7	12	$0.0464 \pm 0.0014^{+0.0024}_{-0.0013}$
0.002	0.7	16	$0.0493 \pm 0.0016^{+0.0017}_{-0.0036}$
0.002	0.7	22	$0.0515 \pm 0.0018^{+0.0019}_{-0.0015}$
0.002	0.7	30	$0.0486 \pm 0.0021^{+0.0030}_{-0.0018}$
0.002	0.7	40	$0.0502 \pm 0.0026^{+0.0006}_{-0.0018}$
0.002	0.7	50	$0.0518 \pm 0.0031^{+0.0020}_{-0.0024}$
0.002	0.7	65	$0.0524 \pm 0.0041^{+0.0029}_{-0.0036}$
0.002	0.9	40	$0.0338 \pm 0.0029^{+0.0033}_{-0.0014}$
0.002	0.9	50	$0.0367 \pm 0.0034^{+0.0032}_{-0.0024}$
0.002	0.9	65	$0.0373 \pm 0.0037^{+0.0009}_{-0.0028}$
0.002	0.9	85	$0.0324 \pm 0.0045^{+0.0043}_{-0.0012}$

Table A.11: *The reduced diffractive cross section multiplied by $x_{\rm IP}$, $x_{\rm IP}\sigma_r^{D(3)}$, as a function of Q^2 for different values of β, for $x_{\rm IP} = 0.0038$. The normalisation uncertainty of $\pm 2.25\%$ is not included.*

$x_{\rm IP}$	β	Q^2 (GeV^2)	$x_{\rm IP}\sigma_r^{D(3)} \pm (stat) \pm (syst)$
0.0038	0.025	2.5	$0.0210 \pm 0.0004^{+0.0014}_{-0.0013}$
0.0038	0.025	3.5	$0.0242 \pm 0.0006^{+0.0012}_{-0.0017}$
0.0038	0.025	4.5	$0.0265 \pm 0.0006^{+0.0012}_{-0.0016}$
0.0038	0.1	2.5	$0.0174 \pm 0.0005^{+0.0008}_{-0.0020}$
0.0038	0.1	3.5	$0.0216 \pm 0.0006^{+0.0010}_{-0.0015}$
0.0038	0.1	4.5	$0.0228 \pm 0.0007^{+0.0022}_{-0.0002}$
0.0038	0.1	5.5	$0.0221 \pm 0.0007^{+0.0005}_{-0.0013}$
0.0038	0.1	6.5	$0.0235 \pm 0.0008^{+0.0016}_{-0.0015}$
0.0038	0.1	8.5	$0.0272 \pm 0.0006^{+0.0010}_{-0.0010}$
0.0038	0.1	12	$0.0329 \pm 0.0009^{+0.0008}_{-0.0017}$
0.0038	0.2	2.5	$0.0203 \pm 0.0004^{+0.0008}_{-0.0008}$
0.0038	0.2	3.5	$0.0251 \pm 0.0006^{+0.0004}_{-0.0018}$
0.0038	0.2	4.5	$0.0245 \pm 0.0007^{+0.0010}_{-0.0023}$
0.0038	0.2	5.5	$0.0254 \pm 0.0008^{+0.0009}_{-0.0019}$
0.0038	0.2	6.5	$0.0262 \pm 0.0009^{+0.0018}_{-0.0013}$
0.0038	0.2	8.5	$0.0273 \pm 0.0006^{+0.0003}_{-0.0015}$
0.0038	0.2	12	$0.0282 \pm 0.0007^{+0.0012}_{-0.0010}$
0.0038	0.2	16	$0.0305 \pm 0.0009^{+0.0006}_{-0.0016}$
0.0038	0.2	22	$0.0371 \pm 0.0013^{+0.0009}_{-0.0013}$
0.0038	0.2	30	$0.0377 \pm 0.0018^{+0.0008}_{-0.0016}$
0.0038	0.3	2.5	$0.0249 \pm 0.0006^{+0.0003}_{-0.0011}$
0.0038	0.3	3.5	$0.0300 \pm 0.0006^{+0.0018}_{-0.0007}$
0.0038	0.3	4.5	$0.0319 \pm 0.0008^{+0.0013}_{-0.0017}$
0.0038	0.3	5.5	$0.0331 \pm 0.0009^{+0.0017}_{-0.0010}$
0.0038	0.3	6.5	$0.0327 \pm 0.0009^{+0.0004}_{-0.0025}$
0.0038	0.3	8.5	$0.0326 \pm 0.0006^{+0.0012}_{-0.0013}$
0.0038	0.3	12	$0.0343 \pm 0.0008^{+0.0003}_{-0.0016}$
0.0038	0.3	16	$0.0369 \pm 0.0010^{+0.0016}_{-0.0011}$
0.0038	0.3	22	$0.0369 \pm 0.0011^{+0.0011}_{-0.0016}$
0.0038	0.3	30	$0.0377 \pm 0.0013^{+0.0010}_{-0.0010}$
0.0038	0.3	40	$0.0418 \pm 0.0017^{+0.0008}_{-0.0012}$
0.0038	0.3	50	$0.0457 \pm 0.0023^{+0.0003}_{-0.0015}$
0.0038	0.3	65	$0.0474 \pm 0.0035^{+0.0010}_{-0.0019}$
0.0038	0.5	4.5	$0.0350 \pm 0.0013^{+0.0017}_{-0.0012}$
0.0038	0.5	5.5	$0.0351 \pm 0.0012^{+0.0025}_{-0.0013}$
0.0038	0.5	6.5	$0.0384 \pm 0.0015^{+0.0003}_{-0.0038}$
0.0038	0.5	8.5	$0.0398 \pm 0.0009^{+0.0010}_{-0.0019}$
0.0038	0.5	12	$0.0450 \pm 0.0011^{+0.0010}_{-0.0010}$
0.0038	0.5	16	$0.0424 \pm 0.0013^{+0.0021}_{-0.0004}$
0.0038	0.5	22	$0.0469 \pm 0.0015^{+0.0004}_{-0.0027}$
0.0038	0.5	30	$0.0462 \pm 0.0019^{+0.0031}_{-0.0011}$
0.0038	0.5	40	$0.0418 \pm 0.0021^{+0.0026}_{-0.0005}$
0.0038	0.5	50	$0.0459 \pm 0.0025^{+0.0024}_{-0.0012}$
0.0038	0.5	65	$0.0445 \pm 0.0028^{+0.0032}_{-0.0009}$
0.0038	0.5	85	$0.0441 \pm 0.0035^{+0.0035}_{-0.0010}$
0.0038	0.7	12	$0.0396 \pm 0.0013^{+0.0030}_{-0.0005}$
0.0038	0.7	16	$0.0431 \pm 0.0015^{+0.0017}_{-0.0019}$
0.0038	0.7	22	$0.0464 \pm 0.0017^{+0.0016}_{-0.0020}$
0.0038	0.7	30	$0.0460 \pm 0.0021^{+0.0010}_{-0.0027}$
0.0038	0.7	40	$0.0441 \pm 0.0025^{+0.0008}_{-0.0027}$
0.0038	0.7	50	$0.0453 \pm 0.0028^{+0.0020}_{-0.0033}$
0.0038	0.7	65	$0.0435 \pm 0.0031^{+0.0017}_{-0.0017}$
0.0038	0.7	85	$0.0421 \pm 0.0034^{+0.0006}_{-0.0024}$
0.0038	0.7	110	$0.0472 \pm 0.0041^{+0.0019}_{-0.0023}$
0.0038	0.7	140	$0.0555 \pm 0.0070^{+0.0042}_{-0.0066}$
0.0038	0.9	40	$0.0342 \pm 0.0030^{+0.0019}_{-0.0041}$
0.0038	0.9	50	$0.0300 \pm 0.0028^{+0.0016}_{-0.0008}$
0.0038	0.9	65	$0.0330 \pm 0.0033^{+0.0017}_{-0.0018}$
0.0038	0.9	85	$0.0260 \pm 0.0032^{+0.0024}_{-0.0031}$
0.0038	0.9	110	$0.0284 \pm 0.0035^{+0.0010}_{-0.0022}$
0.0038	0.9	140	$0.0282 \pm 0.0043^{+0.0015}_{-0.0012}$
0.0038	0.9	185	$0.0166 \pm 0.0053^{+0.0013}_{-0.0037}$

Table A.12: *The reduced diffractive cross section multiplied by $x_{\rm IP}$, $x_{\rm IP}\sigma_r^{D(3)}$, as a function of Q^2 for different values of β, for $x_{\rm IP} = 0.0073$. The normalisation uncertainty of $\pm 2.25\%$ is not included.*

$x_{\rm IP}$	β	Q^2 (GeV^2)	$x_{\rm IP}\sigma_r^{D(3)} \pm (stat) \pm (syst)$
0.0073	0.025	2.5	$0.0174 \pm 0.0004^{+0.0011}_{-0.0027}$
0.0073	0.025	3.5	$0.0205 \pm 0.0005^{+0.0020}_{-0.0024}$
0.0073	0.025	4.5	$0.0237 \pm 0.0005^{+0.0016}_{-0.0021}$
0.0073	0.025	5.5	$0.0258 \pm 0.0006^{+0.0016}_{-0.0014}$
0.0073	0.025	6.5	$0.0279 \pm 0.0008^{+0.0016}_{-0.0037}$
0.0073	0.025	8.5	$0.0325 \pm 0.0007^{+0.0015}_{-0.0023}$
0.0073	0.1	2.5	$0.0160 \pm 0.0005^{+0.0014}_{-0.0016}$
0.0073	0.1	3.5	$0.0205 \pm 0.0006^{+0.0009}_{-0.0021}$
0.0073	0.1	4.5	$0.0194 \pm 0.0008^{+0.0007}_{-0.0026}$
0.0073	0.1	5.5	$0.0206 \pm 0.0008^{+0.0016}_{-0.0020}$
0.0073	0.1	6.5	$0.0209 \pm 0.0008^{+0.0013}_{-0.0019}$
0.0073	0.1	8.5	$0.0251 \pm 0.0006^{+0.0011}_{-0.0021}$
0.0073	0.1	12	$0.0297 \pm 0.0008^{+0.0011}_{-0.0022}$
0.0073	0.1	16	$0.0330 \pm 0.0011^{+0.0017}_{-0.0022}$
0.0073	0.1	22	$0.0352 \pm 0.0013^{+0.0013}_{-0.0012}$
0.0073	0.2	2.5	$0.0188 \pm 0.0006^{+0.0013}_{-0.0017}$
0.0073	0.2	3.5	$0.0232 \pm 0.0007^{+0.0014}_{-0.0021}$
0.0073	0.2	4.5	$0.0245 \pm 0.0008^{+0.0003}_{-0.0016}$
0.0073	0.2	5.5	$0.0221 \pm 0.0008^{+0.0022}_{-0.0016}$
0.0073	0.2	6.5	$0.0256 \pm 0.0010^{+0.0013}_{-0.0024}$
0.0073	0.2	8.5	$0.0251 \pm 0.0006^{+0.0014}_{-0.0019}$
0.0073	0.2	12	$0.0263 \pm 0.0007^{+0.0025}_{-0.0006}$
0.0073	0.2	16	$0.0296 \pm 0.0009^{+0.0015}_{-0.0013}$
0.0073	0.2	22	$0.0343 \pm 0.0011^{+0.0010}_{-0.0027}$
0.0073	0.2	30	$0.0336 \pm 0.0013^{+0.0024}_{-0.0012}$
0.0073	0.2	40	$0.0383 \pm 0.0018^{+0.0016}_{-0.0014}$
0.0073	0.2	50	$0.0355 \pm 0.0021^{+0.0033}_{-0.0016}$
0.0073	0.3	4.5	$0.0296 \pm 0.0009^{+0.0016}_{-0.0018}$
0.0073	0.3	5.5	$0.0286 \pm 0.0009^{+0.0023}_{-0.0008}$
0.0073	0.3	6.5	$0.0292 \pm 0.0009^{+0.0009}_{-0.0023}$
0.0073	0.3	8.5	$0.0308 \pm 0.0007^{+0.0016}_{-0.0012}$
0.0073	0.3	12	$0.0305 \pm 0.0007^{+0.0012}_{-0.0020}$
0.0073	0.3	16	$0.0320 \pm 0.0009^{+0.0014}_{-0.0013}$
0.0073	0.3	22	$0.0341 \pm 0.0010^{+0.0013}_{-0.0020}$
0.0073	0.3	30	$0.0326 \pm 0.0012^{+0.0016}_{-0.0017}$
0.0073	0.3	40	$0.0338 \pm 0.0015^{+0.0012}_{-0.0021}$
0.0073	0.3	50	$0.0396 \pm 0.0018^{+0.0018}_{-0.0024}$
0.0073	0.3	65	$0.0409 \pm 0.0021^{+0.0013}_{-0.0021}$
0.0073	0.3	85	$0.0407 \pm 0.0026^{+0.0026}_{-0.0021}$
0.0073	0.3	110	$0.0387 \pm 0.0032^{+0.0014}_{-0.0029}$
0.0073	0.5	6.5	$0.0340 \pm 0.0015^{+0.0034}_{-0.0024}$
0.0073	0.5	8.5	$0.0367 \pm 0.0010^{+0.0011}_{-0.0026}$
0.0073	0.5	12	$0.0385 \pm 0.0011^{+0.0015}_{-0.0023}$
0.0073	0.5	16	$0.0418 \pm 0.0014^{+0.0016}_{-0.0028}$
0.0073	0.5	22	$0.0428 \pm 0.0014^{+0.0021}_{-0.0019}$
0.0073	0.5	30	$0.0415 \pm 0.0018^{+0.0026}_{-0.0017}$
0.0073	0.5	40	$0.0370 \pm 0.0020^{+0.0009}_{-0.0031}$
0.0073	0.5	50	$0.0392 \pm 0.0022^{+0.0020}_{-0.0014}$
0.0073	0.5	65	$0.0382 \pm 0.0025^{+0.0019}_{-0.0020}$
0.0073	0.5	85	$0.0430 \pm 0.0031^{+0.0025}_{-0.0026}$
0.0073	0.5	110	$0.0427 \pm 0.0032^{+0.0040}_{-0.0011}$
0.0073	0.5	140	$0.0423 \pm 0.0039^{+0.0011}_{-0.0028}$
0.0073	0.5	185	$0.0450 \pm 0.0061^{+0.0056}_{-0.0035}$
0.0073	0.7	12	$0.0380 \pm 0.0014^{+0.0023}_{-0.0022}$
0.0073	0.7	16	$0.0386 \pm 0.0014^{+0.0021}_{-0.0016}$
0.0073	0.7	22	$0.0430 \pm 0.0017^{+0.0020}_{-0.0032}$
0.0073	0.7	30	$0.0430 \pm 0.0021^{+0.0027}_{-0.0015}$
0.0073	0.7	40	$0.0384 \pm 0.0023^{+0.0018}_{-0.0033}$
0.0073	0.7	50	$0.0333 \pm 0.0024^{+0.0037}_{-0.0010}$
0.0073	0.7	65	$0.0420 \pm 0.0031^{+0.0012}_{-0.0014}$
0.0073	0.7	85	$0.0353 \pm 0.0031^{+0.0014}_{-0.0015}$
0.0073	0.7	110	$0.0416 \pm 0.0036^{+0.0012}_{-0.0027}$
0.0073	0.7	140	$0.0421 \pm 0.0044^{+0.0006}_{-0.0029}$
0.0073	0.7	185	$0.0310 \pm 0.0045^{+0.0011}_{-0.0022}$

Table A.13: *The reduced diffractive cross section multiplied by $x_{\rm IP}$, $x_{\rm IP}\sigma_r^{D(3)}$, as a function of Q^2 for different values of β, for $x_{\rm IP} = 0.0073$ (cont.), and 0.014. The normalisation uncertainty of $\pm 2.25\%$ is not included.*

$x_{\rm IP}$	β	Q^2 (GeV^2)	$x_{\rm IP}\sigma_r^{D(3)} \pm (stat) \pm (syst)$
0.0073	0.7	255	$0.0320 \pm 0.0060^{+0.0072}_{-0.0049}$
0.0073	0.9	40	$0.0272 \pm 0.0027^{+0.0020}_{-0.0032}$
0.0073	0.9	50	$0.0282 \pm 0.0029^{+0.0000}_{-0.0031}$
0.0073	0.9	65	$0.0265 \pm 0.0029^{+0.0019}_{-0.0016}$
0.0073	0.9	85	$0.0270 \pm 0.0033^{+0.0018}_{-0.0011}$
0.0073	0.9	110	$0.0226 \pm 0.0029^{+0.0014}_{-0.0015}$
0.0073	0.9	140	$0.0181 \pm 0.0030^{+0.0020}_{-0.0018}$
0.0073	0.9	185	$0.0205 \pm 0.0040^{+0.0012}_{-0.0018}$
0.0073	0.9	255	$0.0181 \pm 0.0043^{+0.0026}_{-0.0022}$
0.014	0.025	2.5	$0.0167 \pm 0.0005^{+0.0015}_{-0.0016}$
0.014	0.025	3.5	$0.0201 \pm 0.0006^{+0.0032}_{-0.0021}$
0.014	0.025	4.5	$0.0218 \pm 0.0007^{+0.0033}_{-0.0036}$
0.014	0.025	5.5	$0.0239 \pm 0.0007^{+0.0031}_{-0.0041}$
0.014	0.025	6.5	$0.0251 \pm 0.0009^{+0.0021}_{-0.0039}$
0.014	0.025	8.5	$0.0313 \pm 0.0007^{+0.0052}_{-0.0045}$
0.014	0.025	12	$0.0371 \pm 0.0009^{+0.0054}_{-0.0052}$
0.014	0.025	16	$0.0423 \pm 0.0014^{+0.0072}_{-0.0059}$
0.014	0.1	2.5	$0.0152 \pm 0.0007^{+0.0018}_{-0.0015}$
0.014	0.1	3.5	$0.0214 \pm 0.0008^{+0.0012}_{-0.0043}$
0.014	0.1	4.5	$0.0195 \pm 0.0009^{+0.0035}_{-0.0018}$
0.014	0.1	5.5	$0.0215 \pm 0.0010^{+0.0014}_{-0.0032}$
0.014	0.1	6.5	$0.0226 \pm 0.0012^{+0.0037}_{-0.0029}$
0.014	0.1	8.5	$0.0243 \pm 0.0008^{+0.0022}_{-0.0040}$
0.014	0.1	12	$0.0298 \pm 0.0010^{+0.0038}_{-0.0027}$
0.014	0.1	16	$0.0327 \pm 0.0012^{+0.0014}_{-0.0048}$
0.014	0.1	22	$0.0362 \pm 0.0014^{+0.0021}_{-0.0035}$
0.014	0.1	30	$0.0358 \pm 0.0016^{+0.0059}_{-0.0036}$
0.014	0.1	40	$0.0458 \pm 0.0024^{+0.0059}_{-0.0038}$
0.014	0.1	50	$0.0496 \pm 0.0033^{+0.0090}_{-0.0046}$
0.014	0.2	3.5	$0.0206 \pm 0.0009^{+0.0021}_{-0.0031}$
0.014	0.2	4.5	$0.0227 \pm 0.0010^{+0.0020}_{-0.0022}$
0.014	0.2	5.5	$0.0234 \pm 0.0011^{+0.0031}_{-0.0012}$
0.014	0.2	6.5	$0.0232 \pm 0.0011^{+0.0029}_{-0.0024}$
0.014	0.2	8.5	$0.0243 \pm 0.0008^{+0.0018}_{-0.0030}$
0.014	0.2	12	$0.0255 \pm 0.0008^{+0.0017}_{-0.0032}$
0.014	0.2	16	$0.0274 \pm 0.0010^{+0.0023}_{-0.0026}$
0.014	0.2	22	$0.0309 \pm 0.0012^{+0.0021}_{-0.0036}$
0.014	0.2	30	$0.0316 \pm 0.0015^{+0.0015}_{-0.0048}$
0.014	0.2	40	$0.0337 \pm 0.0018^{+0.0050}_{-0.0037}$
0.014	0.2	50	$0.0368 \pm 0.0020^{+0.0038}_{-0.0034}$
0.014	0.2	65	$0.0387 \pm 0.0023^{+0.0023}_{-0.0044}$
0.014	0.2	85	$0.0396 \pm 0.0031^{+0.0045}_{-0.0051}$
0.014	0.2	110	$0.0414 \pm 0.0040^{+0.0043}_{-0.0052}$
0.014	0.3	8.5	$0.0267 \pm 0.0008^{+0.0019}_{-0.0034}$
0.014	0.3	12	$0.0300 \pm 0.0009^{+0.0026}_{-0.0035}$
0.014	0.3	16	$0.0310 \pm 0.0010^{+0.0017}_{-0.0040}$
0.014	0.3	22	$0.0301 \pm 0.0010^{+0.0023}_{-0.0047}$
0.014	0.3	30	$0.0327 \pm 0.0014^{+0.0033}_{-0.0023}$
0.014	0.3	40	$0.0329 \pm 0.0016^{+0.0031}_{-0.0031}$
0.014	0.3	50	$0.0318 \pm 0.0018^{+0.0025}_{-0.0034}$
0.014	0.3	65	$0.0351 \pm 0.0021^{+0.0024}_{-0.0039}$
0.014	0.3	85	$0.0362 \pm 0.0024^{+0.0020}_{-0.0033}$
0.014	0.3	110	$0.0329 \pm 0.0024^{+0.0029}_{-0.0041}$
0.014	0.3	140	$0.0374 \pm 0.0031^{+0.0053}_{-0.0033}$
0.014	0.3	185	$0.0427 \pm 0.0047^{+0.0037}_{-0.0057}$
0.014	0.5	12	$0.0332 \pm 0.0014^{+0.0035}_{-0.0028}$
0.014	0.5	16	$0.0359 \pm 0.0014^{+0.0030}_{-0.0040}$
0.014	0.5	22	$0.0360 \pm 0.0014^{+0.0033}_{-0.0034}$
0.014	0.5	30	$0.0407 \pm 0.0019^{+0.0027}_{-0.0042}$
0.014	0.5	40	$0.0363 \pm 0.0022^{+0.0025}_{-0.0047}$
0.014	0.5	50	$0.0342 \pm 0.0023^{+0.0046}_{-0.0029}$
0.014	0.5	65	$0.0318 \pm 0.0024^{+0.0032}_{-0.0033}$
0.014	0.5	85	$0.0376 \pm 0.0030^{+0.0023}_{-0.0036}$
0.014	0.5	110	$0.0395 \pm 0.0032^{+0.0052}_{-0.0039}$

Table A.14: *The reduced diffractive cross section multiplied by $x_{\rm IP}$, $x_{\rm IP}\sigma_r^{D(3)}$, as a function of Q^2 for different values of β, for $x_{\rm IP} = 0.014$ (cont.). The normalisation uncertainty of $\pm 2.25\%$ is not included.*

$x_{\rm IP}$	β	Q^2 (GeV^2)	$x_{\rm IP}\sigma_r^{D(3)} \pm (stat) \pm (syst)$
0.014	0.5	140	$0.0380 \pm 0.0035^{+0.0022}_{-0.0035}$
0.014	0.5	185	$0.0359 \pm 0.0043^{+0.0028}_{-0.0059}$
0.014	0.5	255	$0.0282 \pm 0.0042^{+0.0030}_{-0.0053}$
0.014	0.7	16	$0.0314 \pm 0.0017^{+0.0036}_{-0.0021}$
0.014	0.7	22	$0.0356 \pm 0.0016^{+0.0054}_{-0.0024}$
0.014	0.7	30	$0.0362 \pm 0.0021^{+0.0062}_{-0.0027}$
0.014	0.7	40	$0.0303 \pm 0.0021^{+0.0048}_{-0.0017}$
0.014	0.7	50	$0.0359 \pm 0.0026^{+0.0019}_{-0.0039}$
0.014	0.7	65	$0.0332 \pm 0.0028^{+0.0024}_{-0.0032}$
0.014	0.7	85	$0.0310 \pm 0.0031^{+0.0032}_{-0.0046}$
0.014	0.7	110	$0.0331 \pm 0.0033^{+0.0029}_{-0.0029}$
0.014	0.7	140	$0.0292 \pm 0.0035^{+0.0029}_{-0.0029}$
0.014	0.7	185	$0.0243 \pm 0.0037^{+0.0033}_{-0.0043}$
0.014	0.7	255	$0.0308 \pm 0.0045^{+0.0044}_{-0.0043}$
0.014	0.9	40	$0.0231 \pm 0.0026^{+0.0018}_{-0.0028}$
0.014	0.9	50	$0.0251 \pm 0.0029^{+0.0026}_{-0.0034}$
0.014	0.9	65	$0.0176 \pm 0.0024^{+0.0028}_{-0.0023}$
0.014	0.9	85	$0.0162 \pm 0.0025^{+0.0023}_{-0.0023}$
0.014	0.9	110	$0.0176 \pm 0.0026^{+0.0023}_{-0.0025}$
0.014	0.9	140	$0.0167 \pm 0.0028^{+0.0025}_{-0.0028}$
0.014	0.9	185	$0.0170 \pm 0.0037^{+0.0020}_{-0.0033}$
0.014	0.9	255	$0.0190 \pm 0.0043^{+0.0027}_{-0.0037}$

Acknowledgements

So many people contributed to the work presented in this thesis, that it is impossible to mention everyone in so short acknowledgements. I am very grateful to all of them.

First of all, I would like to thank Professor Danuta Kisielewska who proposed to me and made possible the work on my PhD within the ZEUS collaboration at DESY. Thanks to her I had the honour to meet and work with people whose help allowed me to perform and finish this work.

Special thanks I direct to my supervisor, Mariusz Przybycień, who provided me assistance, evinced me his patience, and gave me plenty of valuable advice. Many inquiring discussions with him made this thesis better.

I would like to thank Professor Leszek Turczynowicz-Suszycki for care for me when I was beginning to learn the ropes of high energy physics.

I am especially grateful to Alexander Proskuryakov, who did the second independent analysis, for very efficient cooperation and a number of valuable remarks. His knowledge and experience were a great help for me.

Not smaller gratitude I express to the coordinators of the Diffractive and Low-x Working Group, Marta Ruspa, Professor Michele Arneodo, and Professor Aharon Levy. I also direct my thanks to Physics Coordinator of the ZEUS collaboration, Professor Halina Abramowicz and to Yuji Yamazaki. A lot of common discussions explained me many doubts concerning analysis and diffractive physics.

I would also like to thank Bernd Löhr, Günter Wolf, and Heuijin Lim for help in the initial period of my analysis and for later cooperation.

I am sincerely indebted to the former coordinators of the diffractive group, Uta Klein, Kerstin Borras and Alessia Bruni. To a large extent they were influencing on progress in my analysis.

Great thanks to Dorota and Janusz Szuba and to Agnieszka and Krzysztof Wrona for extremely warm and family atmosphere during my stays at DESY, as well as for help and valuable hints for whole duration of my PhD. Gratefullness to Leszek Adamczyk who shared his experience with me, especially when I was starting my analysis.

I am very grateful to Lydia Shcheglova and Irina Korzhavina for friendly atmosphere in the office at DESY and for support.

I would like to thank all my friends and colleagues, not only from Cracow. I wish I could thank you all individually.

Many thanks to Małgorzata Michalska, Łukasz Mączewski, Beata Brzozowska and Krzysztof Komar. I spent many pleasant moments with them, not only at DESY.

I owe special thanks to Marta Wieczorek and Michał Gładysz for a few weeks of nice time when I was finishing my thesis. I am indebted to Marta who made her flat available to me in that time.

I am deeply thankful to my best friend, Agnieszka Jakubowska for her support and cheering me up during my work on PhD.

Finally, I would like to express my gratitude to my family, and above all, to my parents. Their incessant help, support and great patience were indispensable for me for these past years. I have high regard for them.

Bibliography

[1] P.D.B. Collins, *An Introduction to Regge Theory and High Energy Physics*. Cambridge University Press, 1977.

[2] V. N. Gribov, Sov. Phys. JETP **14**, 478 (1962).

[3] UA8 Coll., A. Brandt et al., Phys. Lett. **B 211**, 239 (1988);
UA8 Coll., A. Brandt et al., Phys. Lett. **B 297**, 417 (1992).

[4] ZEUS Coll., S. Chekanov et al., Phys. Lett. **B 516**, 273 (2001).

[5] ZEUS Coll., M. Derrick et al., Phys. Lett. **B 315**, 481 (1993).

[6] H1 Coll., T. Ahmed et al., Nucl. Phys. **B 429**, 477 (1994).

[7] ZEUS Coll., J. Breitweg et al., Eur. Phys. J. **C 6**, 43 (1999).

[8] M. N. Rosenbluth, Phys. Rev. **79**, 615 (1950).

[9] E. Leader and E. Predazzi, *An Introduction to Gauge Theories and the New Physics*. Cambridge University Press, 1982.

[10] F. Halzen and A.D. Martin, *Quarks and Leptons: An Introductory Course in Modern Particle Physics*. John Wiley & Sons, Inc, 1984.

[11] W. H. K. Panofsky, *Proceedings of the 14th International Conference on High Energy Physics*, J. Prentki, J. Steinberger (ed.). Vienna (1968).

[12] W. Albrecht et al.. DESY Report 69/46, 1969.

[13] J.D. Bjorken, Phys. Rev. **179**, 1547 (1969).

[14] R.P. Feynman, Phys. Rev. Lett. **23**, 1415 (1969).

[15] C.G. Callan and D.J. Gross, Phys. Rev. Lett. **22**, 156 (1969).

[16] M. Gell-Mann and Y. Ne'eman, *The Eightfold Way*. Benjamin, New York, 1964.

[17] G. Zweig, Preprint CERN-8192/TH 401, 1964;
G. Zweig, Preprint CERN-8419/TH 412, 1964.

[18] T. Eichten et al., Phys. Lett. **B 46**, 274 (1973).

[19] R. Brandelik et al., Phys. Lett. **B 86**, 243 (1979).

[20] H1 Coll., S. Aid et al., Nucl. Phys. **B 470**, 3 (1996);
ZEUS Coll., M. Derrick et al., Z. Phys. **C 72**, 399 (1996).

[21] Yu.L. Dokshitzer, Sov. Phys. JETP **46**, 641 (1977).

[22] V.N. Gribov and L.N. Lipatov, Sov. J. Nucl. Phys. **15**, 438 (1972);
G. Altarelli and G. Parisi, Nucl. Phys. **B 126**, 298 (1977).

[23] L. N. Lipatov, Sov. J. Nucl. Phys. **23**, 338 (1976);
E.A. Kuraev, L.N. Lipatov and V.S. Fadin, Sov. Phys. JETP **45**, 199 (1977);
Ya.Ya. Balitskii and L.N. Lipatov, Sov. J. Nucl. Phys. **28**, 822 (1978).

[24] L.V. Gribov, E.M. Levin and M.G. Ryskin, Phys. Rep. **100**, 1 (1983).

[25] G. Alberi and G. Goggi, Phys. Rep. **74**, 1 (1981);
K. Goulianos, Phys. Rep. **101**, 169 (1983).

[26] T. Regge, Nuovo Cimento **14**, 951 (1959);
T. Regge, Nuovo Cimento **18**, 947 (1960).

[27] G. F. Chew and S. C. Frautschi, Phys. Rev. Lett. **8**, 41 (1962).

[28] Particle Data Group, S. Eidelman et al., Phys. Lett. **B 592**, 1 (2004).

[29] A. Donnachie and P.V. Landshoff, Phys. Lett. **B 296**, 227 (1992).

[30] A. H. Mueller, Phys. Rev. **D 2**, 2963 (1979).

[31] G. Ingelman and P.E. Schlein, Phys. Lett. **B 152**, 256 (1985).

[32] A. Donnachie and P.V. Landshoff, Phys. Lett. **B 191** (1987).

[33] CEA-Bubble-Chamber Collab., Phys. Rev. **146**, 994 (1966);
Aachen-Berlin-Bonn-Hamburg-Heidelberg-München Collab., Phys. Rev. **175**, 1669 (1968);
Aachen-Berlin-Bonn-Hamburg-Heidelberg-München Collab., Phys. Rev. **188**, 2060 (1969);
J. Ballam et al., Phys. Rev. Lett. **21**, 1544 (1968).

[34] J.J. Sakurai, Phys. Rev. Lett. **22**, 981 (1969).

[35] J.J. Sakurai and D. Schildknecht, Phys. Lett. **B 40**, 121 (1972).

[36] L. Trentadue, G. Veneziano, Phys. Lett. **B 323**, 201 (1994).

[37] A. Berera, D. Soper, Phys. Rev. **D 50**, 4328 (1994).

[38] M. Grazzini, L. Trentadue, G. Veneziano, Nucl. Phys. **B 519**, 394 (1998).

[39] J. Collins, Phys. Rev. **D 57**, 3051 (1998).

[40] V. Barone and E. Predazzi, *High Energy Particle Diffraction*, in Texts and Monographs in Physics. Springer, Berlin, 2002.

[41] M. Arneodo and M. Diehl, Preprint DESY 05-214 (hep-ph/0511047), 2005.

[42] J. Bjorken, J. Kogut, Phys. Rev. **D 8**, 1341 (1973).

[43] J. Bartels, J. Ellis, H. Kowalski, M. Wüsthoff, Eur. Phys. J. **C 7**, 443 (1999).

[44] H. Kowalski, *Proceedings of the Workshop on New Trends in HERA Physics*, G. Grindhammer, B.A. Kniehl and G. Kramer (eds.), pp. 361–380. (1999), available on `http://www-library.desy.de/conf/ringberg99.html`.

[45] W. Buchmüller and A. Hebecker, Nucl. Phys. **B 476**, 203 (1996).

[46] K. Golec-Biernat and J. Kwiecinski, Phys. Lett. **B 335**, 329 (1995).

[47] F.E. Low, Phys. Rev. **D 12**, 163 (1975);
S. Nussinov, Phys. Rev. Lett. **34**, 1286 (1975).

[48] M.G. Ryskin, Z. Phys. **C 57**, 89 (1993).

[49] S. J. Brodsky et al., Phys. Rev. **D 50**, 471 (1994).

[50] E. Gotsman, E. Levin and U. Maor, Nucl. Phys. **B 493**, 354 (1997).

[51] N.N. Nikolaev and B.G. Zakharov, Z. Phys. **C 53**, 331 (1992).

[52] K. Golec-Biernat and M. Wüsthoff, Phys. Rev. **D 59**, 014017 (1999);
K. Golec-Biernat and M. Wüsthoff, Phys. Rev. **D 60**, 114023 (1999);
K. Golec-Biernat and M. Wüsthoff, Eur. Phys. J. **C 20**, 313 (2001).

[53] W. Buchmüller and A. Hebecker, Phys. Lett. **B 355**, 573 (1995).

[54] ZEUS Coll., U. Holm (ed.), *The ZEUS Detector*. Status Report (unpublished), DESY (1993), available on `http://www-zeus.desy.de/bluebook/bluebook.html`.

[55] N. Harnew et al., Nucl. Inst. Meth. **A 279**, 290 (1989);
B. Foster et al., Nucl. Phys. Proc. Suppl. **B 32**, 181 (1993);
B. Foster et al., Nucl. Inst. Meth. **A 338**, 254 (1994).

[56] D.S. Bailey et al., Nucl. Inst. Meth. **A 396**, 320 (1997).

[57] A. Quadt and O. Ruske, *A New Method to Measure Vertex Distributions* (unpublished). ZEUS-98-036, internal ZEUS Note, 1998.

[58] M. Derrick et al., Nucl. Inst. Meth. **A 309**, 77 (1991);
A. Andresen et al., Nucl. Inst. Meth. **A 309**, 101 (1991);
A. Caldwell et al., Nucl. Inst. Meth. **A 321**, 356 (1992);
A. Bernstein et al., Nucl. Inst. Meth. **A 336**, 23 (1993).

[59] ZEUS Coll., FPC group, A. Bamberger et al., Nucl. Inst. Meth. **A 450**, 235 (2000).

[60] H. Bethe and W. Heitler, Proc. Roy. Soc. Lond. **A 146**, 83 (1934).

[61] J. Andruszków et al., Preprint DESY-92-066, DESY, 1992;
ZEUS Coll., M. Derrick et al., Z. Phys. **C 63**, 391 (1994);
J. Andruszków et al., Acta Phys. Pol. **B 32**, 2025 (2001).

[62] C. Youngman, *The ZEUS Data Acquisition System* (unpublished). ZEUS-92-150A, 1992.

[63] W. H. Smith et al., *The ZEUS Trigger System* (unpublished). ZEUS-89-084, 1989;
ZEUS Coll., R. Carlin et al., Nucl. Inst. Meth. **A 379**, 542 (1996).

[64] U. Behrens, L. Hagge and W.O. Vogel, Nucl. Inst. Meth. **A 332**, 253 (1993).

[65] S.M. Fisher and P. Palazzi, *ADAMO Programmers Manual – Version 3.2*. CERN ECP, available on `http://adamo.web.cern.ch/Adamo/programmers_manual/TOC_of_adamo.html`.

[66] Frédéric Bénard, Robert S. Orr, Stefan Polenz, and David Simmons, *The 1995 TLT Filter Software* (unpublished). ZEUS-95-164, 1995.

[67] H. Spiesberger, DJANGO6 *Version 2.4 – A Monte Carlo Generator for Deep Inelastic Lepton Proton Scattering Including QED and QCD Radiative Effects*, 1996, available on `http://www.desy.de/~hspiesb/django6.html`;

H. Spiesberger, HERACLES *and* DJANGOH*: Event Generation for ep Interactions at HERA Including Radiative Processes*, 1998, available on `http://www.desy.de/~hspiesb/djangoh.html`.

[68] T. Sjöstrand, Comp. Phys. Comm. **82**, 74 (1994).

[69] A. Kwiatkowski, H. Spiesberger and H.-J. Möhring, Comp. Phys. Comm. **69**, 155 (1992). Also in *Proc. Workshop Physics at HERA*, eds. W. Buchmüller and G.Ingelman, (DESY, Hamburg, 1991);
H. Spiesberger, *An Event Generator for ep Interactions at HERA Including Radiative Processes (Version 4.6)*, 1996, available on `http://www.desy.de/~hspiesb/heracles.html`.

[70] L. Lönnblad, Comp. Phys. Comm. **71**, 15 (1992).

[71] Y. Azimov et al., Phys. Lett. **B 165**, 147 (1985);
G. Gustafson, U. Petterson, Nucl. Phys. **B 306**, 746 (1988);
B. Andersson et al., Z. Phys. **C 43**, 625 (1989).

[72] G. Ingelman, A. Edin and J. Rathsman, Comp. Phys. Comm. **101**, 108 (1997).

[73] B. Andersson et al., Phys. Rep. **97**, 31 (1983).

[74] H. Jung, Comp. Phys. Comm. **86**, 147 (1995);
H. Jung, *The RAPGAP Monte Carlo for Deep Inelastic Scattering version 2.08*, 1999, available on `http://www.quark.lu.se/~hannes/rapgap.html`.

[75] H.L. Lai et al., Phys. Rev. **D 55**, 1280 (1997).

[76] R. Brun et al., GEANT3, Technical Report CERN-DD/EE/84-1, CERN, 1987.

[77] E. de Wolf et al., ZGANA*, ZEUS trigger simulation library*, 1981.

[78] G.F. Hartner et al., *VCTRAK(3.07/04): Offline Output Information* (unpublished). ZEUS-97-064, internal ZEUS Note, 1997;
G.F. Hartner, *VCTRAK Briefing: Program and Math* (unpublished). ZEUS-98-058, internal ZEUS Note, 1998.

[79] H. Abramowicz, A. Caldwell and R. Sinkus, Nucl. Inst. Meth. **A 365**, 508 (1995);
R. Sinkus and T. Voss, Nucl. Inst. Meth. **A 391**, 360 (1997).

[80] A. Bamberger et al., Nucl. Inst. Meth. **A 401**, 63 (1997);
J. Ng and W. Verkerke, *An Overview of SRTD Analysis* (unpublished). ZEUS-95-37.

[81] V. A. Kuzmin, *HES bad cells exclusion from data and MC* (unpublished). ZEUS-02-015, 2002.

[82] A. Bernstein et al., Nucl. Inst. Meth. **A 336**, 23 (1993).

[83] G.M. Briskin, *Diffractive Dissociation in ep Deep Inelastic Scattering*. Ph.D. Thesis, Tel Aviv University, Report DESY-THESIS 1998-036, 1998.

[84] G. A. Akopjanov et al., Nucl. Inst. Meth. **140**, 441 (1977).

[85] T. C. Awes et al., Nucl. Inst. Meth. **A 311**, 130 (1977).

[86] J. Krüger, *The Uranium Scintillator Calorimeter for the ZEUS Detector at the Electron - Proton collider HERA: The Heart of ZEUS*. Habilitation Thesis, Universität Hamburg, Report DESY-F35-92-02, 1992.

[87] F. Jacquet and A. Blondel, *Proc. the Study of an eP Facility for Europe*, U. Amaldi (ed.), p. 391. (1979). Also in preprint DESY 79-48.

[88] S. Bentvelsen, J. Engelen and P. Kooijman, *Proc. Workshop on Physics at HERA*, W. Buchmüller and G. Ingelman (eds.), Vol. 1, p. 23. Hamburg, Germany, DESY (1992).

[89] ZEUS Coll., J. Breitweg et al., Eur. Phys. J. **C 1**, 81 (1998).

[90] ZEUS Coll., M. Derrick et al., Z. Phys. **C 70**, 391 (1996).

[91] N.N. Nikolaev and B.G. Zakharov, Z. Phys. **C 64**, 631 (1994).

[92] ZEUS Coll., S. Chekanov et al., Eur. Phys. J. **C 38**, 43 (2004).

[93] V. Blobel, Preprint DESY 84-118, 1984.

[94] N. D. Gagunashvili, Nucl. Inst. Meth. **A 343**, 606 (1994).

[95] See e.g.: M. McDermott and G. Briskin, *Proc. Workshop on Future Physics at HERA*, G. Ingelman, A. De Roeck and R. Klanner (eds.), Vol. 2, p. 691. DESY, Hamburg, Germany (1996).

[96] E. Leader and E. Predazzi, *An Introduction to Gauge Theories and Modern Particle Physics*, Vol. 1. Cambridge University Press, 1996.

[97] J.R. Cudell, K. Kang and S.K. Kim, Phys. Lett. **B 395**, 311 (1997).

[98] H. Abramowicz, Int. J. Mod. Phys. **A 15 S1b**, 495 (2000).

[99] I.P. Ivanov, N.N. Nikolaev and A.A. Savin, hep-ph/0501034 (2005).

[100] M. Glück, E. Reya and A. Vogt, Z. Phys. **C 53**, 127 (1992).

[101] M. Glück, E. Reya and A. Vogt, Z. Phys. **C 53**, 651 (1992).

[102] M. Glück, E. Reya and A. Vogt, Z. Phys. **C 67**, 433 (1995).

[103] J.F. Owens, Phys. Rev. **D30**, 943 (1984).

[104] H1 Coll. et al., Eur. Phys. J. **C 48**, 715 (2006).

[105] H1 Coll. et al., Eur. Phys. J. **C 48**, 749 (2006).